Koppelen naar en proben van nanofotonische circuits met metaalroosters

Metal Grating Based Interfacing to and Probing of Nanophotonic Circuits

Stijn Scheerlinck

Promotoren: prof. dr. ir. R. Baets, prof. dr. ir. D. Van Thourhout
Proefschrift ingediend tot het behalen van de graad van
Doctor in de Ingenieurswetenschappen: Elektrotechniek

Vakgroep Informatietechnologie
Voorzitter: prof. dr. ir. D. De Zutter
Faculteit Ingenieurswetenschappen
Academiejaar 2008 - 2009

UNIVERSITEIT GENT

ISBN 978-90-8578-245-2
NUR 959
Wettelijk depot: D/2009/10.500/3

Promotoren:

Prof. dr. ir. R. Baets	Universiteit Gent, INTEC
Prof. dr. ir. D. Van Thourhout	Universiteit Gent, INTEC

Examencommissie:

Prof. dr. ir. R. Verhoeven	Universiteit Gent, INTEC
Prof. dr. ir. P. Bienstman	Universiteit Gent, INTEC
Prof. dr. ir. A. Kristensen	Technical University of Denmark, MIC
Prof. dr. P. Dubruel	Universiteit Gent, Organische Chemie
Prof. dr. ir. J. Vanfleteren	Universiteit Gent, ELIS
Dr. ir. D. Delbeke	Universiteit Gent, INTEC

Universiteit Gent
Faculteit Ingenieurswetenschappen

Vakgroep Informatietechnologie (INTEC)
Sint-Pietersnieuwstraat 41
B-9000 Gent
België

Tel.: +32-9-264.33.24
Fax: +32-9-264.35.93
http://www.intec.ugent.be

Dit werk kwam tot stand in het kader van een specialisatiebeurs toegekend door het IWT (Instituut voor de Aanmoediging van Innovatie door Wetenschap en Technologie in Vlaanderen). This work was carried out in the frameworks of the European IST-ePIXnet network of excellence, the Belgian IAP-Photon project and the Ghent University GOA project "Label-free and multi-parameter detection of biomolecules on nanosurfaces using photonic techniques".

Dankwoord

Aan het eind gekomen van mijn doctoraatsavontuur zou ik graag enkele mensen willen bedanken die een bijzondere rol hebben gespeeld in de afgelopen jaren. Terwijl ik mij de gezichten voor de geest haal van wie ik allemaal wil bedanken, denk ik prompt aan enkele indrukwekkende gebeurtenissen van de voorbije jaren. Zo denk ik aan de laatste photonics-dag op de Gentse binnenwateren: iedereen doorweekt, hetzij door de regen, hetzij door toedoen van vijandelijke kanos. Ik denk aan het benevelend bezoek aan graanstokerij Filliers, het adembenemende Deltapark Neeltje Jans en de vermoeiende zeiltocht op het IJsselmeer. Mijn gedachten dwalen af naar een pannenkoekenslag op het koertje van de 39, naar mijn eerste ontmoeting met Gunay die mij stevig op de schouder klopt en vraagt hoe het met me gaat, naar een illusionist in Sint-Amandsberg die Sam tracht te overtuigen, naar Lieven en zijn moppen, naar Peter en zijn Petere moppen.

Ik dank Prof. Roel Baets en Prof. Dries Van Thourhout voor hun promotorschap. Kunnen doctoreren in zo 'n sterk uitgebouwde, veelzijdige en aangename onderzoeksgroep waar creativiteit zoveel kansen krijgt, was een heel bijzondere ervaring. Dank aan mijn bureaugenoten van het eerste uur: Hans, Hendrik, Wouter, Wouter, Peter Geerinck, Ilse en Gunther. Dank aan Peter Nieuws Uit De Wereld, Hans en Joost met wie ik het tijdperk betrad van de kleinere intiemere bureaus in Gent in combinatie met desk-sharing in Zwijnaarde. Dank aan Koen en Kristof die mij er op tijd aan herinnerden dat ik ancien geworden was en dus kon aanspraak maken op een nog intiemere bureau op het einde van de gang. Daar bracht ik de meest vruchtbare periode door in het gezelschap van Wouter, Katrien en Peter en kortstondig ook Yannick en Marie en bij momenten Dave, natuurlijk. Een dikke merci voor die schitterende laatste maanden in ons bureautje! Steven en Liesbet, bedankt voor jullie zorg om de clean room en de fijne momenten aldaar, al dan niet achter het FIB/SEM-scherm gekluisterd. Dank aan Ilse, Ilse, Karien en Bernadette voor het papierwerk. Speciale dank aan Jonathan en Frederik voor hun operatorengeduld en aan Hans, Peter, Peter en Peter, Pieter, Wim, Jie, Shankar, Geert, Dirk, Bjorn, Denis, Jeroen, Tom, Bram, Wout, Els, Danae, Rasmus en Joris voor de samenwerking, interessante discussies en de frisse ideeën.

Met het schrijven van dit dankwoord komt er een einde aan 10 boeiende jaren aan deze universiteit. Het waren 10 rijk gevulde jaren die ik niet had willen missen. De fijne herinneringen aan alle VTK-, IAYC-, IWA-, ETH-, AKO-, AOZ-, JUPLA-, JEMOO-, DSO-, OVSO- en duo-, trio-, kwartet- en andere muziek-gerelateerde activiteiten en vooral de vriendschappen die ik eraan ontleen zal ik blijven koesteren. Dank u, lieve mama en papa, om mij destijds naar Gent op kot te sturen en mij rond te voeren van Gent naar eender waar zolang ik nog geen rijbewijs had. Dank u, Gerrit-Jan, Eva en Anne-Leen voor jullie steun en geduld met mij, ook al was ik er niet altijd. Dank je, lieve Liesbet, om mij te vinden, en met mij de allermooiste momenten te beleven. Dank je, Korneel, om bij ons te komen!

Gent, 11 januari 2009

Contents

Dankwoord **i**

Samenvatting **1**
1 Nano-imprintlithografie op chips en vezelfacetten 1
2 Metalen roosterkoppelaar 2
3 Polymeer-wig voor vertikale koppeling 3
4 Vezelprobe op basis van een metaalrooster 4

Summary **1**
1 Nanoimprint lithography on chips and fiber facets 1
2 Metal grating coupler 2
3 Polymer wedge for vertical coupling 3
4 Metal-grating based optical fiber probe 3

1 Introduction **1-1**
1.1 Photonics 1-2
1.1.1 Communicating with light 1-2
1.1.2 Sensing with light 1-4
1.2 Silicon-on-Insulator photonic integrated circuits 1-5
1.3 Challenges and future practice 1-8
1.4 Purpose and outline of this work 1-10
1.5 Publications 1-10
1.5.1 Publications in international journals 1-11
1.5.2 Publications in international conference proceedings . . 1-12
1.5.3 Publications in national conferences 1-13
1.5.4 Patent applications 1-13

2 Nanopatterning techniques **2-1**
2.1 Introduction 2-2
2.2 Nanopatterning techniques 2-2
2.2.1 Principles of lithography 2-2
2.2.2 Direct write lithography 2-3
2.2.2.1 Electron beam lithography 2-3

2.2.2.2 Focused ion beam milling 2-4
2.2.2.3 Excimer laser ablation 2-5
2.2.3 Optical contact and projection lithography 2-6
2.2.4 Structuring fiber facets 2-8
2.2.4.1 Fiber cleaving and fiber polishing 2-9
2.2.4.2 Focused ion beam versus electron beam lithography 2-9
2.2.4.3 Alternative solutions 2-12
2.3 Nanoimprint lithography based techniques 2-13
2.3.1 Introduction 2-13
2.3.2 Principles of nanoimprint lithography 2-16
2.3.3 Adhesion control and anti-adhesion treatment 2-19
2.3.4 Imprint tools 2-20
2.3.5 Polymers 2-23
2.3.5.1 PAK-01 2-23
2.3.5.2 J-Resist 2-24
2.3.5.3 SU-8 2-25
2.3.5.4 PDMS 2-26
2.3.5.5 PMMA 2-26
2.3.6 Process development 2-27
2.3.6.1 Double UV-based nanoimprint for defining metal nanostructures 2-27
2.3.6.2 Nano-print 2-31
2.3.6.3 UV-based nanoimprint-and-transfer 2-32
2.3.6.4 Alignment & 3D-imprint 2-34
2.3.6.5 Photonic circuit fabrication 2-37
2.4 Nanoimprint lithography based patterning of fiber facets 2-40
2.4.1 Process and set-up 2-40
2.4.2 Results 2-41
2.5 Conclusion 2-43
Bibliography 2-47

3 Out-of-plane grating couplers **3-1**
3.1 Introduction 3-2
3.2 Basics and definitions 3-2
3.3 Simulation tools 3-4
3.3.1 Eigenmode expansion 3-5
3.3.2 Finite difference time domain 3-6
3.3.3 3D approximation using 2D calculations 3-7
3.4 Experimental tools 3-8
3.5 State-of-the-art: fiber coupling 3-10
3.6 State-of-the-art: free-space coupling 3-11
3.7 Low-index versus high-index contrast waveguide platforms . . 3-12

3.8 Conclusion 3-14
Bibliography 3-16

4 Metal grating coupler **4-1**
4.1 Introduction 4-2
4.2 Metals 4-2
4.2.1 Optical properties 4-2
4.2.2 Surface plasmons 4-4
4.3 Metal grating couplers for Silicon-on-Insulator circuits 4-7
4.3.1 Rationale 4-7
4.3.2 Design and simulation methods 4-8
4.3.3 Coupling efficiency 4-9
4.4 Fabrication and measurements 4-18
4.4.1 Focused ion beam milling 4-19
4.4.2 Nanoimprint and lift-off 4-20
4.4.3 Electron beam lithography 4-24
4.5 Conclusion 4-26
Bibliography 4-28

5 Angled facets for vertical coupling **5-1**
5.1 Introduction 5-2
5.2 Concept 5-2
5.3 Design 5-3
5.4 Fabrication and measurements 5-5
5.4.1 Polymer wedges by fiber molding 5-5
5.4.2 Polymer wedges by 3D nanoimprint 5-6
5.4.3 Air wedges by molding on fiber facets 5-7
5.5 Applications 5-11
5.6 Conclusion 5-12
Bibliography 5-14

6 Metal grating based fiber probe **6-1**
6.1 Introduction 6-2
6.2 Optical fiber probes: literature overview 6-4
6.3 Novel concept for wafer-scale circuit testing 6-7
6.4 Design 6-9
6.5 Fabrication issues 6-10
6.6 Measurement results 6-14
6.6.1 Distance dependent coupling 6-14
6.6.2 Coupling efficiency 6-16
6.6.3 Circuit probing 6-18
6.6.4 Multiple usage 6-19
6.7 Conclusion 6-21

Bibliography 6-22

7 Conclusion and perspectives **7-1**
7.1 Conclusions 7-2
7.2 Future work 7-3
Bibliography 7-6

Samenvatting

Samenvatting

MINIATURIZEREN en integreren van optische componenten op een kleine chip heet fotonische integratie. Fotonische chips zijn het equivalent van de elektronische chips, maar werken met licht in plaats van met elektronen. Werken met licht biedt heel wat voordelen, in het bijzonder wanneer licht kan gecontroleerd worden op de minuscule schaal van een micrometer en kleiner. Verwacht wordt dat fotonische chips zullen worden toegepast voor tele- en datacommunicatie, sensoren voor de chemische en farmaceutische industrie, zorg voor het milieu, geneeskunde en nog vele andere. Het materiaalsysteem Silicium-op-Isolator (SOI) is door het hoge brekingsindex-verschil tussen het silicium en de isolator een erg veelbelovend materiaalsysteem voor dergelijke fotonische chips.

Een typisch fabricageproces voor fotonische chips start bij een SOI wafer en maakt gebruik van waferschaal processen die oorspronkelijk ontwikkeld werden voor de elektronica-industrie. Nieuwe componenten en methoden zijn echter nodig om deze chips te testen en in te pakken. In dit werk worden nieuwe componenten ontworpen en gedemonstreerd die testen en inpakken in de toekomst kunnen vergemakkelijken. Deze componenten zijn metalen roosterkoppelaars, polymeer-wiggen en optische vezelprobes. Om deze te vervaardigen werden enkele nieuwe technieken ontwikkeld die gebaseerd zijn op nano-imprintlithografie. Deze technieken maken het mogelijk om metalen roosterkoppelaars en polymeer-wiggen te definiëren op fotonisch geïntegreerde circuits op een chip of op het minuscule oppervlak van een optische vezelfacet.

1 Nano-imprintlithografie op chips en vezelfacetten

Nano-imprintlithografie is een goedkope manier om structuren te definiëren met erg hoge resolutie en wint daarom gestaag aan populariteit. Deze techiek is in essentie een heel eenvoudige techniek waarvan intussen verscheidene varianten gedemonstreerd werden, naargelang van de toepassing. Het principe is als volgt: eerst wordt een stempel met de gewenste structuur in een polymeer gedrukt dat zich op een substraat bevindt. Vervolgens wordt het polymeer uitgehard om de structuur te bewaren en daarna wordt de stempel terug

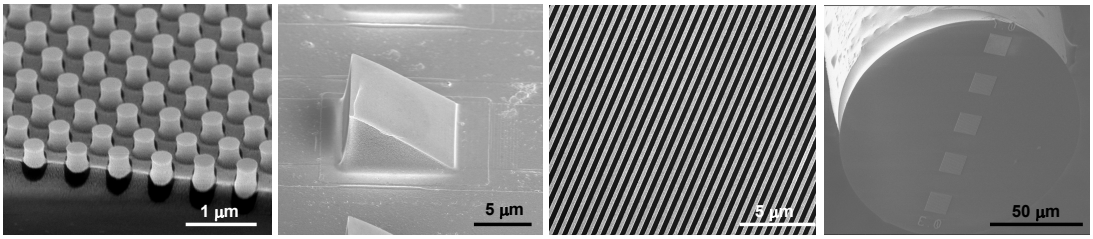

Figuur 1: Overzicht van gefabriceerde structuren met nano-imprintlithografie. Van links naar rechts: sub-micron polymeer pilaren, polymeer wiggen gealigneerd bovenop silicium roosterkoppelaars, gouden roosters met een sub-micron periode en compacte gouden roosters met sub-micron periode op het facet van een monomode vezel.

weggenomen. Nano-imprintlithografie is in volle ontwikkeling en wordt voor talrijke toepassingen gebruikt, in het bijzonder in toepassingsdomeinen waar niet zozeer de hoge resolutie dan wel de flexibiliteit inzake keuze van materialen en het gebruiksgemak een rol spelen.

In dit werk hebben we aangetoond dat UV-gebaseerde nano-imprintlithografie een zeer toegankelijke techniek is om twee- en drie-dimensionale structuren te definiëren zonder gesofisticeerde imprint machines. Voor stempelfabricage maken we gebruik van diep UV lithografie en gefocuseerde ionenbundels. Met UV-gebaseerde nano-imprintlithografie hebben we metalen nanostructuren en polymeer wiggen vervaardigd bovenop silicium chips. Daartoe hebben we gebruik gemaakt van een standaard alignatiesysteem voor optische contactlithografie (MA-6, Süss MicroTek). Deze structuren hebben we ook weten te definiëren op optische vezelfacetten. Daartoe hebben we gebruik gemaakt van een eenvoudige opstelling die toelaat om de structuren te aligneren ten opzichte van de vezelkern. Een overzicht van enkele gefabriceerde structuren met nano-imprintlithografie is opgenomen in Fig. 1.

2 Metalen roosterkoppelaar

Het probleem om efficiënt licht te koppelen in fotonische chips wordt zeer elegant opgelost met zogenaamde roosterkoppelaars. Dit zijn roosters die in een lichtgeleider worden geëtst en breedbandig en efficiënte koppeling van licht mogelijk maken tussen optische vezels en fotonische circuits. In dit werk hebben we een alternatieve structuur bedacht om deze koppeling mogelijk te maken in de vorm van een metaalrooster bovenop de lichtgeleider. We hebben aangetoond dat het hoge brekingsindex contrast dat wordt veroorzaakt door het metaal de dominerende factor is in het werkingsprincipe van deze component. Bovendien hebben we bewezen dat de absorptieverliezen die inherent

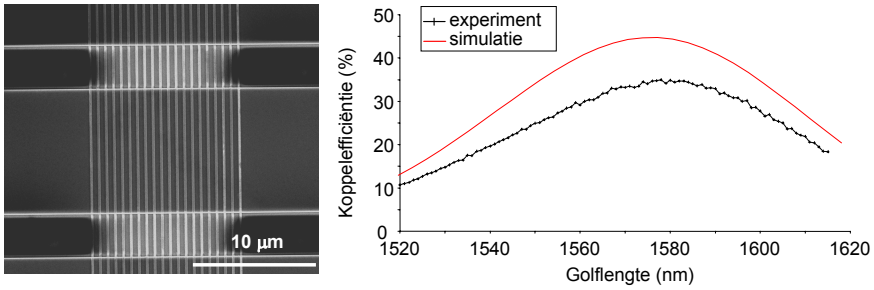

Figuur 2: Efficiënt en breedbandige koppeling tussen silicium-op-isolator lichtgeleiders en optische vezels met gouden roosterkoppelaars gefabriceerd met elektronenbundel lithografie.

zijn aan het gebruik van metalen kunnen worden geminimaliseerd door de preciese geometrie van het rooster te controleren.

Tot de voordelen van metalen roosterkoppelaars behoren het gemak van fabricage en het potentieel van integratie met elektronische componenten. Gouden roosterkoppelaars bovenop silicium-op-isolator lichtgeleiders werden vervaardigd met gefocuseerde ionenbundels and elektronenbundel lithografie. De beste resultaten werden geboekt met elektronenbundel lithografie: een koppelefficiëntie van 34 % en een 1 dB bandbreedte van 40 nm werd aangetoond tussen een SOI lichtgeleider en een optische vezel die een hoek maakt van 10 graden met de vertikale. Het experimentele resultaat komt goed overeen met het resultaat uit simulaties (zie Fig. 2).

3 Polymeer-wig voor vertikale koppeling

Perfect vertikale koppeling met fotonisch geïntegreerde circuits is niet eenvoudig. Zowel vanuit theoretisch als praktisch oogpunt is het realiseren van koppeling in een richting die een kleine hoek maakt met de vertikale veel eenvoudiger. Niettemin zou perfect vertikale koppeling veel meer voordelen bieden voor het inpakken van fotonische chips en voor integratie met andere componenten zoals lichtbronnen. Een eenvoudige aanpak om dit probleem op te lossen is gebruik te maken van refractieve elementen bovenop roosterkoppelaars. Het refractief element zorgt er als het ware voor dat het licht wordt georiënteerd in de perfect vertikale richting, zoals schematisch geschetst in Fig. 3. Wij hebben dit principe aangetoond door polymeer-wiggen te integreren op chips en op optische vezels en hebben vastgesteld dat het verlies in koppelefficiëntie miniem is.

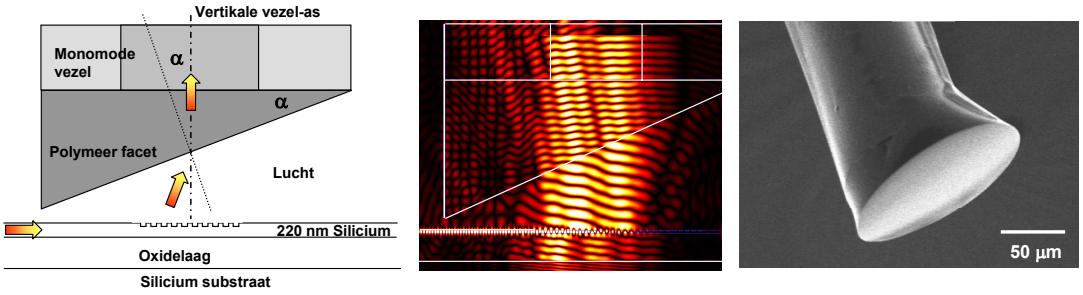

Figuur 3: Perfect vertikale koppeling tussen silicium-op-isolator lichtgeleiders en optische vezels met polymeer-wig op het vezelfacet.

4 Vezelprobe op basis van een metaalrooster

Koppeling uit het vlak van een fotonische chip is bijzonder interessant voor waferschaal testen van fotonisch geïntegreerde circuits. De enige componenten die deze functie echter kunnen waarnemen zijn roosterkoppelaars die op voorhand geïntegreerd worden in het circuit, waardoor het testen van circuits gelimiteerd is tot het testen van het stukje circuit tussen de roosterkoppelaars. Dit zijn immers de enige optische toegangspunten van de chip. Voor toekomstige fotonische chips die steeds in complexititeit zullen toenemen is een flexibeler aanpak nodig die toelaat om de toegangspunten tot het circuit vrij te kiezen. Onze oplossing bestaat erin om gebruik te maken van optische vezelprobes met een roosterkoppelaar op het facet van de probe. Deze probes laten toe om individuele componenten of verschillende componenten die met elkaar verbonden zijn via lichtgeleiders te testen volgens het principeschema in Fig. 4 (a). We hebben een prototype optische vezelprobe vervaardigd die gebaseerd is op een gouden rooster op het facet. We hebben een nano-imprint-and-transfert techniek ontwikkeld om deze probes te vervaardigen in een enkele processtap. Dit is mogelijk met behulp van een hybride silicium/goud stempel die bovendien is uitgerust met een lichtgeleidingslaag die nauwkeurige alignatie toelaat van het rooster ten opzicht van de vezelkern.

Door contact te maken tussen de optische vezelprobe en een 3 μm brede SOI lichtgeleider werd een koppelefficiëntie aangetoond van 15 %, wat zeer goed overeenkomt met onze theoretische berekeningen. Vergeleken met bestaande optische vezelprobes die in de literatuur zijn beschreven, is dit de enige probe die koppeling uit het vlak van de chip combineert met een hoge efficiëntie en breedbandige koppeling. Het testen van een geïntegreerde microring resonator met behulp van twee probes werd in dit werk voor het eerst gedemonstreerd. Het resultaat van deze meting is opgenomen in Fig. 4 (b).

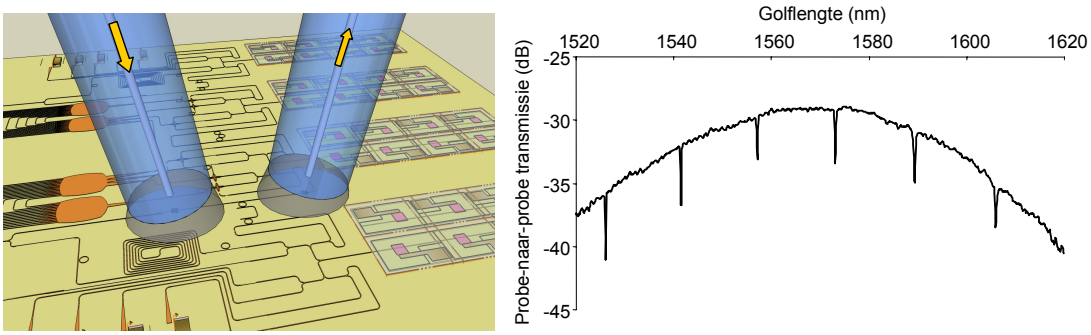

Figuur 4: Twee optische vezelprobes met een metaalrooster op het facet worden gebruikt om een geïntegreerde microring resonator te testen: artistieke impressie en experimentele demonstratie.

Summary

Summary

PHOTONIC integration is the process of miniaturizing optical components and integrate them onto small chips. Chips containing photonic, electronic and possibly fluidic functionality are expected to find applications in areas as broad as tele- and datacommunication, mechanical-, chemical- and bio-sensing, medicine, pharmaceutics, environmental monitoring and many more. Silicon-on-Insulator (SOI) is one of the most promising material platforms for the manufacturing of photonic integrated circuits, because of the high refractive index contrast between the silicon and the isolator.

A possible process flow for future photonic integrated circuits starts from an SOI wafer and makes use of state-of-the-art wafer-scale processes, which are originally developed for the electronics manufacturing industry. Whereas standard processes can be adapted for the fabrication of photonic integrated circuits, novel components and methods are needed for the testing, packaging and assembly of these circuits into final products. In this work, we design, fabricate and demonstrate novel coupling components that are expected to facilitate testing and packaging in the future. These components include metal grating couplers, polymer wedges and optical fiber probes. To fabricate these components, a number of novel techniques are developed based on nanoimprint lithography. These techniques allow us to define metal grating couplers and polymer wedges on top of photonic integrated circuits as well as on tiny optical fiber facets. In the following, we briefly summarize our work.

1 Nanoimprint lithography on chips and fiber facets

Nanoimprint lithography is an emerging high resolution and low cost lithography technique. It is essentially a molding technique and is in principle very simple and very flexible. Depending on the application, there exist numerous variants of the nanoimprint technique. The principle to define the desired pattern is the following: press a mold into a polymer layer on top of a substrate, lock the polymer into place by a curing mechanism and demold the mold again. Although nanoimprint lithography is still in a developing stage - certainly with regard to high volume fabrication of electronic circuitry - it offers a number of very promising opportunities in other application areas

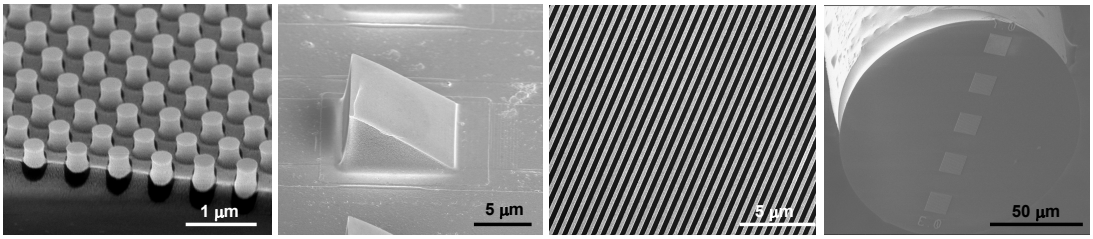

Figure 1: Fabrication results of in-house developed techniques based on nanoimprint lithography. From left to right: sub-micron polymer pillars, polymer wedges aligned on top of grating couplers, large area sub-micron period gold gratings, small sub-micron period gold gratings aligned to the core of a single-mode fiber.

where not so much the resolution but the flexibility with respect to materials and substrates and the ease of processing are key properties.

By making appropriate choices with regard to the properties of the nanoimprint polymer, we show that UV-based nanoimprint is suitable for two-dimensional as well as three-dimensional patterning without very sophisticated imprint tools. For the mold fabrication we rely on deep-UV fabrication for the two-dimensional silicon molds and focused ion beam milling for the three-dimensional glass molds. Metal nanostructures and polymer wedges are fabricated on top of unstructured and structured silicon samples by UV-based nanoimprint using an MA-6 Mask Aligner (Suss MicroTek). These types of structures are also fabricated on top of tiny optical fiber facets using a simple set-up that allows for proper orientation and alignment of the optical fiber with respect to the mold structures. Figure 1 depicts some of the results of our process development.

2 Metal grating coupler

Out-of-plane grating couplers are a very elegant solution to the problem of coupling light into and out of ultra-compact photonic integrated circuits. Due to extensive research on these components, efficient and broadband coupling of light between optical fibers and on-chip waveguides has already been demonstrated. All of these couplers are defined by etching slits into the waveguide. In this work, we offer an alternative solution: grating couplers based on a metal grating on top of the waveguide. By proper design of the grating parameters and a proper choice of the metal, these metal grating couplers reach the same efficiency as standard etched grating couplers. We show that the high index contrast inposed by the metal is the dominant factor in the working principle of metal grating couplers and that the inherent absorption losses can be minimized by controlling the aspect ratio of the grating teeth. We find that

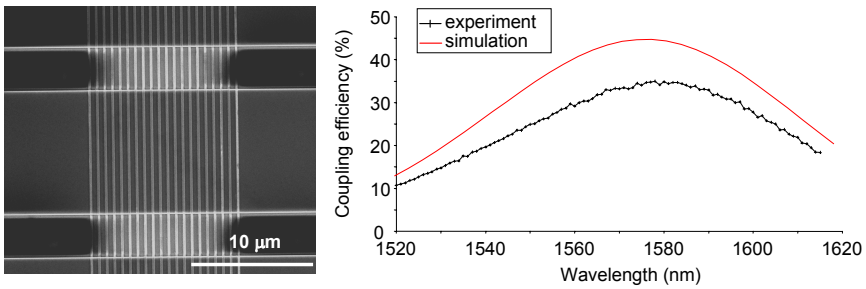

Figure 2: Efficient and broadband coupling between silicon-on-insulator waveguides and optical fibers by gold grating couplers fabricated with e-beam lithography.

very thin metal layers of only a few tens of nanometer thick suffice to obtain very high coupling efficiencies. Therefore, metal gratings are very interesting from a fabricational point of view while they hold potential for electronic integration. Prototype gold grating couplers on top of silicon-on-insulator (SOI) waveguides are fabricated using focused ion beam milling and e-beam lithography. The best results are obtained with e-beam lithography: a coupling efficiency of 34 % and a 1 dB bandwidth of 40 nm to a fiber tilted 10^o with respect to the vertical is demonstrated for a simple uniform grating coupler design. The experimental results agree well with simulation (see Fig. 2).

3 Polymer wedge for vertical coupling

Perfectly vertical coupling to photonic integrated circuits with grating couplers is not straightforward. From a fabricational and design point of view, out-of-plane coupling to a direction which is slightly off the vertical is much easier to obtain. However, from a packaging and assembling point of view, perfectly vertical coupling is much more appropriate. A simple approach to solve this problem is to make use of refractive elements on top of grating couplers to redirect the light from the slightly off-vertical towards the vertical direction, as depicted in Fig. 3. We demonstrate this principle by on-chip integration of polymer wedges and show that there is almost no penalty in terms of coupling efficiency. We also demonstrate a simple molding technique to define polymer wedges on optical fiber facets and demonstrate their usage for vertical coupling.

4 Metal-grating based optical fiber probe

Out-of-plane coupling is ideally suited for wafer-scale testing of photonic integrated circuits. However, the only components that are currently capable

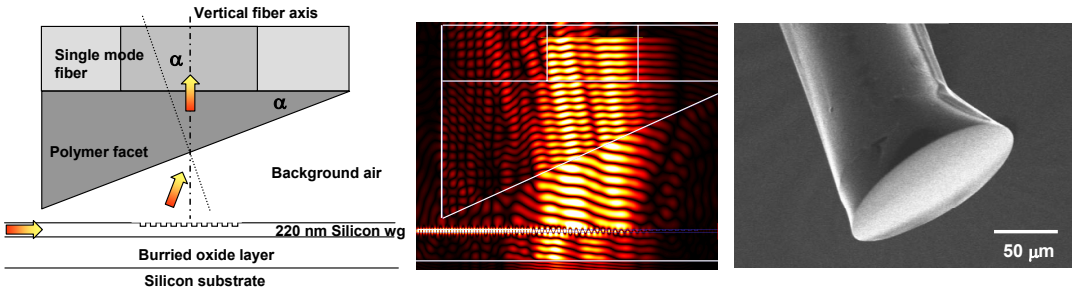

Figure 3: Perfectly vertical coupling between silicon-on-insulator waveguides and optical fibers containing a polymer wedge on the fiber facet.

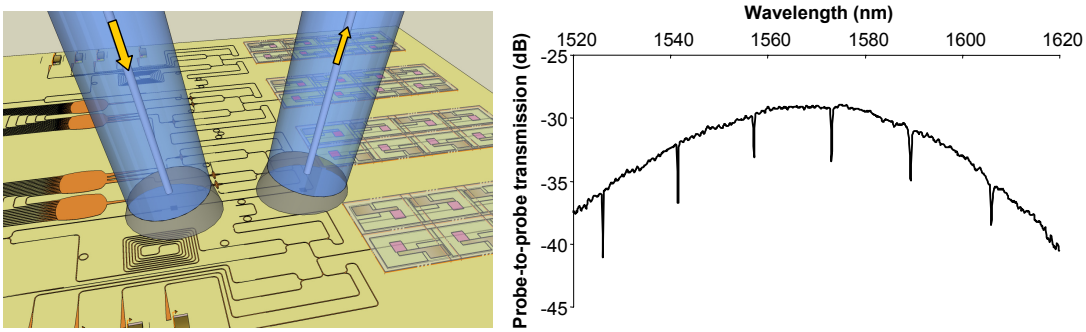

Figure 4: Two metal-grating based optical fiber probes used to test an integrated ring resonator: artist's impression and experimental demonstration.

of performing this type of coupling are grating couplers integrated into the circuit. Once integrated, the access points to the circuit are fixed and testing is limited to the circuit part that is terminated by those grating couplers. For future photonic integrated circuits with increasingly complex layouts a more flexible approach is needed for choosing the access points and for testing circuits, circuit parts and individual components. Our solution is to perform the testing by using optical fiber probes that include a grating coupler on the facet. A schematic is shown in Fig. 4. We fabricate prototype optical fiber probes containing a gold grating on the facet using a single-step nanoimprint and transfer method based on a hybrid silicon/gold mold containing a waveguide layer for accurate alignment. By making contact between a gold grating fiber probe and a 3 μm wide SOI waveguide, 15 % coupling efficiency is obtained, which is in good agreement to simulation results. Compared to existing optical fiber probes discussed in the literature, this is the only probe that combines out-of-plane coupling with a high efficiency and broadband coupling. Testing of integrated photonic components in SOI using two probes is demonstrated for the first time.

English Text

1 Introduction

IN this work, novel components for coupling to and probing of photonic integrated circuits are proposed and demonstrated. In this introductary chapter, we discuss the rationale behind this work and present the outline of this thesis.

1.1 Photonics

Over the past decades, we have witnessed how electronics and photonics have been infiltrating into many of our daily activities. Whether you drive a car, use your mobile phone or check your e-mails, electric and optical signals take care of the technology behind it. Miniaturization of electronic circuitry and efficient use of the fundamental property of light to carry information have been keys to unlock the vast amount of opportunities we have today.

1.1.1 Communicating with light

Exchange of information among people is more easy and more rapid than ever before. The reason is that we essentially make use of light signals to communicate and light is very fast. Today, all transport of information over long distances is taken care of by light signals of wavelengths around 1.3 μm and 1.55 μm, guided by optical fibers. These fibers are made of pure glass and have extremely little propagation loss, so that very little power is needed to send signals through. Moreover, they have good dispersion characteristics, which allows for the transport of very high bit rate signals. The principle of information transport through optical fibers is simple to understand. Suppose that one end of the fiber is connected to a laser source and the other end to a detector. Suppose the information is coded into a bit pattern, ie. a chain of zeros and ones. To represent a "one", the laser is switched on and to represent a "zero", the laser is switched off. At the other end of the fiber, the detector will detect the chain of light signals and interpret it as a chain of zeros and ones. The information is then retrieved by decoding the detected chain. Now, instead of using one laser, multiple lasers can be used, each operating at their specific wavelength and each carrying diffent bit patterns. In this way, many wavelength channels can be used simultaneously, thus boosting the capacity of the optical fiber. This technique, called wavelength division multiplexing (WDM), has played an essential role in the succes of optical fibers for telecommunication.

The installation of optical fibers started in the late 70s. Before that, information exchange was taken care of by electrical interconnections based on coaxial cables. However, those electrical connections have high propagation losses and could not stay in pace with the ever increasing bandwidth requirements for long-distance communication. Since then, the information capacity of fiber-optic systems has doubled almost every 2.5 years while at the same time the performance of fiber-optic components gradually improved. Moreover, the cost of fiber-optic systems reduced and came down to a level where it became profitable to replace electrical connections in shorter-distance communication networks too. As a result, these networks nowadays benefit also from the advantages of optical interconnections such as low power consumption and high

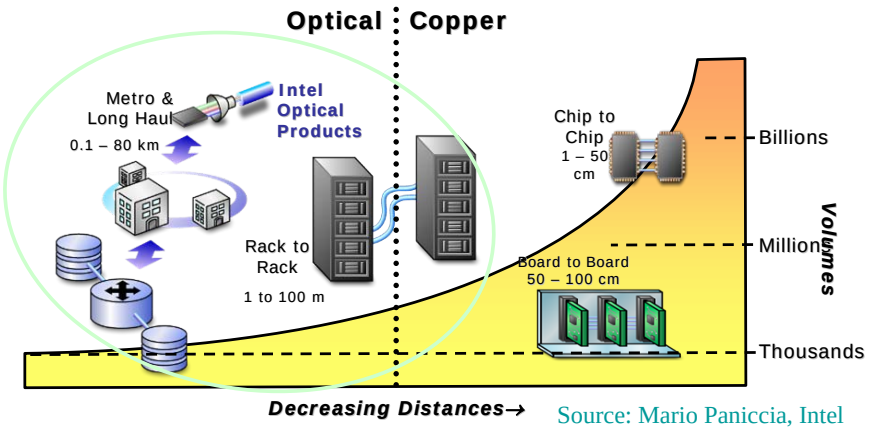

Figure 1.1: Moving towards photonic interconnections.

bandwidth. Even for very short distance communication (smaller than 100 m), optical interconnections are expected to break through.

Fig. 1.1 sketches the current use of optical and electrical connections as a function of communication distance and market volume. For wide-spread use of optical interconnections in very short distance communication, the required volumes are too high and the implementation too costly to be economically acceptable. The reason is that current optical interconnection systems are very complex and typically consist of an assembly of various components: multiplexers, demultiplexers, laser diodes, isolators, modulators, amplifiers, etc., each of them built and packaged seperately and placed into the big assembly as an individual module. In addition, each module has its own individual working principle, often consisting of an optical part and an electronic part, where the electronic circuitry takes care of the logical functions (ie. the processing of the chains of zeros and ones) to steer the optical elements. As a result, optical interconnection components are voluminous, power consuming and rather expensive (over 75 % is packaging cost). These factors in combination with the need for multiple optoelectronic conversions seriously limit the growth of optical interconnection.

Moving towards optical interconnections seems unavoidable as current short-distance communication solutions based on electric interconnections are meeting with fundamental physical limits with respect to the bandwidth they can offer. This becomes especially relevant for inter-chips connections in a computer and will become relevant for intra-chip connections. For years, manufacturers kept on adding transistors to a chip and boosted clock speed to keep up with bandwidth requirements. But this is now creating a situation where extreme amounts of power are being pumped into tiny spaces, which leads to increased signal interference, lower battery life-time in notebooks and more manufacturing defects. Although optical interconnections could in principle

lead to a solution, the size of optical interconnection components are currently incompatible with the size of electronic chips or transistors.

To tackle all of these issues, there is a strong drive towards miniaturization of photonic components and integration on a chip. By integrating multiple optical functions on a single chip, labour-intensive steps needed to optically align fibers and components are avoided, which reduces the cost of packaging considerably. Moreover, integrated devices can be made much smaller, lighter, less power consuming and multi-functional compared to the big assemblies used today. Also the multiple optoelectronic conversions may be reduced so that current communication systems can continue to increase in performance.

Communication is just one area where photonic integrated chips can make a difference.

1.1.2 Sensing with light

Today, sensors are being used and developed for a huge range of low-tech as well as high-tech applications. A lot of sensors are based on optical principles and consist of optical and optoelectronic components and CCD detectors to measure physical or chemical quantities. Spectroscopy is a widely used optical sensing mechanism. When analyzing the spectral properties of a beam of light that propagates through a medium like a gas or a liquid for example, molecular vibrations will lead to characteristic signatures in the absorption spectrum, and the composition of the medium can be retreived. Another mechanism is refractive index sensing, like surface plasmon resonance sensing where light propagation properties change due to molecules that attach to a gold layer.

The success of optical sensors is due to a number of distinct advantages that optical transduction mechanisms seem to offer over other mechanisms. They are electrically passive and thus free of any electrical interference. They can be made extremely sensitive by making use of resonating structures such as optical cavities with a certain resonance frequency that changes when there is a change in the environment (like strain, adsorbed molecules, temperature, etc ...). They can be used in high-voltage applications and harsh environments where electronic circuitry would not survive. Moreover, optical sensors lend themselves easily to multiplexing capabilities by using different wavelengths or polarization states of light.

Many optical sensor systems make use of optical fibers or an alternative kind of light guiding structures. In some applications even, the sensor is itself an optical fiber. In other cases, optical fiber is used to connect to a sensor at a remote location or connect different sensing elements along the length of the fiber in a multiplexed configuration using different wavelengths of light for each sensor.

Health care is the field which appears to contain the biggest potential for optical sensor development. Rapid, simple and low-cost medical devices for multiple parameter screening, which are used in the case of diseases and infectious illnesses, are essential for early diagnosis and improved treatments. A lot of the research effort in the field of sensors for medical applications is driven by the vision of a laboratory-on-a-chip. A lab-on-a-chip is a device that integrates one or several laboratory functions on a single chip of only millimeters to a few square centimeters in size. The concept of a lab-on-a-chip is expected to revolutionalize the field of medical diagnostics and introduce novel ways of patient managing using point-of-care and point-of-need diagnostic tools. Labs-on-a-chip are also expected to find numerous applications in other areas such as industrial process control, pharmaceutics, environmental monitoring, (bio)chemical analysis, etc.

A key factor for the successful breakthrough of lab-on-a-chip technology will be the ability to combine, miniaturize and integrate a high number of laboratory equipment and processes like cell lycing, sample amplification and dilution, sample cleaning, fluorescent labeling, process monitoring and optical detection into a compact system. Currently, all of these processes are carried out in a laboratory, which is slow, suffers from high fluid volume consumption (of water, reagents and sample volumes) and is therefore rather costly. On the contrary, labs-on-a-chip would have a fast response time, allow for massive parallelization due to compactness and would need only very low fluid volumes. The success of integration is for a great part also a cost-issue. The technology to produce labs-on-a-chip should be massively parallel so that low-cost fabrication is possible. As an example, the manufacturing price of a lab-on-a-chip for point-of-care diagnostics is economically valuable only when it can go down to the level where it becomes disposable.

The development of labs-on-a-chip is a highly multidisciplinary effort, requiring the integration of knowledge and technology from various fields and input from photonics and electronics as well as chemistry, micro- and nanofluidics and biosensing. The drive to miniaturize optical communication systems by integration of photonic and optoelectronic functions onto a chip is similar to the drive to miniaturize laboratories and sensing systems by integration of laboratory functions and sensor equipment onto a chip. In both fields, many challenges are still to be overcome. But it is clear that the ability to miniaturize complex optical functions by photonic integration within a fluidic platform expands the opportunities for labs-on-a-chip considerably.

1.2 Silicon-on-Insulator photonic integrated circuits

Silicon is available in high quality at relatively low cost and is the key material of electronic chips. Silicon is also a very suitable material for guiding infrared

light with a wavelength longer than 1.11 μm and thus a good candidate material for photonic chips.

Photonic chips consist of photonic integrated circuits in which waveguides are used to connect various photonic components such as filters, multiplexers, demultiplexers and resonators on the same chip to perform certain functions. A waveguide is a miniaturized equivalent of an optical fiber, ie. a structure that confines light within a certain area and transport it. In most waveguides, light is trapped in the core with a higher refractive index than the surroundings just as in the case of optical fibers.

Currently, the best performing photonic integrated circuits use silica waveguides that are integrated on a silicon carrier substrate. This material platform is called silica-on-silicon. However, because of the low refractive index contrast, these photonic integrated circuits are quite large. Smaller photonic integrated circuits can be made by choosing material platforms that provide a higher refractive index contrast. Examples are silicon oxynitride waveguides and silicon nitride waveguides, but the most promising one is Silicon-on-Insulator (SOI).

Silicon-on-insulator is a material platform with a very high difference in refractive index between the silicon core and the cladding (a difference of about 2). It is a membrane-type platform in which the top silicon waveguide layer with a thickness of no more than a few hundreds of nanometer is used as the guiding layer. Because of the high index contrast, light can be confined in a very small cross section and guide it through very sharp bends. In this way, photonic components can be made very small and various optical functions can be integrated on a compact area. Where conventional waveguides are typically much broader than 1 μm, SOI waveguides have dimensions of 500 nm or even less. These tiny waveguides are called photonic wires and are a basic building block in photonic components.

Figure 1.2 shows two examples of very compact components made in SOI: an arrayed waveguide grating for demuliplexing optical signals and a ring resonator for filtering light. The first one is an example of a key-component for communication, the second is an example of a key-component for sensing. These components contain sub-micron features and are fabricated using processes with an accuracy of about 10 nm. Therefore, these compact components are called nanophotonic components.

For SOI to become a suitable platform for photonic integration with widespread use in communication and sensing systems, various issues still have to be overcome. Nevertheless, for many of these issues solutions have been proposed and are being developed.

One of the important issues is the problem of integrating active functionality, such as light generation, modulation and detection into the circuit. This can be solved by making use of heterogeneous integration in which overlay materials are combined with SOI waveguides. By modifying the dimensions of the

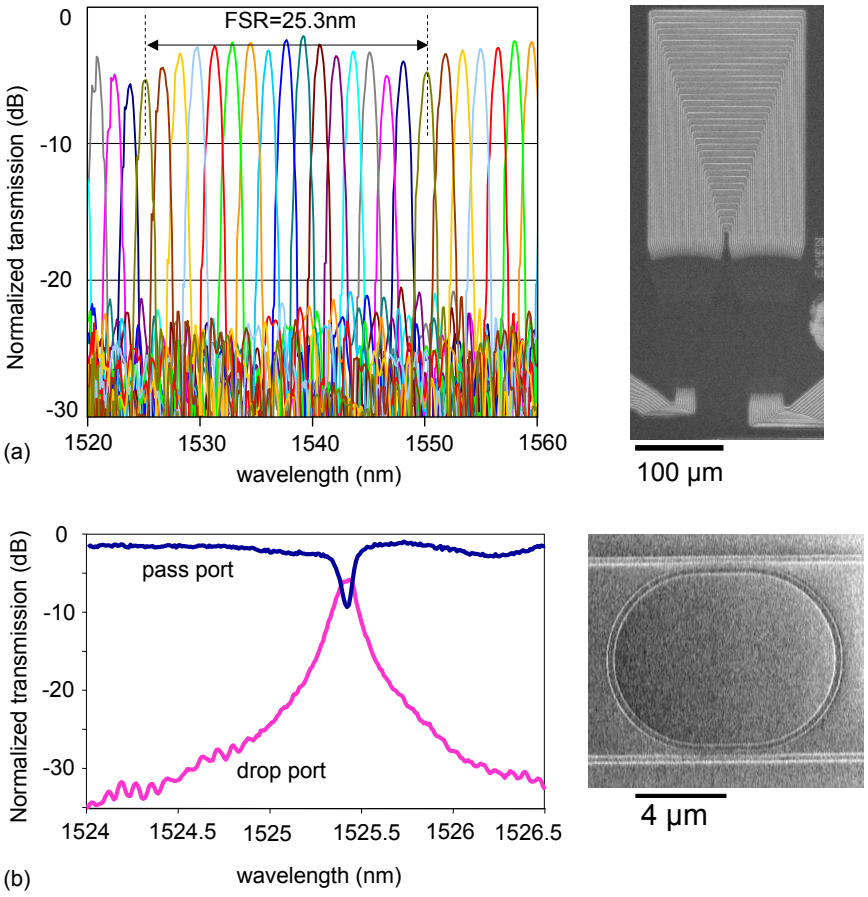

Figure 1.2: (a) SOI arrayed waveguide grating and (b) SOI ring resonator. Source: Pieter Dumon, Ghent University.

silicon waveguide the overlap of the optical field with such an overlay material can be tuned. In principle, many different overlayers can be integrated on the same chip.

Another issue is the problem of integrating electronic functionality. But this is not really a problem. In fact, SOI is the standard material for electronic circuitry and microelectronics manufacturing. Thus, from a material's choice point of view, the integration of photonic and electronic components and components for optoelectronic conversions is possible.

What may seem a problem at first sight is the large mismatch in mode size between existing fiber-optic systems and the waveguides in ultracompact photonic components. However, quite a number of solutions are being developed ranging from integrated tapers to convert between optical fibers and waveguides within the circuit plane to integrated surface couplers to couple out of the circuit plane, both with high efficiency and relatively high bandwidth.

Whether or not Silicon-on-Insulator will be the platform of choice for future optoelectronic modules or labs-on-a-chip cannot be foreseen and nobody knows the answer. Nevertheless, the above-mentioned arguments are strong arguments in favour of SOI. Another strong argument is the high level of maturity of silicon technology. Indeed, silicon technology - in particular Complementary Metal Oxide Semiconductor (CMOS) technology - outperforms any other planar chip manufacturing technology by orders of magnitude in terms of performance, throughput and reproducibility. Wafer-scale CMOS processes have a very high yield and once developed, they are amazingly reproducible across a wafer and from wafer to wafer.

Typical feature sizes of nanophotonic components are one tenth of the operation wavelength. For operation at a wavelength of 1550 nm for example corresponding to a wavelength in silicon of about 500 nm the required smallest feature sizes are typically between 50 and 500 nm. This matches nicely the capabilities of CMOS technology. The processes to define the basic waveguide structures in SOI nanophotonic circuits are compatible with front-end processes for fabricating CMOS and also provide sufficient accuracy. Moreover, as all processing occurs by means of wafer-scale processes on large wafers, CMOS fabrication is very cost-effective.

1.3 Challenges and future practice

In order to obtain a final lab-on-a-chip product or a module for optical interconnection or any other component, the fabrication of SOI photonic integrated circuit chips need to be followed by a number of extra manufacturing steps to include overlay materials and/or packaging features. Moreover, wafer-scale testing procedures need to be implemented to keep track of the quality of the

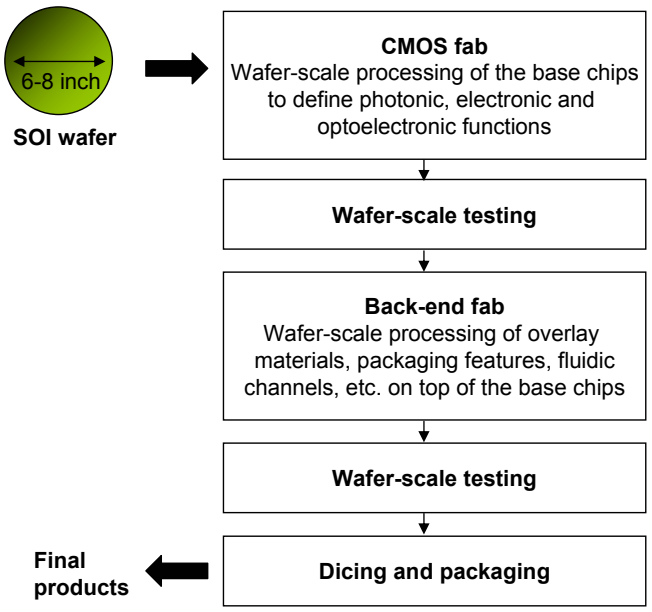

Figure 1.3: Possible process flow for the manufacturing of future devices based on SOI photonic integrated circuits.

fabricated chips during the subsequent manufacturing steps. A possible process flow for the future fabrication of photonic modules is depicted in Fig. 1.3.

The process flow of Fig. 1.3 is a future vision and not yet ready for implementation. In all of the stages of the manufacturing cycle, several issues still have to be overcome. One of the issues is to deal with the increasing complexity of devices when multiple materials are needed on a small scale to integrate different functions. This is challenging from a design point of view. Optimal exploitation of material properties will be necessary in possibly novel component architectures to deal with this challenge and facilitate integration.

Another issue is the testing of photonic devices. Typically, a fabricated wafer can count hundreds to thousands of photonic components, grouped on dies that are eventually separated and packaged into individual modules. Amongst other production control considerations, such as for improved packaging yield and quality control, it is necessary to carry out testing of the devices at the various stages of the fabrication process. An important problem is how to implement such a wafer-scale testing method.

A third issue is the packaging of photonic devices. It is expected that the cost of a final product will keep on being dominated by the packaging, as this is the case in current optical modules. So to keep device fabrication at a low cost, it is important that large part of the packaging can be taken care of by wafer-scale processes while the overall packaging scheme should be as simple as possible. Current surface couplers allow for vertical coupling, which is expected to allow for simpler and more straightforward packaging options.

But it remains a matter of debate whether these couplers are indeed suitable for packaging, certainly when it is recognized that the current coupling structures allow for near-to-vertical coupling rather than perfect vertical coupling.

Existing components, fabrication procedures and testing methods not only will have to be improved, novel concepts, components and procedures will need to be developed to deal with these issues. As we will see in this work, a possible key to unlock some of the problems regarding integration, packaging and testing of photonic devices, is to concentrate on novel components and integrate them on optical fibers rather than on chips. Such an approach opens quite some opportunities, but also requires the development of novel fabrication methods that can deal with the unconventional dimensions of an optical fiber as compared to wafers and chips.

1.4 Purpose and outline of this work

In this work we introduce novel components for coupling to and probing of SOI photonic integrated circuits based on a metal grating. To fabricate prototype components, we make use of novel techniques based on nanoimprint lithography. This emerging lithography technique not only holds the promise of an ultra-high resolution low-cost wafer-scale lithography process, it also provides flexible ways to structure chips and optical fiber facets, as we will see in this work.

The outline of this work is as follows. In chapter 2, we present the technologies for micro- and nanofabrication that will be used in this work. In particular, we introduce nanoimprint lithography as well as a number of nanoimprint-based techniques and apply them on chips and optical fiber facets. In chapter 3, we describe existing surface coupling techniques based on integrated grating couplers and illustrate the wider applicability of grating couplers to material platforms other than SOI. In chapter 4, we introduce a novel type of grating coupler - a metal grating coupler - and demonstrate its working for interfacing to SOI nanophotonic circuits. In chapter 5, the use of polymer and air wedges above grating couplers for perfectly vertical out-of-plane coupling is demonstrated. Finally in chapter 6, a metal-grating based optical fiber probe is introduced and demonstrated that allows for testing of individual SOI components using surface coupling. Its potential as a future wafer-scale testing probe is discussed.

1.5 Publications

The results obtained within this work have been published in various papers and presented at various conferences. This paragraph gives an overview of the

publications. They can also be found in the publications section of the photonics research group website: http://www.photonics.intec.ugent.be. These publications may be downloaded for personal use only. For any other use, the permission of the copyright owner (usually the publisher of the journal) must be obtained.

1.5.1 Publications in international journals

- S. Scheerlinck, J. Schrauwen, G. Roelkens, D. Van Thourhout, R. Baets, 'Vertical fiber-to-waveguide coupling using adapted fibers with angled facet fabricated by a simple molding technique', Applied Optics, 47(18), p.3241-3245 (2008)

- S. Scheerlinck, P. Dubruel, P. Bienstman, E. Schacht, D. Van Thourhout, R. Baets, "Metal grating patterning on fiber facets by UV-based nano imprint and transfer lithography using optical alignment", J. Lightwave Technol., in press.

- S. Scheerlinck, D. Van Thourhout, R. Baets, 'Flexible metal grating based optical fiber probe for integrated photonic circuits', Applied Physics Letters, 92(3), p.031104 (2008).

- D. Van Thourhout, G. Roelkens, R. Baets, W. Bogaerts, J. Brouckaert, P.P.P. Debackere, P. Dumon, S. Scheerlinck, J. Schrauwen, D. Taillaert, F. Van Laere, J. Van Campenhout, 'Coupling mechanisms for a heterogeneous silicon nanowire platform', Semicondcutor Science and Technology, 23, p.064004(9pp) (2008)

- U. Plachetka, A. Kristensen, S. Scheerlinck, N. Whitbread, J. Huskens, N. Koo, H. Kurz, 'Fabrication of Photonic Components by Nanoimprint Technology within ePIXnet', Microelectronic Engineering, 85(5-6), p.886-889 (2008).

- F. Van Laere, T. Claes, J. Schrauwen, S. Scheerlinck, W. Bogaerts, D. Taillaert, L. O'Faolain, D. Van Thourhout, R. Baets, 'Compact Focusing Grating Couplers for Silicon-on-Insulator Integrated Circuits', Photonics Technology Letters, 19(23), p.1919-1921 (2007).

- S. Scheerlinck, J. Schrauwen, F. Van Laere, D. Taillaert, D. Van Thourhout, R. Baets, 'Efficient, broadband and compact metal grating couplers for silicon-on-insulator waveguides', Optics Express, 15, p.9639-9644 (2007).

- P.P.P. Debackere, S. Scheerlinck, P. Bienstman, R. Baets, 'Surface plasmon interferometer in silicon-on-insulator: novel concept for an integrated biosensor: Reply', Optics Express, 15(21), p.13651-13653 (2007).

- P.P.P. Debackere, S. Scheerlinck, P. Bienstman, R. Baets, 'Surface plasmon interferometer in silicon-on-insulator: novel concept for an integrated biosensor', Optics Express, 14(16), p.7063-7072 (2006).

1.5.2 Publications in international conference proceedings

- S. Scheerlinck, R.H. Pedersen, P. Dumon, W. Bogaerts, U. Plachetka, D. Van Thourhout, R. Baets, A. Kristensen, 'Fabrication of Nanophotonic Circuit Components by Thermal Nano Imprint Lithography', CLEO/QELS 2008, United States, p.CFO2 (2008)

- S. Scheerlinck, D. Van Thourhout, R. Baets, 'UV-based Nano Imprint Fabrication of Gold Grating Couplers on Silicon-on-Insulator', 2007 Digest of the IEEE/LEOS Summer Topicals Meetings, United States, p.MB3.4 (2007)

- S. Scheerlinck, J. Schrauwen, F. Van Laere, D. Van Thourhout, R. Baets, 'Metal grating coupler for Silicon-on-Insulator, Annual Workshop of the IEEE/LEOS Benelux Student Chapter', Netherlands, p.17 (2007).

- D. Van Thourhout, W. Bogaerts, J. Brouckaert, P. Dumon, G. Roelkens, S. Scheerlinck, S. Selvaraja, J. Schrauwen, D. Taillaert, J. Van Campenhout, P. Bienstman, R. Baets, 'Silicon nanophotonics on CMOS', 33rd International Conference on Micro- and Nano-Engineering 2007 (MNE07), Denmark, p.113-114 (2007)

- S. Scheerlinck, F. Van Laere, J. Schrauwen, D. Taillaert, D. Van Thourhout, R. Baets, 'Gold Grating Coupler for Silicon-on-Insulator Waveguides with 34 % Coupling Efficiency', ECIO 2007, Denmark, (2007).

- S. Scheerlinck, J. Schrauwen, D. Taillaert, D. Van Thourhout, R. Baets, 'Efficient, broadband and compact metal grating couplers fo silicon-on-insulator',
CLEO/QELS 2007, United States, (2007).

- U. Plachetka, A. Kristensen, S. Scheerlinck, N. Whitbread, J. Huskens, N. Koo, H. Kurz, 'Fabrication of photonic components by nanoimprint technology within ePIXnet', MNE 2007, Denmark, (2007).

- S. Scheerlinck, J. Schrauwen, D. Van Thourhout, R. Baets, 'Metal grating for coupling to photonic crystal circuits',PECS-VII, United States, p.B-48 (2007).

- P.P.P. Debackere, D. Taillaert, S. Scheerlinck, K. De Vos, P. Bienstman, R. Baets, 'Si based waveguide and surface plasmon sensors', Photonics

West 2007: Silicon Photonics II (invited), 6477, United States, p.647719 (2007).

- S. Scheerlinck, D. Van Thourhout, R. Baets, 'UV-NIL with a DUV-fabricated silicon template as a flexible tool for nanopatterning',Micro- and Nano-Engineering 2006, 32nd International Conference, MNE 2006, Spain, p.121-122 (2006).

- P.P.P. Debackere, S. Scheerlinck, P. Bienstman, R. Baets, 'Surface Plasmon Interferometer in Silicon-on-Insulator: Novel Concept for an Integrated Biosensor', Group IV Photonics , Canada, p.7-10 (2006).

- K. De Vos, I. Bartolozzi, P. Dumon, S. Scheerlinck, W. Bogaerts, D. Taillaert, E. Schacht, P. Bienstman, R. Baets, 'Silicon-on-Insulator Microring for Label-Free Biosensing' , NanoBioEurope, France, (2006).

- S. Scheerlinck, D. Van Thourhout, R. Baets, 'Replication of SOI Photonic Structures by Nano-Imprintlithography', IEEE/LEOS Benelux Chapter, Workshop on Photonic Materials and Technology, Netherlands, p.16 (2004).

1.5.3 Publications in national conferences

- S. Scheerlinck, D. Van Thourhout, R. Baets, Nano imprint lithography for photonic structure patterning,Proceedings Symposium IEEE/LEOS Benelux Chapter, Belgium, p.63-66 (2005).

- S. Scheerlinck, Replication of submicron structures by nano-imprintlithography, 5th FTW PHD Symposium, Interactive poster session, paper nr. 17 (proceedings available on CD-Rom) , Belgium, (2004).

1.5.4 Patent applications

The work on the polymer wedges on chips and the work on the fiber probe were the subject of patent applications:

- S. Scheerlinck, D. Van Thourhout, R. Baets, 'Waveguide coupling probe and methods for manufacturing same', International Patent Application PCT/EP2008/058330, 27/06/2008.

- J. Schrauwen, S. Scheerlinck, G. Roelkens, D. Van Thourhout, R. Baets, 'Integrated Photonic Devices Including Refractive Elements and Methods of Coupling Light Between an Integrated Photonic Waveguide and an Optical Element', US Provisional Patent Application 61054401, 19/05/2008.

2
Nanopatterning techniques

TAILORING the properties of materials by micro- and nanostructuring is an active domain of research. Various techniques exist to structure different kinds of materials at the micro- and nanoscale. Bottom-up approaches make use of chemical reactions to produce particles of a certain material or combination of materials. Top-down approaches use lithography to produce the desired patterns into specific materials. In this work we focus on the top-down approaches. In this chapter we give a review of methods and techniques that were used and developed in this work. Among others, we focus on nanoimprint lithography as a novel flexible approach for micro- and nanopatterning of chips and optical fiber facets.

2.1 Introduction

The electronic chip manufacturing industry is the most important user of lithography systems for high volume fabrication of integrated circuits. Moore's law predicts that the number of transistors on a chip doubles each two years and the industry is continually investing to stay in pace. Partly because of the insight that optical lithography is reaching its resolution limits and partly because of the urge in research to have access to more flexible techniques than the slow direct write approaches for micro- and nanopatterning over large areas, novel alternatives have been developed over the past decade. One of them is nanoimprint lithography. Nanoimprint lithography is essentially a molding technique and is in principle very simple and very flexible. Although nanoimprint lithography is still in a developing stage - certainly with regard to high volume fabrication of electronic circuitry - it offers a number of very promising opportunities in other application areas where not so much the resolution but the flexibility with respect to materials and substrates and the ease of processing are key properties.

In this chapter, we show that nanoimprint is a very suitable technique, capable of high resolution two-dimensional as well as three-dimensional patterning. We discuss the potential of novel NIL-based processes for integrated photonics. In particular, we offer a nanoimprint based solution to the problem of structuring very small facets such as optical fiber facets.

2.2 Nanopatterning techniques

We begin this chapter by giving a review of the basic principles of conventional processing techniques to define micro- and nanoscale patterns on a substrate. We start with the direct write techniques that are the principal workhorses of the research community. Then comes optical contact lithography and optical projection lithography, which is the principal technique of the industrial chip manufacturing community. We conclude this section by a literature overview of the described techniques for micro- and nanoscale patterning of small facets.

2.2.1 Principles of lithography

Micro- and nanostructures for photonic, electronic or biochemical applications have a typical smallest feature size of a few tens to a few hundreds of nanometers. The accuracy with which the structures have to be fabricated depends largely on the application. For nanophotonic components, it is of the order of 10 nm or even less, especially when wavelength-selective functions are involved.

Many photonic or electronic components are fabricated by a combination of lithography and etching: the patterns of the structures are defined into a sensitive resist layer. Once the resist pattern is ready, the actual structuring of the material can start. There are two main approaches. The first approach is to use the patterned resist as an etch mask for the underlying substrate. The transfer of the pattern into the desired material is done with wet etching (mostly for low resolution patterns) or anisotropic dry etching (mostly for high resolution patterns). The second approach is to use the patterned resist as a template for material deposition and lift-off. Once the material is deposited, the substrate is put in a solvent lifting the material on top of the resist structures off the substrate and leaving the rest of the material. For more complex components, a combination of these approaches and various other techniques are widely used. In the following we will focus on the pattern definition.

2.2.2 Direct write lithography

2.2.2.1 Electron beam lithography

With electron beam lithography, commonly referred to as e-beam lithography, a focused electron beam scans over an electron sensitive resist on a substrate, as is illustrated in Fig. 2.1. Depending on the type of resist (positive or negative) the pattern written by the electron beam will stay or will dissolve upon development. The primary advantage of electron beam lithography is its ability to make features in the sub-micrometer and nanometer regime with very high accuracy. This is because the beam width at the focus point of an electron beam can be made as small as a few nanometer and because electron beam resists have well-suited properties that allow the defined feature sizes to be maintained throughout the scanning and development process. Well-known resists are Poly(Methyl Methacrylate) (PMMA) and Styrene Methyl Acrylate based resist products, commercialized by Zeon Corporation (ZEP-series). They are spin-coated onto the substrate prior to the electron beam lithography process.

Electron beam lithography is very flexible. It is too slow for mass production but very attractive for the fabrication of prototype devices. For this purpose it is extensively used by the research community and is widely applied on a variety of substrate materials and sizes.

We note that scanning electron microscopy (SEM) uses the same mechanisms as e-beam lithography but relies on detectors to capture secondary electrons that are radiated back from the surface when it is hitted by an electron beam. SEM is the primary tool for characterization of materials and patterns that are too small for optical microscopy.

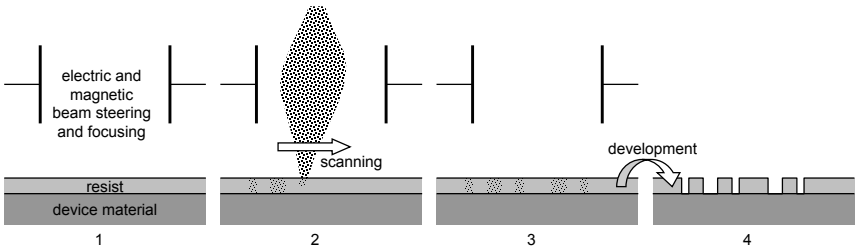

Figure 2.1: E-beam lithography: (1) setup, (2) writing of the pattern with a scanning electron beam, (3) definition of the pattern in the resist and (4) the result after development.

2.2.2.2 Focused ion beam milling

The necessity of a resist layer in e-beam lithography is an important drawback for two reasons. First of all, it limits the use of e-beam lithography to fabrication of planar structures and second, the fabrication process has to rely on classical etching tools using the patterned resist as a mask, making optimization processes more difficult and slowing down fabrication runs.

Initially developed as a diagnosis instrument for semiconductor industry, Focused Ion Beam (FIB) milling is one of the most promising direct-write technologies. FIB milling consists in scanning a focused ion beam over a sample surface for direct etching. The ions are extracted from a liquid metal source (generally gallium), accelerated, deflected and focused on the substrate. The desired pattern is defined by scanning the beam over the surface in a controlled manner (Fig. 2.2). Unlike e-beam lithography, a focused ion beam allows to sputter away any material with a resolution between 10 and 100 nm. In addition, gas molecules may be dissociated near to the writing field, resulting in etch enhancement or a deposition of materials.

FIB milling enables the fabrication of very complex geometries. For example, by tilting the sample one can etch slanted holes or angled slits. By tuning the beam current one can etch less or more deeply into the substrate, allowing for three-dimensional structures. And when a machine with an electron beam as well as an ion beam is used, one can directly inspect the fabricated device using SEM, which can greatly accelerate process optimization. Moreover, SEM allows for alignment of the focused ion beam to underlying structures.

Focused ion beam lithography is inherently destructive. Ion implantation and material amorphization take place during focused ion beam milling and cause large optical losses in dielectric materials. Although techniques have been developed to limit the damage and reduce optical losses, it can not be prevented completely without the introduction of buffer and mask layers that prevent the ions of directly hitting the substrate. We will come back to this issue in chapter 4.

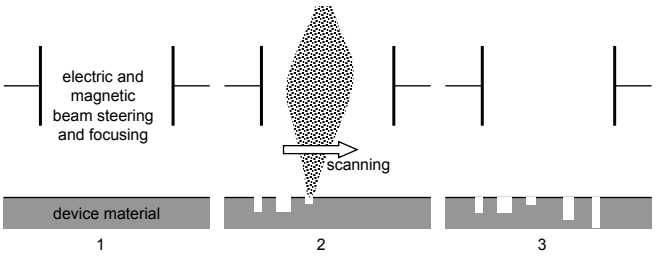

Figure 2.2: FIB milling: (1) setup, (2) drilling the pattern with a focused ion beam, (3) the pattern is directly defined in the substrate.

Although very high current densities are possible (315 Acm^{-2}) the corresponding small spot sizes (10 to 500 nm) make it a very time consuming process to mill out large volumes of material. For example, when using a beam current of 1 nA it takes 60 min to mill out a volume of 50 m^{-3} in silicon [1]. One approach to enable large numbers of FIB milled shapes to be produced would be to use the FIB system to mill either embossing tools or moulds. Although the initial FIB milling would be time consuming, these could then be used in a mass production process. We will come back to this approach in a later section.

In this work, we made use of a Novalab Dual-Beam 600 system (FEI), equipped with a 30 keV gallium beam with minimal spot size of 10 nm and a 30 keV electron beam with a minimal spot size of 3 nm.

2.2.2.3 Excimer laser ablation

Excimer laser ablation is another direct-write technology that does not require a resist. Although the processes are fundamentally different, the principle of excimer laser ablation resembles the one of focused ion beam lithography. In excimer laser ablation the beam of an excimer laser with emission wavelength typically in the range of 157 to 355 nm is focused onto the substrate so that the energy is sufficient for local thermal dissociation or photochemical decomposition of the material. Given that most polymers feature a low thermal conductivity and extremely high UV absorption, excimer laser ablation is especially suitable for micropatterning of polymers with micron and even submicron accuracy.

Compared to e-beam lithography and focused ion beam milling, excimer laser ablation has a much lower resolution. The structures made by ablation have typical sizes of a few tens to a few hundreds of micrometers. Nevertheless, excimer laser ablation allows for the fabrication of a variety of structures which do not need the resolution offered by e-beam or focused ion beam technology. In particular, excimer laser ablation is ideally suited for rapid prototype-fabrication of three-dimensional micro-optical structures such as lenses, wedges, via-holes, fiber support structures, etc. as well as lab-on-a-chip

structures such as channels and fluid capillaries or micro-alignment structures. All of these structures can be fabricated in a top polymer layer of a heterogeneous photonic or opto-electronic module in a late phase of the assembly process [3]. Fabricating the same type of devices by e-beam or fib would be possible but extensively time-consuming and unnecessary because of the low resolution needed for these applications.

All three direct-write technologies are serial processes and thus ideally suited for prototyping, but they lack the high throughput needed for fabricating a large number of devices in a reasonable time frame. To obtain a higher throughput, parallel processes such as optical lithography techniques are much more suitable. These techniques will be the subject of the next section.

2.2.3 Optical contact and projection lithography

Optical lithography is the most widely used technique to define various types of planar structures and patterns. Fig. 2.3 and 2.4 illustrate the principle of optical contact lithography and optical projection lithography respectively. They are both parallel processes and make use of a mask in which the two-dimensional geometry of the desired structures is defined. The mask pattern is then defined into a photosensitive resist layer applied on top of the substrate by UV-irradiation through the mask. Either contact is made between mask and resist, or a projection system is used. Upon development, the irradiated regions (or non-irradiated regions depending on the type of resist: positive or negative) will stay and the resist pattern can be used as a mask for etching the substrate or as a template for patterning another material by a lift-off process.

The resolution of optical lithography is dependent on a number of factors. The main limitation is imposed by the illumination wavelength: the shorter the wavelength, the smaller the features that can be defined. For conventional photonic structures for example defined by optical contact lithography, wavelengths in the optical or near UV range are used. Typically, this limits the feature size for dense features to approximately 600 nm. For this work, we had access to an MA-6 Mask Aligner tool (Suss MicroTec).

Patterns of higher resolution require shorter wavelengths within the deep UV region. They can be defined by using Deep UV (DUV) lithography at wavelengths of 248 nm, 193 nm or 157 nm. Possibly in the future 15 nm, known as extreme UV lithography will be used. However, the optics for DUV lithography need to be of very high quality to deal with these short wavelengths. Therefore, DUV lithography systems are very expensive, require a huge initial investment and are only available to industries with a sufficient market potential, as is the case with advanced CMOS components. For these large-volume applications, DUV lithography is the most attractive technology

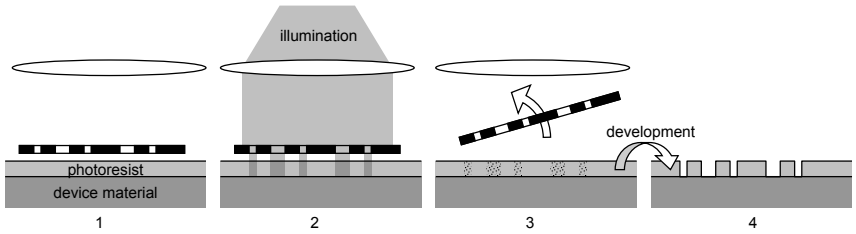

Figure 2.3: Optical contact lithography: (1) alignment of the mask with respect to the substrate, (2) UV-exposure through the mask, (3), unloading of the substrate and (4) the result after development.

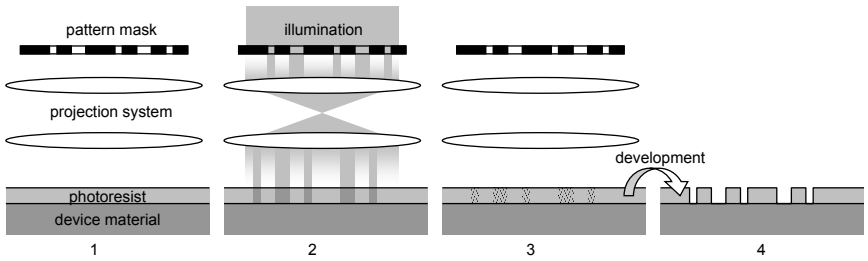

Figure 2.4: Optical projection lithography: (1) alignment of the mask with respect to the substrate, (2) UV-exposure through the mask, (3) unloading of the substrate and (4) the result after development.

because of its high throughput and sufficiently high resolution at acceptable working costs. 193 nm DUV lithography is the current standard lithography process for silicon-based CMOS fabrication.

In the case of optical contact lithography, the whole wafer is illuminated in one step with a one-to-one relation between the mask feature sizes and the resist structures. In DUV lithography, DUV-steppers illuminate one die at the time and step over the wafer in a grid-like pattern with a four times reduction between the mask structures and the final structures. It is advantageous to work with four times larger structures on the mask as this relaxes the required accuracy and limits the cost of mask fabrication. In this work, we had access to DUV lithography systems via the ePIXnet silicon photonics platform that uses the CMOS fabrication equipment of IMEC (Leuven, Belgium) and LETI (Grenoble, France) for the structuring of 200 mm and 300 mm SOI wafers [4].

CMOS technology has reached a level of maturity that outperforms any other planar chip manufacturing technology by orders of magnitude in terms of performance, throughput and reproducibility over a very large wafer area. That includes the CMOS etching processes that have been optimized towards extremely high interface smoothness. The processes, once developed, are amazingly reproducible across a wafer and from wafer to wafer [5]. This will continue to be the case for whatever processes that will be used for CMOS fabrica-

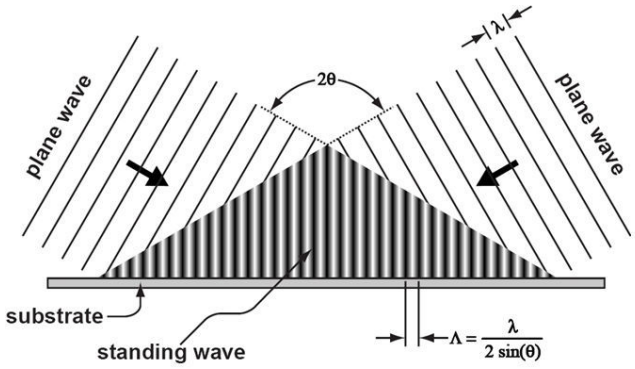

Figure 2.5: Optical interference lithography: schematic of the interference principle [2].

tion, including immersion lithography or extreme UV lithography. This is an exclusive advantage of using CMOS technology for nanopatterning.

However, some disadvantages should be addressed. First of all, optical lithography techniques are essentially planar techniques. This implies that the three-dimensional patterning capability that is offered for instance by focused ion beam milling and excimer laser ablation is far from trivial. It is only possible in a layer-by-layer approach whereby multiple subsequent processing steps of resist exposure and etching whereby each of the subsequent patterns should be carefully aligned to each other. In fact, a simple high throughput alternative for three-dimensional patterning apart from CMOS-based techniques does not exist. Second, CMOS equipment is very inflexible in terms of materials and substrates. They cannot be chosen freely. A CMOS fab only accepts wafers of specific well-defined dimensions and made of specific materials. That material is normally silicon, only accepted in the form of large wafers. This makes DUV-lithography a very inflexible technique. This issue will be covered further on.

As a final remark, we note that optical techniques can also be used to define high resolution submicron scale patterns without the use of a mask. These techniques are based on interference of waves (see Fig. 2.5) to define a periodic pattern in a photoresist. This enables the fabrication of one-dimensional as well as two-dimensional patterns over large areas.

2.2.4 Structuring fiber facets

Fiber facets are very small substrates of a diameter no bigger than 125 μm. This is slightly more than the average width of a human hair. As a consequence, any attempt to adapt or structure fiber facets goes with practical difficulties. The lithography processes described above are well studied and documented for chip-size and wafer-size substrates. For very small substrates such as fiber

facets, the processes are much more driven by the specific application and less well studied. In this section, we discuss various technologies reported in the literature to structure fiber facets at the micro-and nanoscale.

2.2.4.1 Fiber cleaving and fiber polishing

Flat fiber facets are obtained by fiber cleaving. Cleaving is usually done by using the so-called score-and-bend technique whereby the fiber is slightly bent after creating a small initial crack. Due to the bending, the crack opens up and propagates through the fiber, thus cleaving the fiber and leaving a flat end facet. Mechanical cleaving tools have a sharp blade typically made of diamond or tungsten carbide to produce the initial crack. An alternative way to produce the initial crack, is by using an excimer laser. Despite the fact that silica glass is fairly transparant for the UV excimer wavelengths, when used in a short pulse regime, ablation phenomena take place and a selective ablation of the glass in the form of a small rectangular cavity can serve as the fracture initiator [6]. By controlling the bending of the fiber, the propagation of the crack through the fiber can be controlled. Although - in principle - angled facets can be produced, the control of the angle is very difficult and these methods are thus most widely used to produce flat facets.

In optical communication systems, facet quality is critical for ensuring low reflectance terminations and for enabling optimal optic performance. Moreover, more sophisticated facet structures than flat facets are often needed. As an example, efficient coupling between laser diodes and single mode fibers require wedge-shaped fiber [7] ideally consisting of a quadrangular-pyramid-shaped structure [8]. Such fiber ends are made by fiber polishing. Fiber polishing requires a fiber holder and a rotating polishing table (see Fig. 2.6). The fiber is mounted at the desired angle and pushed down onto the rotating polishing table to polish the fiber by friction. For polishing multiple wedges, the fiber can be rotated in between subsequent polishing runs. Fiber polishing is a very delicate process and requires automated steering of the applied force in order to prevent fiber breaking during the process and in order to control the fabricated angle of the wedges. As an alternatively, the use of CO_2 lasers has been explored and has been shown to be interesting for decreasing the surface roughness of fiber ends [9] and cutting of angled facets [10]. However, thermal effects limit the applicability of these lasers to cutting. As a result, shaping of the fiber end with multiple wedges is not feasible.

2.2.4.2 Focused ion beam versus electron beam lithography

Direct-write technologies such as FIB milling and e-beam lithography are very attractive to structure fibers as they offer both design freedom and a very high

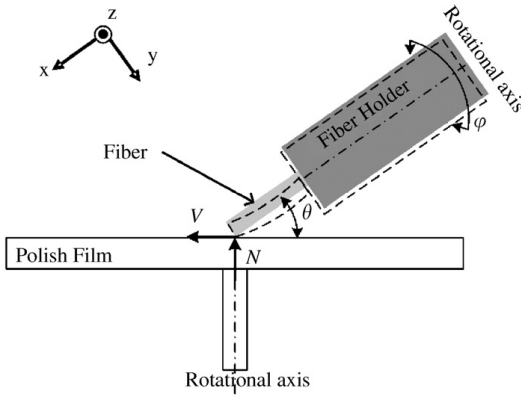

Figure 2.6: Schematic of a fiber polishing setup to produce angled facets. Figure reproduced from [7].

resolution. In particular, FIB milling allows for direct etching of core as well as cladding material of the fiber without the need for any resist.

The most well-known application of FIB milling of fibers is the fabrication of aperture optical fiber probes for Scanning Near-field Optical Microscopy (SNOM). The fabrication of fiber probes for aperture SNOM basically consists of three steps. First, the fiber is processed to obtain a taper with a sharp apex. This is usually done by selective chemical etching in HF solutions whereby core and cladding have different etching properties [11]. Other techniques such as the heating-and-pulling method also exist but are less interesting as they do not allow for accurate control of the taper cone angle [12]. Second, the fiber taper is coated with a metal such as aluminum to avoid light leackage and to increase the amount of light that will emerge from the aperture. In the third and final step, FIB is used for defining the aperture at the fiber apex [13].

Another application of FIB is the definition of metal nanostructures on small facets, a technique which has been adapted to fiber facets only recenlty. In particular, FIB has been demonstrated for the definition of very small sub-50 nm diameter apertures in a metal coating on the facet of a semiconductor laser source to obtain very high field confinement [14]. FIB has also been demonstrated for the milling of a plasmon nanoantennas which is an even more promising approach to obtain high confinement as it can be combined with field enhancement due to the resonant behaviour of the antenna [15]. Potential applications are in the field of data storage, near-field optical microscopy, spatially resolved spectroscopy and ultra-small photodetectors [16]. FIB-milled gold nanorod assemblies have recently been demonstrated on fiber facets with potential applications in biosensing [17], the principle of which is based on surface plasmon coupling (see Fig. 2.7). However, FIB milling leads to implantation and amorphization of the substrate by the gallium ions and influences the optical properties of the substrate, as we mentioned before. Although ex-

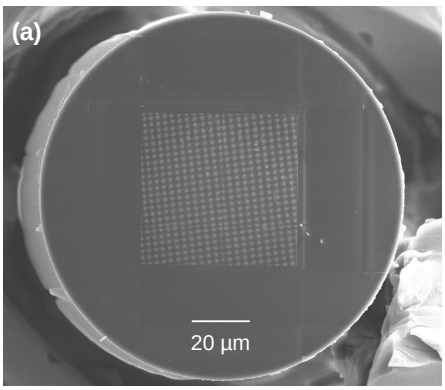

Figure 2.7: Surface plasmon resonance based fiber sensor layout. The gold nanopattern is fabricated by FIB milling. Figure reproduced from [17].

perimental work on ITO-coated glass samples have proven the principle of the technique, the optical response of the fiber optic sensor fabricated by FIB has not yet been demonstrated because of the high absorption at visible wavelengths after FIB milling [18].

An alternative to FIB for the structuring of fibers is e-beam lithography. However, the requirement of a resist scheme is a serious complication for this type of substrates. Indeed, spin-coating on a fiber facet is extremely difficult. Solutions whereby short-cleaved fiber pieces are mounted in special chucks with narrow grooves have been proposed such that the facets are at the same level as the chuck surface, thus virtually enlargening the fiber facet area to a more conventional size, but the results were problematic [19]. On the contrary, solutions based on dry resist schemes have proven very successful. In this case, the resist is deposited in high vacuum by thermal evaporation and allows the resist to be applied with a homogeneous thickness without any restriction on substrate size. E-beam writing using an e-beam sensitive sterol followed by etching was successfully demonstrated for defining high resolution features down to 100 nm on laser diode facets and fiber facets [20].

For both FIB milling and e-beam lithography, charging of the electrically insulating fiber glass is an important issue. The charge build-up process can be inhibited by using a thin chromium layer onto the facet which also partially covers the outer cylindrical surface of the fiber, so enabling good electrical contact of the fiber with the fiber holder.

A drawback of any direct-write technique is that it is rather slow and thus only suitable for prototyping. In an attempt to come up with a wafer-scale microfabrication process of SNOM probes, an interesting technique was proposed in [21]: FIB milling is only used for defining the nanoscale feature of the aperture while all other fabrication steps are carried out by by wafer-scale processes. The fabrication starts with the fabrication of probe moulds in $\langle 100 \rangle$ silicon substrate using KOH, resulting in an inverted sharp pyramidal tip apex.

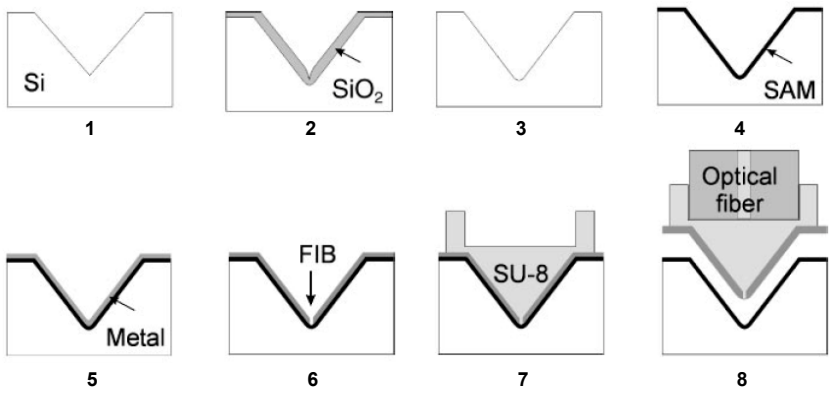

Figure 2.8: Process flow for fabrication of SNOM probes using a combination of molding and FIB: (1) inverted tip shape definition on mold, (2) mold shape control by oxidation, (3) oxide layer removal, (4) anti-adhesion layer treatment (see section 2.3.3, (5) metal deposition, (6) nano-aperture opening by FIB, (7) polymer probe structuring and (8) optical fibre bonding and releasing from mold [21].

This is followed by an anti-adhesion treatment, metal evaporation and FIB-milling of the aperture in the evaporated metal. Then a photoresist is spin-coated and structured by lithography to form an optical fiber holder in which the fiber is placed to attach the tip to the optical fiber. The process flow is depicted in Fig. 2.8.

As a final remark, we point out that both FIB milling as well as e-beam lithography processes require multiple fiber handling steps. Fibers are rather delicate to handle and a low number of processing steps that require less critical handling is important to increase the yield in any fabrication scheme involving optical fibers. From this point of view, the mould approach we mentioned is the most interesting approach as all critical processing is done on a chip or wafer prior to fiber attachement. However, for keeping the number of processing steps as low as possible, a number of alternative solutions have been proposed in the literature.

2.2.4.3 Alternative solutions

We describe two different fiber optic applications very much related to the applications mentioned before where patterning of the fiber facet is carried out using an alternative fabrication technique. The first application is a surface plasmon resonance gold nanoparticle based fiber sensor [22]. By surface treatment of the fiber facet using N-(2-Aminoethyl)3-aminopropyltrimethoxysilane and subsequent immersion in a gold nanoparticle solution, gold nanoparticles are immobilized onto the fiber facet covering $\pm$ 20% of the surface area . A second application is a fiber with a microlens on the sidewall to be used as

a probe for compact optical data storage [23]. The fiber is immersed in photoresist and the photoresist is cured by UV-light guided by the fiber, thus only exposing a small portion of the photoresist determined by the width of the core. A microlens of width 16 μm and height 5 μm is then formed by optimized thermal reflow.

Unlike FIB milling and e-beam lithography these alternative solutions for fiber facet structuring require much less delicate fiber handling. However, the type of structures that can be obtained and the design freedom is extremely limited. We will now introduce a novel micro- and nanostructuring technique which has attracted a lot of attention in recent years and which will be proof to be very useful for the patterning of fiber facets.

2.3 Nanoimprint lithography based techniques

2.3.1 Introduction

Features sized 100 nm and less are difficult to fabricate. Flexibility is a key point. With flexibility is meant flexibilty towards choice of materials, choice of substrate shapes and sizes (flat, non-flat, small, big, etc ...) and general practical use. Optical lithography methods used in microelectronic manufacturing industry are being driven by an extremely targeted industry and are characterized by a serious lack of flexibility. This is even more true in view of the recent developments in optical lithography techniques that allow for fabrication in the sub-100 nm domain. Immersion lenses, angular illumination, phase shifted masks, etc. introduced to or considered for Deep UV-lithography systems make these lithography methods even more costly and likewise less practical for general use. Direct-write techniques offer this type of flexibility but there is a considerable penalty in the throughput. The trade-off between resolution and throughput for various patterning technologies can be seen in Fig. 2.9: the higher the resolution, the lower the throughput.

Nanoimprint lithography is essentially a molding technique and is in principle very simple and very flexible. Nano Imprint Lithography and related techniques have been developed in the past decade out of a need for alternative solutions for high resolution definition of patterns at low cost, in a flexible way and without the throughput penalty. A mold can be made using expensive technologies while the NIL process itself is low-cost and may allow for high throughput. These techniques are very accessible and allow for prototyping and process development. Moreover, it allows fabrication of nanopatterns up to a level of throughput compatible with some degree of manufacturing. Nano Imprint Lithography was pioneered by S.Y. Chou and co-workers [26] and offers an appealing approach for high resolution patterning beyond the resolution limits imposed by optical lithography and with high through-

put. The principle of Nano Imprint Lithography is shown in Fig. 2.10. In principle, it is an update of the hot embossing process used to make copies of relief structures such as compact disks. Rather than forcing a pattern in a bulk plastic substrate, however, the imprint is made in a thin film of thermoplastic polymer using a combination of heat and pressure. In this process, even the smallest features of only a few nanometer in size are faithfully replicated. Instead of thermoplastic polymers, also photoplastic polymers can be used. This was already recognized back in 1989 by Okai and co-workers [27] who demonstrated the use of UV-curable polymers to produce optical transparant gratings with grating periods of 240 nm. The technique of Nano Imprint Lithography with UV-curable polymers is nowadays called UV-NIL.

Nano Imprint Lithography is essentially a molding process. Various aspects of the process, such as surface modification, mold material and fabrication, polymer flow, curing cycles, composition of imprint polymers and resists, pattern transfer steps, etc. have been the subject of a wave of research papers and commercial ventures. Since Nano Imprint Lithography was placed on the International Technology Roadmap for Semiconductors as a potential lithography solution at the 32 and 22 nm fabrication nodes [28], a lot of effort is being put into the development of Nano Imprint Lithography for microelectronic circuit manufacturing, which necessitates the study and improvement of Imprint Lithography infrastructure for template fabrication, imprint on a wafer-scale, overlay accuracy and defect control. Both thermal as well as UV-NIL have proven capable of patterning transistors for electronics applications [29], [30], [31].

Given its flexibility Nano Imprint Lithography is being explored for a variety of other applications in addition to integrated optics and electronics. An exhaustive list is beyond the scope of this work, but a few highlights are worth mentioning. Magnetic memory [40], [41], sensors [42], biomedical applications [43], [44], plastic electronics [45], organic thin film transistors [46], and high resolution organic light emitting diodes [47] have been demonstrated.

In all these cases, the desired structures are made by pattern transfer of the nano-imprinted polymer into the underlaying substrate, followed by a number of post-processing steps such as lift-off or etching if necessary. However, Nano Imprint Lithography also offers the potential of fabricating the desired structures by a single imprint step without post-processing or pattern transfer. In this case, the imprinted pattern *is* the functional device. Although direct imprinting of hard materials such as silicon was investigated [33], most of the work is found in the field of integrated optics and photonics using polymers. Fabrication of passive optical components including polymer waveguides, photonic crystal devices, [34] and ring resonators [32] has been demonstrated. More recently, active components such as distributed feedback lasers [36], [37] and photonic crystal band-edge lasers [38] have been reported. A very interesting approach is to integrate lasers and waveguides with mi-

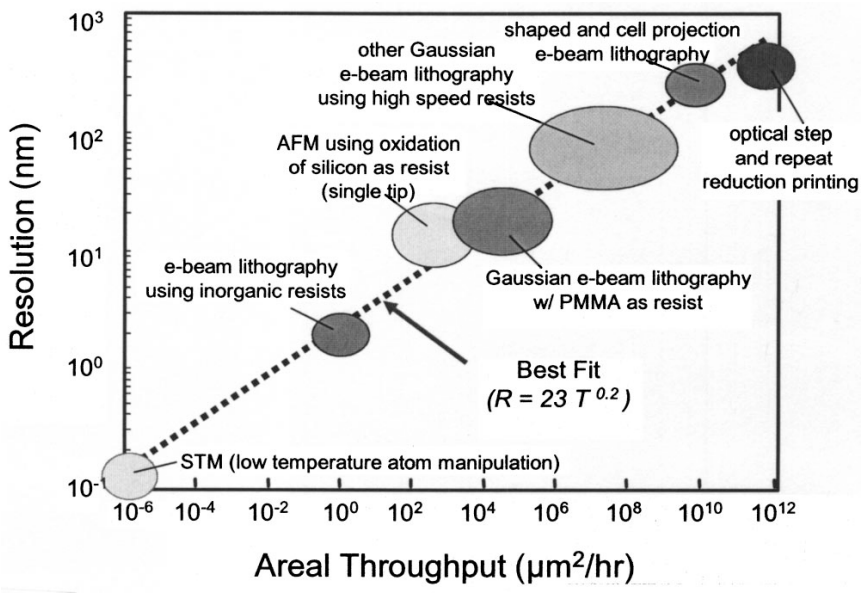

Figure 2.9: Trade-off between throughput and resolution [24], [25].

crofluidic functionality on the chip [39]. Even more interesting in this context, is the ability of NIL to define three-dimensional structures, e.g. structures with more than two levels, such as wedged areas or curved patterns on a wafer scale [80]. Unlike nanoimprint lithography, all conventional wafer-scale lithography techniques are essentially two-dimensional. Fabrication of 3D structures would thus require multiple exposures and/or etching steps. Although 3D patterning with nanoimprint is widely recognized as a very promising approach, to date it has remained largely unexplored.

Printing is a slightly different approach. Micro Contact Printing (often referred to as μCP) with soft elastomeric stamps containing micron-sized relief structures ”inked” with a self-assembled monolayer (SAM) of hexadecanethiol on gold [49] was demonstrated back in 1993. Further developments of this technique have been reported including the printing of sub-100 nm sized metal patterns directly on silicon [50] and the printing of protein arrays for biofunctional surfaces [51].

The potential of both molding and printing by Micro or Nano Imprint and Print Lithography have triggered a lot of interest in various alternative techniques that utilize a template (mold/master) in one way or another. It is clear from the above description that these techniques find applications in a wide range of disciplines. In this chapter we describe the process development of a number of NIL-based techniques for integrated photonics. To attain this goal, material properties, mold properties and surface chemistry are important issues and will be discussed in the following sections.

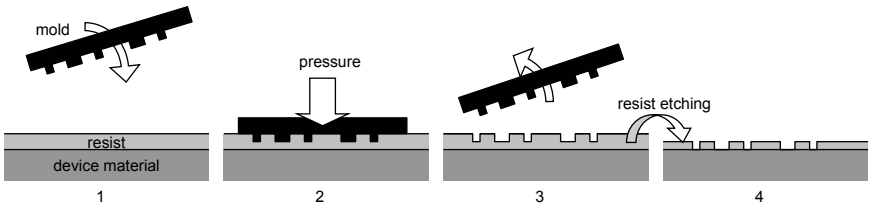

Figure 2.10: Principle of nanoimprint lithography (NIL): (1) alignment of mold and sample and application of a resist, (2) resist curing and (3) demolding.

2.3.2 Principles of nanoimprint lithography

Thermal NIL - also called hot embossing - utilizes a thermoplastic polymer layer for patterning. The mold is pressed into the polymer film while a heating cycle is started to elevate the temperature to typically 40^o to 90^o C above the glass transition temperature of the polymer. This allows the material to soften and to flow into the recessed areas of the mold. The assembly is subsequently cooled to harden the polymer structures. Finally, the mold is removed. The thermoplastics utilized for thermal NIL generally have high viscosities that require large pressures (20 to 70 bars) to fill the mold during the imprint step.

Ultraviolet-NIL (UV-NIL) utilizes a UV-curable liquid (resist) of low viscosity that can be imprinted at room temperature using UV light to initiate a polymerization and "lock" the molded structures into place. Unlike thermal NIL, UV-NIL requires either the mold or the substrate to be transparant for UV-light. In most cases, the substrate is opaque and a transparant mold is used. The low viscosity of UV-NIL resists allows imprint processes with low pressures. Therefore, the mechanical requirements of the imprint tool are relaxed considerably. Moreover, the use of a transparent mold offers advantages for precision alignment.

The principle of both approaches is fundamentally the same and a scheme is depicted in Fig. 2.11. In the following we assume parallel contact between the surfaces of the mold and the substrate and neglect surface tensions and capillary forces. The mold is assumed rectangular of dimensions SxL and contains a grating structure with protrusion lines of dimensions sxLxh_s, whereby $s \ll S$ and with h_s the height of the grating. The protrusion coverage is the ratio of elevated to recessed area on the mold A_p/A_r and is assumed uniform over the mold area. The initial thickness of the resist layer on top of the substrate is h_i. During imprint, the mold is pressed into the resist with a pressure p. Under these assumptions, the stationary Navier-Stokes equations indicate that the process of pressing together mold and substrate through a resist of viscosity μ goes through two different regimes characterized by a different sinking rate $u = \frac{dh(t)}{dt}$ as a function of time t:

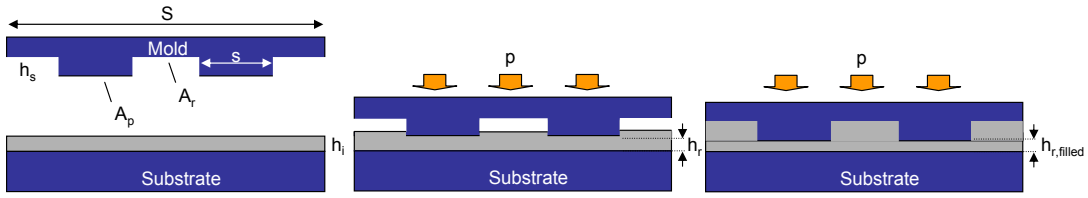

Figure 2.11: Schematic of the cross section of mold and substrate before and during imprint.

$$u = \begin{cases} \frac{ph(t)^3}{\mu s^2} & \text{for } t < t_{filled} \\ \frac{ph(t)^3}{\mu S^2} & \text{for } t > t_{filled}. \end{cases} \tag{2.1}$$

In both regimes, the residual layer at time t can be calculated from:

$$h_r(t) = \begin{cases} \sqrt{(\frac{1}{h_i^2} + \frac{2t}{\mu s^2}\frac{SL}{A_p}p)^{-1}} & \text{for } t < t_{filled} \\ h_i - \frac{1}{1+A_p/A_r}h_s = h_{r,filled} & \text{for } t = t_{filled} \\ \sqrt{(\frac{1}{h_{r,filled}^2} + \frac{2p(t-t_{filled})}{\mu S^2})^{-1}} & \text{for } t > t_{filled}, \end{cases} \tag{2.2}$$

The interpretation of these results is as follows: for $t < t_{filled}$ the mold protrusions sink into the resist layer and make the resist flow from under the protrusions towards the mold cavities. Thus, as long as these cavities are not yet completely filled, the sinking rate is determined by the size of the structures on the mold: the smaller they are, the faster it goes. At $t = t_{filled}$ the recessed areas are filled and the residual layer thickness can be calculated from simple geometric considerations given by the second part in Eq. 2.3.2. At this point, the situation changes drastically. From now on, the mold can only sink further when liquid is displaced over the entire mold width S, which is orders of magnitude bigger than s. As a result, the flow practically stops: it goes further, but at a very slow rate.

This explains why a residual layer will always remain after an imprint process. This residual layer should be removed by a so-called break-through etch in order to expose the substrate in the recessed areas when the final resist pattern is to be used as an etch mask for the underlying substrate or as a sacrificial layer for lift-off. For any imprint process making use of spin-coated resist layers, the second part of Eq. is a very good estimate for the final residual layer thicknes. This is the case for thermal NIL, where resists of very high viscosity are used (in the order of 50 to 5000 kPa.s at imprint temperature) as well as for UV-NIL, where liquids of much lower viscosity are used (in the order of 100 to 1000 mPa.s). However, for very low viscosities (in the order of 1 mPa.s to 100 mPa.s) spin coating leads to unstable films [56] and drop dispensing is often used. In that case, the initial thickness can still be estimated from the third part

of Eq. 2.3.2. Given that the initial layer thickness is much higher than the final residual layer thickness, the equation can be reduced to:

$$h_r(t) = \sqrt{\frac{S^2}{2pt}}\sqrt{\mu}. \tag{2.3}$$

The validity of these estimates has been experimentally verified in [57] and in [58]. As a numeric example, we find that an imprint time of 60 seconds suffices to reach a residual layer of about 100 nm when a mold of 1 cm^2 is pressed into a resist of viscosity 1 mPa.s (ie. viscosity of water at 20^{o}C) using a pressure of 1 bar.

The protrusion coverage is defined locally and is therefore not necessarily constant across the entire mold area. Since any mold is subject to a certain degree of bending, a varying protrusion coverage over the mold area results into a varying residual layer thickness [58] and/or partial filling of the mold cavities [53]. As a consequence, periodic structures where the protrusion coverage A_p/A_r is constant throughout the whole area to be printed are favorable. A_p/A_r can be considered constant on a somewhat larger scale if structures that are aperiodic in themselves are arranged in a periodic manner.

Control of the residual layer thickness and its uniformity over the imprinted area is of great importance for most applications, especially in semiconductor processes where the imprint of the resist is only an intermediate step in the entire fabrication process. A thick residual layer is desirable to support alignment, high throughput and low defects [54]. However, given that the entire imprinted pattern is etched during the break-through, a thin residual layer is advantageous because it requires a much shorter etching step than a thick residual layer and thus allows for better control of the critical dimensions of the imprinted pattern [55].

Important for obtaining uniform residual layers is a parallel alignment of mold and substrate and a uniform imprint pressure during the imprint cycle. As most bonding machines provide these requirements, imprint tools are often based on bonding machines in some cases extended with mold separation tooling. The high pressures during the imprint cycle allow conformal contact between the rigid substrate with spincoated or dispensed imprint layer and the rigid mold. The high pressures are needed to overcome thickness variations of the mold and/or substrate to ensure a uniform residual layer after imprint. The low viscosity of UV-NIL resists allows imprinting with much lower pressures. However, the pressure is generally too low to ensure parallel alignment and uniformly distributed pressure while the polymer is flowing between mold and substrate. This problem can be tackled by using a flexible mold. The mold cavities allow for sufficient polymer flow, while the mold flexibility allows for uniform distribution of the pressure and conformal con-

tact with the substrate once the resist has flown freely. Using this principle uniform residual layers can be obtained even without applying pressure [59].

Based on the principles of nanoimprint lithography described in this section we have developed a number of nanoimprint based techniques for chips and fiber facets. The results of the process development will be described further on.

2.3.3 Adhesion control and anti-adhesion treatment

Ideally, imprinted features will adhere selectively to the substrate and release completely from the mold after imprinting. In cases where the mold does not release cleanly from the imprinted material, defects are created on the substrate and the mold is contaminated. To minimize adhesion, molds are typically surface treated to improve its release properties. A common strategy is to modify the surface functionality by covalently bonding molecules with fluorinated tails to the surface. Fluorinated molecules, such as Teflon, have low surface energy, which is an ideal property to minimize adhesion.

The molds used in this work are made of silicon. For silicon surfaces or silicon oxide surfaces, a silylation reaction can be used to covalently bond fluorinated chlorosilane molecules (or fluorinated alkyloxysilanes) to the surface. Once treated, the mold can be used and reused several times with minimal adhesion. Anti-adhesion treatment can be done in a solvent, gas or in a plasma environment. We compared them by measurement of the static contact angle of water on the diffently treated surfaces.

The solvent treatment is carried out by the following procedure. A solution of 0.1 % trideca-fluoro-(1,1,2,2)-tetrahydrooctyltrichlorosilane ($C_8H_4Cl_3F_{13}Si$, ABCR GmbH) in pentane is prepared in a petri dish. Then, the mold is immersed and the petri dish is covered to avoid contamination and rapid evaporation of the volatile pentane. The trichlorosilane groups react with the surface hydroxyl groups under separation of HCl allowing the formation of an anti-adhesion layer [60]. The reaction is illustrated in Fig. 2.12 (a). Fig. 2.12 (b) are pictures of a water drop on top of a non-treated and a treated sample. The mold becomes highly hydrophobic as a result of the anti-adhesion treatment illustrating the low surface energy. The described anti-adhesion treatment lowers the adhesion to polymers as well as to other materials (see section 2.3.6.3).

The plasma treatment was performed using Mechanical Vapour Deposition (MVD - Applied Microstructures, Inc.) to deposit an anti-stiction coating of perfluorodecyltrichlorosilane (FDTS: $C_{10}H_4Cl_3F_{17}Si$). Table 2.1 shows the static contact angle measurements of solvent treated and plasma treated silicon. Also included is the root-mean square surface roughness of the corresponding samples, determined by atomic force microscopy (AFM). For comparison measurement data of bare cleaned crystalline silicon and gold are in-

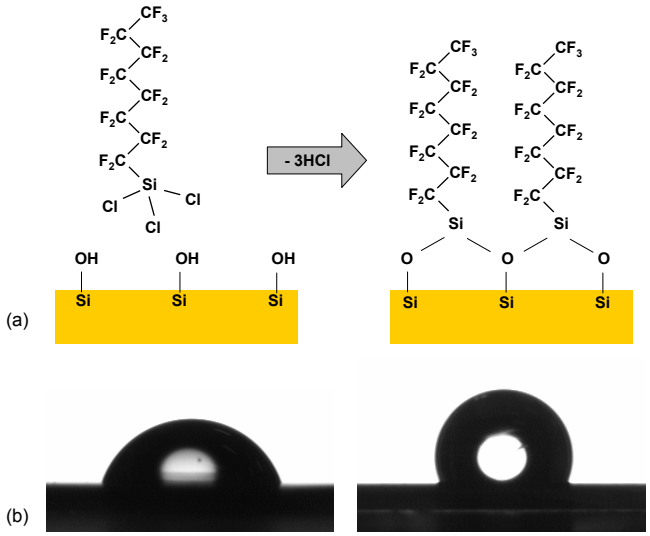

Figure 2.12: Anti-adhesion treatment of silicon or siliconoxide: (a) reaction of the silane. (b) Static contact angles before and after the treatment.

cluded in the table. We conclude that silicon becomes highly hydrophobic by anti-adhesion treatment and that the solvent treatment is preferred over the plasma treatment. Therefore, in the rest of this chapter we use solvent treatment unless otherwise stated.

Table 2.1: Static contact angle measurements and surface roughness data

Material	Contact angle	RMS surface roughness
silicon	65	0.121 nm
solvent treated silicon	110	0.173 nm
plasma treated silicon	92	0.272 nm
gold	85	0.796 nm

For treating molds made of different materials such as metals, polymers or semiconductors other than silicon, surface modification is possible using alternative dedicated molecules. However, given the very good results with silicon silanization, we treated such molds by chemical vapor deposition of a thin silicon oxide layer and subsequent silanisation as described above.

2.3.4 Imprint tools

For thermal nanoimprint lithography, the most straightforward approach is to make use of a wafer bonding machine. Bonding of two wafers requires parallel substrate-to-substrate alignment as well as pressure and temperature control. The requirements for performing thermal nanoimprint are the same

as for wafer bonding with the understanding that the substrate needs to be removed from the mold after the pressure- and temperature cycle, whereas in bonding the two substrates are permanently and intimately glued together during the process. Imprinting of nanophotonic structures using an EVG 520 HE wafer bonder with PMMA spincoated onto the substrate as the imprint resist will be described further.

For applications requiring only moderate pressures (a few bar) in combination with a thermal treatment, we made use of an in-house made vacuum bonding setup [61]. In this bonding tool the mold is attached to a flexible silicone membrane while the substrate is hold on a heated chuck. By evacuating the bonding chamber the flexible silicone membrane deforms and mold and sample are contacted in a low vacuum environment using a uniform pressure of 1 bar. When a higher pressure is wanted, excess nitrogen can be pured in the nitrogen pressure chamber.

UV-based nanoimprint lithography requires the use of unconventional nanoimprinting tools (e.g. IMPRIO by Molecular Imprints, Austin, TX). These machines are dedicated towards UV-based nanoimprint and allow for tight control of process variables for reproducible pattern generation including the ability to obtain a uniform residual layer of predetermined thickness. However, such dedicated tools are typically unavailable in most cleanrooms and require costly imprinting templates and ad hoc drop dispensers to support different UV-curable materials. A very interesting alternative approach is to work with the much cheaper flexible PDMS molds. However, imprinting using PDMS molds also requires specialised tools (e.g. EVG 620). In our work, we worked on the developement of a nanoimprinting method using a conventional mask aligner as the imprint tool.

The MA-6 mask aligner (Suss MicroTec) accepts 5 inch masks and substrates of sizes ranging from 1 square cm to 6 inch wafers. It contains alignment control equipment and a mercury lamp with optical accessories enabling UV exposure at different wavelength channels. For our applications, we used an intensity set-point of 5 W/cm^2 at a wavelength of 320 nm. When the aligner is used for optical lithography, a quartz-chrome mask is attached to the mask holder by suction with the mask oriented such that the chromium pattern is at the bottom. Likewise, the substrate is attached to the chuck on the motorized stage. When used as a tool for UV-based nanoimprint, the mask holder is used to hold either the transparant substrate or the transparant mold. Likewise, the chuck is used to hold the non-transparant mold (e.g. made of silicon) or the substrate respectively. In either case, the UV radiation passes through the upper sample to cure the resist between mold and substrate. We note that a wedge-error compensation (WEC) function is built into the mask aligner system. With this function mold and substrate are positioned almost perfectly parallel prior to alignment.

The machine can be operated in different modes. For our applications, we used the proximity mode and the vacuum contact mode. A scheme of both modes is depicted in Fig. 2.13. In proximity mode, the chuck vacuum holds the substrate during exposure and a pre-set separation gap is maintained between the mask and the substrate during exposure. This is used for pressureless imprinting without contact between mold and substrate. In this case, the residual layer thickness is equal to the preset separation gap (with an accuracy of $\pm 1\mu$m. In vacuum contact mode a vacuum is drawn between the mask and the substrate to bring the wafer in very tight contact with the mask prior to UV exposure. This vacuum is temporarily formed using a rubber ring to seal it off. This mode is used for imprinting with a low pressure. However, we note that the pressure in the MA-6 mask aligner is not uniformly distributed and that bowing of mold and substrate typically occurs. For conventional thicknesses of mask and substrate, the bowing can be up to $\pm 6\mu m$ over a 4 inch wafer. This is less when using thicker and more rigid mask and wafer material. For this reason, the MA-6 mask aligner is not suited when thin and uniform residual layers are desired. This is the main drawback of using a conventional mask-aligner for nanoimprinting purposes. To obtain a uniform pressure, the MA-6 mask aligner can be upgraded with a nanoimprint module in the form of an adapted mask and wafer holder which can be inserted into the aligner [62]. This module allows for vacuum contact while both wafer substrate and mold substrate are slightly bent using excess nitrogen purged into the holder chambers. In this way uniform residual layers can be obtained. In this work, we had access to an MA-6 mask aligner. We used it without an imprint module so that it is only suitable for those applications where the residual layer thickness is not criticial or where a thick residual layer is desirable.

A major advantage of using a conventional mask-aligner as imprint machine is the capability of combining nanoimprint with high precision alignment. The MA-6 mask aligner hardware includes manual x,y-micromechanical stage control, motorized z-stage control, WEC procedure for parallel alignment, rotational control and microscope tooling along with the necessary software and offers 600 nm alignment accuracy for optical contact lithography. Imprinting of micro- and nanophotonic structures and components using the MA-6 mask aligner will be described further.

Imprinting on fiber facets was developed as an in-situ technique. This means that the imprinting is done directly on the measurement setup where the fiber component is used, requiring no specialized imprint equipment.

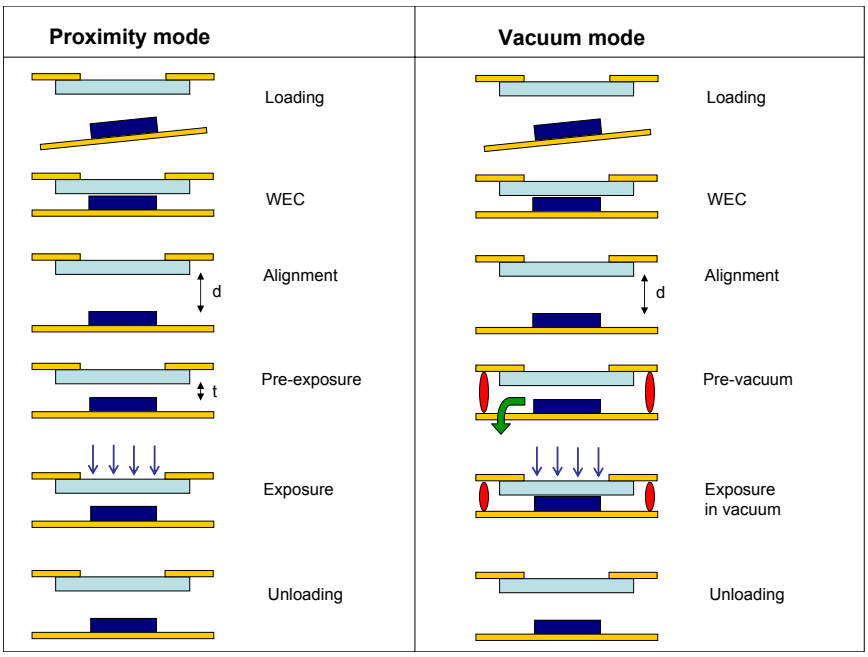

Figure 2.13: MA-6 Mask Aligner user modes: proximity mode for pressure-less imprinting of thick polymer layers and vacuum mode for low pressure imprinting of thin polymer layers. d = alignment gap, t = exposure gap

2.3.5 Polymers

Polymers used for nanoimprint lithogrpahy must meet a number of material requirements, which strongly depend on the application. In this section we give an overview of the polymers used in this work.

2.3.5.1 PAK-01

PAK-01 is a commercially available UV-NIL resist (Toyo Gosei Co.). PAK-01 is composed of tri(propylene glycol) diacrylate, 2,2-dimethoxy-2-phenylacetophenon as a photoinitiator, and several additives [63]. Its viscosity is 75 mPa.s which can be lowered by dilution using isopropoxyethanol (IPE) [64], [65]. The UV-exposure dose needed to crosslink the prepolymer mixture is 2000 mJ/cm^2. Uncured PAK-01 dissolves in solvents like ethanol and isopropylalcohol (IPA). After curing, it is mechanically very stable over a large range of temperatures, has a Youngś modulus of 0.23 GPa [66] and is optically transparant. Its refractive index at a wavelength of 1545 nm is 1.57 at room temperature.

We used an MA-6 Suss Mask Aligner for evaluating PAK-01 as imprint resist. An SOI mold containing periodic arrays of hexagonal holes with different periods and hole diameters and non-periodic isolated features was anti-

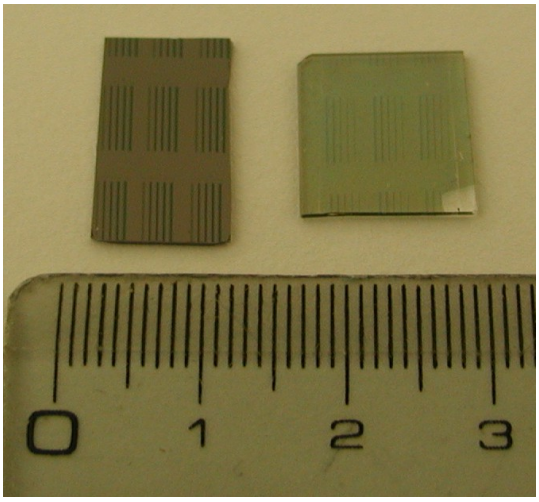

Figure 2.14: Images of the silicon mold and the imprinted PAK-01 sample.

adhesion treated and loaded in the mask aligner. A flat glass plate was installed on the mask holder. We increased the separation gap and dispensed a drop of PAK-01 in the center of the mold using a pipette. Subsequently, the exposure sequence was started. This means that substrate and mold are brought into contact while the liquid drop is flowing and spreading out radially. Exposure starts as soon as the vacuum has built up in the rubber sealed vacuum chamber. After exposure the mold sticks firmly to the substrate and demolding is done manually using a scalpel. Figure 2.14 and Fig. 2.15 show the result.

Periodic as well as isolated features of micro- as well as submicron size structures are well replicated. The residual layer thickness of the imprint is non-uniform. This is no surprise as the overall bowing of the mold, mask holder, chuck, and substrate is estimated to be 1.5 μm for a 1 inch diameter chip.

PAK-01 can be imprinted and used as an etch mask for further processing. However, we did not use it for that purpose. Given its interesting optical and mechanical properties, we used it for the fabrication of optical devices including wedged diffractive elements for SOI grating couplers, wedged diffractive element on fiber facets, UV-transparant molds and as intermediate polymer material for optical fiber probes. We will come back to all of these applications in this and the following chapter.

2.3.5.2 J-Resist

J-Resist is a mixed product of 67 m% benzylmethacrylate monomer (Aldrich), 20 m% polydimethylsiloxane (Aldrich) as a diluent and 3 m% Irgacure 184 (Ciba) as a photo-initiator. 10 m% 3-acryloxypropyl-tri-methylsiloxisilane (Gelest)

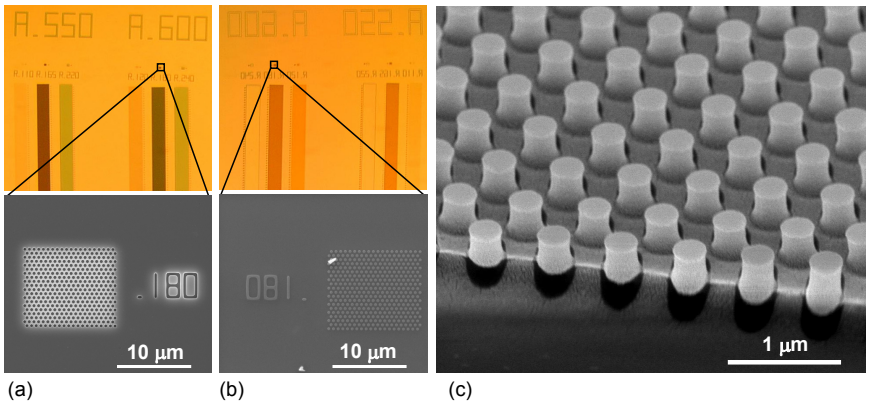

Figure 2.15: Details of the mold and imprinted sample of Fig. 2.14. (a) 1 mm^2 and detail of the mold and (b) 1 mm^2 and detail of the imprint. (c) Cross-section image of the imprint.

is added to lower the surface energy and improve mold detachement. No cross linker molecule was added. This mixture, originally developed by Jung and coworkers for UV-nanoimprint with ultrathin residual layers [67] will be further referred to as J-resist. The viscosity of J-resist is very low in the order of 1 mPa.s (which is the viscosity of water at room temperature). The exposure dose needed for forming a rigid structure by polymerization is 6000 mJ/cm^2. Cured J-resist is easily dissolved in acetone and does not withstand high temperatures. J-resist was originally developed to serve as a sacrificial layer for metal lift-off, which is also the application we used it for.

We evaluated the imprint properties of J-resist according to the procedure described above. Due to the low viscosity of J-resist, it can flow easily during imprinting and leaves very low and rather uniform residual layers. The residual layer can be etched away using a short plasma etch. In this work, J-resist was used for fabricating sub-micron period metal gratings on silicon, according to a double imprint procedure using PAK-01 based molds, as will be explained further.

2.3.5.3 SU-8

SU-8 is a negative high contrast, epoxy based photoresist [78]. Depending on the concentration of the active components, a wide range of film thicknesses can be obtained, ranging from below 1 μm to over 200 μm with a single coating process. The exposed and subsequently cross-linked portions of the film are rendered insoluble to liquid developers. SU-8 is chemically stable and withstands heavy acids such as HF. SU-8 typically has very high optical transparency above 360 nm and in the near infrared, but is not suited as waveguide material in the spectral window around 1550 nm.

In this work we worked with Nano^{TM} SU-8 10 of viscosity 1050 cSt (or 1300 mPa.s, assuming a density of 1.237 g/ml) [79]. We used it for the fabrication of wedged optical elements on grating couplers. Another typical use of SU-8 is for fabricating master templates for the structuring of PDMS for a variety of applications.

2.3.5.4 PDMS

Poly(dimethyl siloxane) (PDMS) is a linear polymer consisting of a backbone chain of Si-O units and two methyl side groups connected to the Si atom. Its chemical formula is included in Fig. 2.16. PDMS is very inert, so reactive functionalities must substitute for the methyl groups at the ends or along the chain in order to form curable polymer blends. Two-component PDMS (Dow Corning, Sylgard 184) is the most well-known of the PDMS family. It has a low surface energy (2224 dyn/cm), high optical transparency (85%) in the wavelength range between 340 and 600 nm and flexible. Its mechanical properties can be engineered to some extent through blending of different functional siloxanes, adding additives and/or adjusting processing parameters such as curing cycles.

PDMS Sylgard 184 has been proven favourable for Soft UV-NIL [68] with high resolution. Flexible PDMS molds are made using a cast-molding process, which typically contains the following steps: (1) mixing (10:1 base/curing agent), (2) pooring the PDMS over the silicon master, (3) curing (35 min on a hot plate at 130^o C) and (4) detachment from the master by peeling. Its viscosity is 3900 mPa.s and its Youngś modulus after curing is 3 MPa.

After detachment from the master, the backside of the formed elastomeric stamp can be treated with an oxygen plasma for 30 s in order to increase their surface energy, thus changing their hydrophobic character to a temporary hydrophilic state. The backside of the stamp can then bonded be to a glass-substrate to be used as a rigid stamp carrier for imprinting. A similar process can also be used for the fabrication of microfluidic chips and is also commonly used for the fabrication of flexible molds for UV-based nanoimprint.

2.3.5.5 PMMA

Poly(methyl methacrylate) (PMMA) is the most thoroughly studied thermal NIL material. Its chemical formula is included in Fig. 2.16. PMMA has a glass transition temperature of 95-105 C, which is well above room temperature. PMMA can be coated out of a number of common solvents such as chlorobenzene and propylene glycol methyl ether acetate. During imprinting, the film is heated to facilitate flow of the polymer. Once imprinted and cooled, the resulting structures are mechanically stable. In this work, PMMA was used as

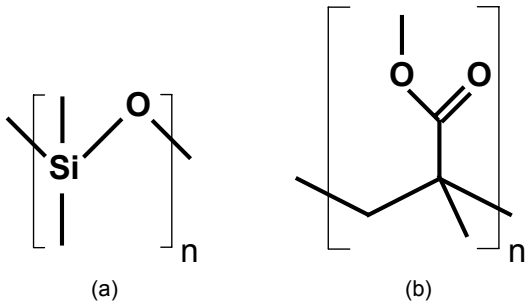

Figure 2.16: Chemical structures of (a) PDMS and (b) PMMA.

an imprint material and etch mask for fabricating SOI nanophotonic circuits, as will be explained.

2.3.6 Process development

We developed a number of nanoimprint processes, mostly based on UV-curing, which are easy-to-implement in a laboratory environment and do not require dedicated nano-imprint tools. These techniques allow for fabricating sub-micron features over large areas with high quality. Moreover, they offer a flexible choice of materials and of substrate sizes and shapes, which make them useful for a variety of applications.

Most of the processes developed in this work start from an 8 inch SOI wafer of which the top 220 nm silicon layer is patterned by DUV lithography and ICP etching. This is the master wafer. Chip-size pieces are cut out of the master wafer and serve as a mold for nanoimprint, nanoprint or nanoimprint-and-transfer. The master chip needs a number of preparation steps to be carried out in a clean room environment before it can be used as a mold. The first step is always an anti-adhesion treatment as described before. The next steps depend on the specific application.

2.3.6.1 Double UV-based nanoimprint for defining metal nanostructures

UV-NIL requires either the substrate or the mold to be transparant. So, for defining nano- and microstructures on an opaque material such as silicon, the mold has to be transparant. The fabrication of a transparant mold is typically done by etching into quartz starting from a resist pattern defined by a direct-write technology. Indeed, other fabrication technologies such as DUV lithography are not accessible for materials other than silicon wafers. So even for structures with limited resolution requirements, the fabrication of a transparant mold has to rely on time-consuming direct write technologies such as e-beam lithography. For that reason, custom-made transparant molds are very

expensive to fabricate. Moreover, the technology for quartz etching is not as mature and standard as for silicon etching. Access to high-resolution quartz etching systems is thus rather limited.

A non-expensive alternative for quartz molds are soft PDMS molds, fabricated by cast-molding. The main advantage of a PDMS mold is its flexibility, allowing for conformal contact between mold and substrate, even for a non-planar surface. Moreover, it is highly UV transparant and has a low surface energy which makes an anti-adhesion treatment unnecessary in most cases. Soft UV-NIL has been developed using flexible PDMS molds to enable the low pressure imprint of whole wafers in a single step [68]. With this technique microring resonator fabrication in SOI has been demonstrated [69].

A typical approach to fabricate high resolution metal nanopatterns on opaque substrates is nanoimprint followed by a lift-off process. However, this is not as straightforward as it seems. A lift-off step is only successful when the process allows for control of the sidewall angle of the patterned resist. In standard microelectronics processing, resist schemes have been developed that allow for the definition of sacrificial resist patterns with negatively sloped angles to allow for a good lift-off. However, defining such a resist pattern with a nanoimprint process seems unfeasible. Thus, the best compromise is to fabricate resist patterns with a straigth angle. However, in a typical nanoimprint process, the imprint step is only the first step of the process. Then follows a residual layer etch which typically has a detriminal effect on the critical dimensions of the resist making the resulting resist pattern unsuitable for lift-off applications due to rounding of the original pattern. The rounding can be avoided by optimizing the imprint process in such a way that very thin residual layers are obtained. As a consequence, residual layer etching times can be very short and the rounding effect will be minimal. Such a combined UV-NIL and lift-off process was developed for the fabrication of very high resolution cross-line patterns by utilizing J-resist with an extremely low viscosity resulting in nearly no residual layer thickness even with a low pressure [67]. However, the process makes use of a rigid quartz mold and thus does not offer the advantages of working with a soft mold.

In a recent publication, the fabrication of gold patterns using a soft PDMS mold was reported. However, this technique is a printing technique whereby the gold patterns are transferred from the PDMS mold protrusions onto the substrate [70]. The demonstrated resolution is rather moderate (none of the features is smaller than 1 μm) and the surface roughness is very high. The reason for the moderate resolution is the intrinsically high viscosity of PDMS molds causing partial filling of the master cavities during mold fabrication and irregularities in the mold protrusion height. The reason for the high surface roughness is the rounding of corners of the mold protrusions. Both are typical drawbacks of PDMS molds and are the main reasons why the fabrica-

tion of metal nanostructures by soft UV-NIL followed by lift-off has not yet been addressed in the literature.

We developed a nanoimprint and lift-off process for defining micron- and submicron scale gold patterns on silicon using a soft PAK-01 mold as the mold. Such a mold is much less flexible than a PDMS mold, but offers very good filling properties. The process flow is shown in Fig. 2.17. First, the DUV-fabricated silicon master is loaded on the vacuum chuck of the mask aligner and a quartz plate is loaded on the mask holder. The aligner is used in proximity mode with the following settings:

Imprint pressure	Al. gap	Exp. gap	Total imprint time	Exposure time
0	10 μm	4 μm	720 s	120 s

A drop of PAK-01 is applied onto the silicon master prior to loading. A setting of 10 μm as alignment gap is rather low, but is chosen in order to preserve the drop shape so that trapping of air after the WEC-procedure is avoided. The imprint starts when pressing the "Exposure" button. Master and quartz plate are brought to a distance of 4 μm. During the first 600 seconds of the exposure, the light from the UV lamp is blocked to allow for sufficient polymer flow prior to the actual exposure step. After exposure, demolding takes place automatically as the z-stage moves down while the mold is tightly hold on the vacuum chuck by suction. When too much polymer is applied, the master sticks to the glass substrate and has to be demolded manually using a scalpel. We note that manual demolding may deteriorate the imprinted structures due to torsional forces. Although this effect has been observed with thermal imprint lithography using PMMA (see Fig. 2.18) and high imprint pressures, such an effect has not (yet) been identiefied in the literature for UV-NIL techniques using low imprint pressures.

Although mechanical more rigid than a PDMS mold, the surface energy of the PAK-01 mold is too high for using directly as an imprint mold. Demolding would damage the imprint. Therefore, a thin layer (30 nm) of silicon oxide is deposited onto the PAK-01 mold by plasma-enhanced chemical vapor deposition, followed by an anti-adhesion treatment. The mold is now ready for further usage.

Nano-imprint followed by lift-off allows the fabrication of sub-micron metal structures. A PAK-01 mold was fabricated on a 15 cm x 15 cm glass substrate according to the method described above. A silicon substrate was cleaned and any organic contaminants were removed by a piranha solution (a mixture of 3:1 concentrated H_2SO_4 and 40 % H_2O_2 solution) prior to imprinting. A drop of J-resist was dispensed on the silicon substrate and loaded in the MA-6 mask aligner. The vacuum mode was used and exposure time was set to 15 minutes. After imprint and unloading, a break through etch was performed by reactive ion etching (RIE) using O_2 and CF_4, 50 and 5 sccm respectively at a power of 50

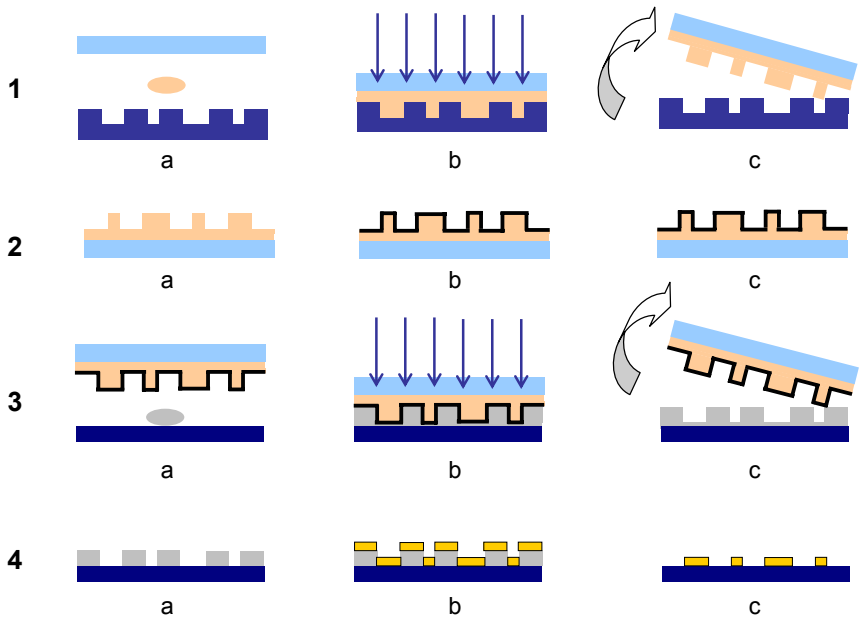

Figure 2.17: Double UV-based nanoimprint process flow for defining metal nanostructures: (1) PAK-01 mold fabrication from DUV-fabricated silicon master, (2) mold anti-adhesion treatment, (3) UV-NIL of very low viscous J-resist, (4) metal lift-off.

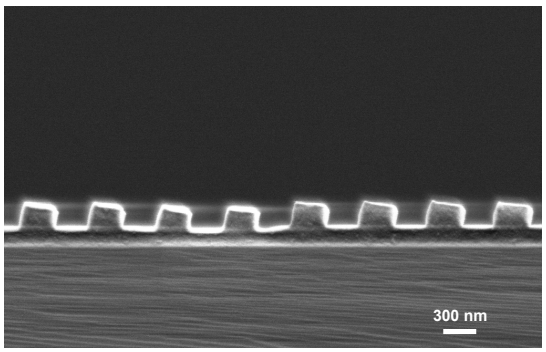

Figure 2.18: Effect of torsional forces on imprinted grating structures caused by manual de-molding after thermal imprint in PMMA.

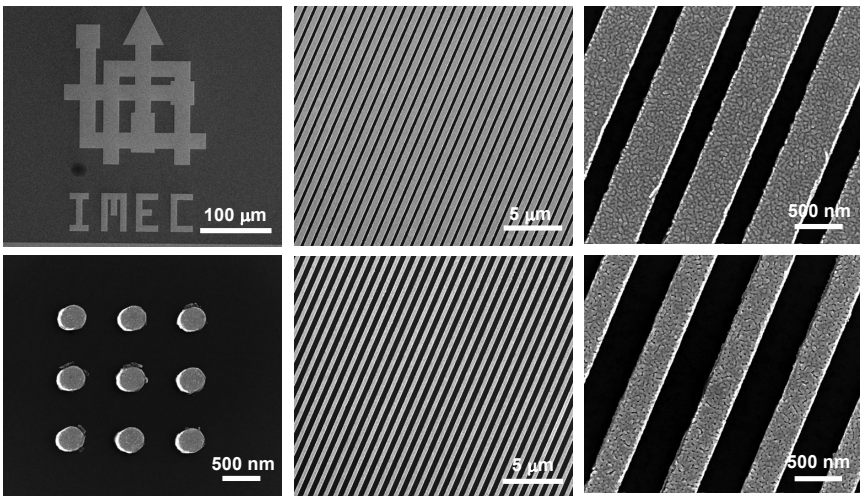

Figure 2.19: Fabricated gold micro- and nanopatterns on a silicon chip by UV-nanoimprint using a transparant PAK mold in J-resist, followed by gold lift-off. (a) Isolated structures, (b) large area gratings with varying filling factor, (c) detail of the gratings. All structures are imprinted in the same step.

W. Etching time was set to 10 seconds. Next, 3 nm of titanium was sputtered and 30 nm of gold evaporated onto the sample using a Univex system. Lift-off was performed in acetone in an ultrasonic bath.

The results are shown in 2.19, representing three areas on the same sample, illustrating that large micron sized as well as submicron sized structures are imprinted in the same step.

2.3.6.2 Nano-print

Nano print lithography (NPL) was developed as an intermediate step for nanoimprint and transfer lithography (section 2.3.6.3). We start with a 2 cm x 2 cm SOI mold with 220 nm top silicon layer containing various structures and treated with an anti-stiction coating. 20 nm of gold is evaporated onto the mold by Joule evaporation. The substrate on which the structures need to be printed is prepared in the following way. A 200 nm layer of BCB (Benzo-CycloButene, Cyclotene 3022-35, Dow Chemicals) is spin coated on a silicon sample. Both are brought in intimate contact using the bonding tool. During contact a pressure of 1 bar was applied and the substrates were heated to a temperature of 150^o C for good adhesion between the BCB and the gold on the mold protrusions. The ensemble is allowed to cool down and the mold is released from the substrate. As a result the gold on top of the mold protrusions is transferred to the BCB layer, as can be seen on Fig. 2.21 (a) and (b). Large areas of the metal as well as thin sub-micron features are successfully trans-

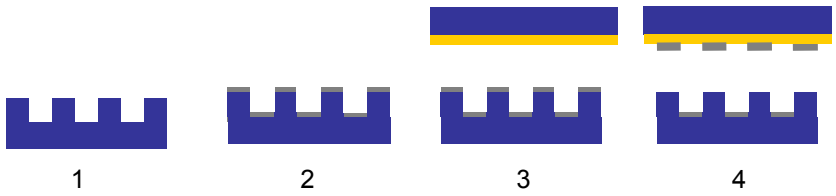

Figure 2.20: Nano-print lithography process flow: (1) Mold anti-adhesion treatment, (2) gold evaporation, (3) preparation of the bonding step: spin-coating of BCB-layer, (4) bonding.

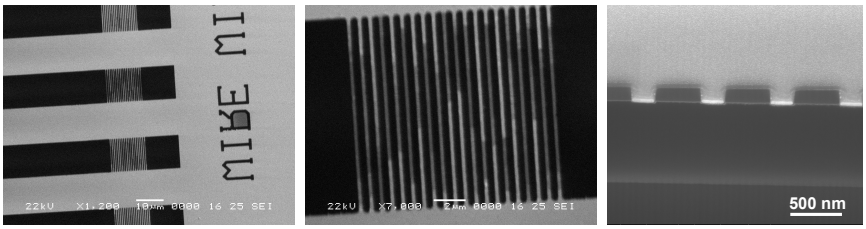

Figure 2.21: Nano-print lithography: (a), (b) transferred gold gratings on a BCB-covered silicon chip, (c) cross section of the mold after the transfer process: gold on top of the grating lines is removed while the gold in the trenches remains.

ferred. The cross-section picture of Fig. 2.21 (c) was taken after removal of the sticky substrate: it shows that the gold on top of the grating lines was successfully removed while the gold in the trenches remained. The original mold has become a carrier of a metal pattern in the mold trenches. Such a mold can be used for nano imprint and transfer lithography.

2.3.6.3 UV-based nanoimprint-and-transfer

Nano-print is an interesting technique to define sub-micron patterns. However, the technique can only be applied when the sticky intermediate layer is spin coated on the substrate. Moreover, it requires a thermal cycle and application of pressure to ensure conformal contact between substrate and mold. UV-based nano imprint and transfer lithography (UV-NITL) was developed to maintain the sub-micron patterning capability while allowing for more flexibility in the choice of substrates. UV-NITL is a combination of UV-NIL and NPL and utilizes a low viscous UV-curable liquid as the intermediate layer between the transferred pattern and the substrate without the need for spin coating. This technique allows the patterning of wedged and curved shapes too and small fiber facets.

UV-NITL starts with a mold carrying the desired metal pattern in the mold trenches. A drop of PAK-01 is dispensed onto the mold and squeezed between

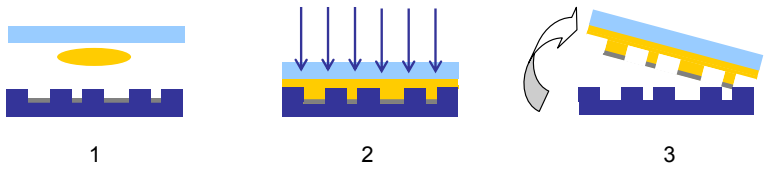

Figure 2.22: UV-nanoimprint-and-transfer (UV-NITL): (1) drop dispensing on the prepared mold, (2) imprint and UV-curing, (3) demolding.

the mold and a UV-transparant substrate. The polymer fills the cavities in the mold and is locked into place by the UV-exposure. Upon demolding the metal sticks to the polymer and is transferred from the mold to the substrate. A schematic is depicted in Fig. 2.22.

A mold for UV-NITL can be prepared in different ways. A first approach is to coat the mold with gold and transfer the gold on the mold protrusions to another substrate by nano print lithography according to the procedure described in the previous section. Due to the printing, the metal on the mold protrusions is removed while the metal in the mold trenches is left behind. A second approach is to coat the mold with gold and remove the gold on the mold protrusions manually using scotch tape. Fig. 2.23 shows a microscopic image of such a mold sample. The border line between the sample area where gold was removed by the sticky tape and the rest of the sample is clearly visible. Both approaches are applicable on a chip scale as well as on a wafer scale.

The coating of the mold with metal is a critical step in the mold preparation. When the mold sidewalls are vertical, controlled directional evaporation of the metal is necessary in order to prevent the sidewalls from coating. When the sidewalls are not vertical, seeds of gold can be formed on the sidewalls of the mold. When such a mold is used for UV-NITL, the gold on the sidewalls gets also transferred which may be unwanted. To avoid metal on the sidewalls, a number of extra steps can be added to the DUV-lithography process to fabricate the original master wafer. In this process, the master SOI wafer goes twice through the lithography process: a first time to define the features in the silicon top layer and a second time to define a resist layer over the silicon features to serve as a protection layer. The exposure dose is chosen such that the resist protection layer is slightly bigger than the fabricated silicon features. In this way the sidewalls of the features are protected during metal evaporation. The mold with metal in the trenches and no metal on the mold protrusions and sidewalls is ready after dissolving the resist in acetone.

Adhesion between silicon and gold is very low. However, the anti-adhesion treatment is necessary for the transfer of gold to take place. Two molds were prepared using the resist overlayer approach. The first mold was prepared by anti-adhesion treatment followed by gold evaporation and resist removal. The second mold was prepared by gold evaporation, resist removal and anti-

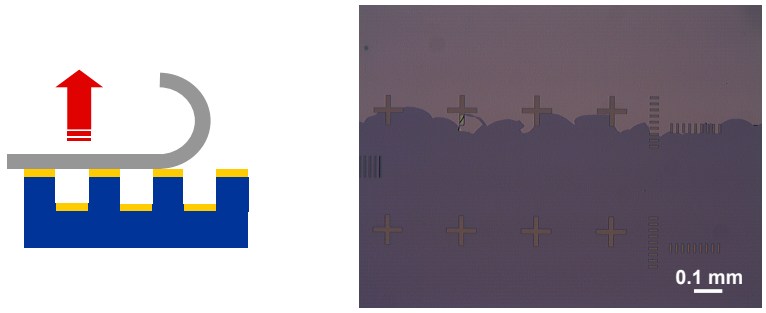

Figure 2.23: UV-NITL mold preparation scheme using scotch tape: (a) principle and (b) picture of the mold after preparation. The dark region is where the gold layer on top of the mold features is removed by the scotch tape.

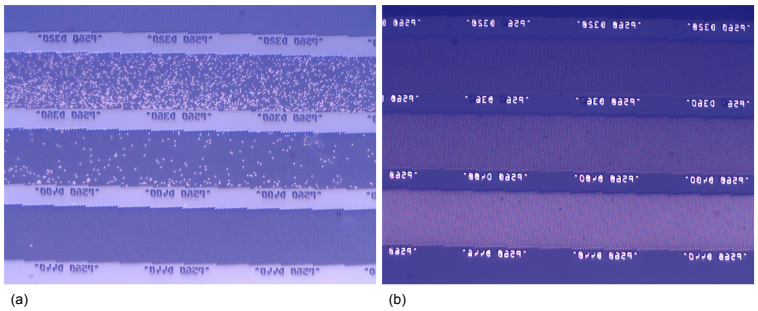

Figure 2.24: UV-NITL onto chips using a mold (a) without anti-adhesion treatment and (b) with anti-adhesion treatment. The transfer of gold is only successful for the anti-adhesion treated mold.

adhesion treatment as a final step. In this way, the difference between the two molds is in the silicon-gold interface: the first mold contains an anti-adhesion layer between gold and silicon whereas the second mold does not. The result of UV-NITL by the different molds is shown in Fig. 2.24 (a) and (b) respectively.

UV-NITL is a highly advantageous technique for high resolution patterning of fiber facets, as will be described in the next section.

2.3.6.4 Alignment & 3D-imprint

An important aspect in preserving and enhancing the functionality of photonic chips is the packaging of chips. Photonic devices of the future will consist of a photonic integrated circuit layer with highly miniaturized and complex functions and a functional polymer layer on top of that layer with interfacing functions to the environment. Interface components can include lenses, facets, mirrors, etc. to direct and redirect the light for coupling into or out of the

circuit, but can also include waveguide structures for interfacing with optical fibers. Another set of interface components can include channels, reservoirs and mixing elements for bio/chemical fluids for sensing applications. The fabrication of such a functional polymer layer requires a technology platform that allows for high resolution patterning combined with accurate alignment capability. Excimer laser ablation is the only technology truly capable of providing that combination. But as we mentioned before, excimer laser ablation is only suitable for prototyping.

Although the potential of nano imprint lithography for fabrication of three-dimensional components is highly recognized, there are only few reports of imprinting 3-dimenstional functional devices. The reason is probably the lack of being able to combine both 3D-patterning and alignment. In this section we implement 3D imprinting of polymers using a FIB-fabricated 3D mold on an SOI photonic chip with high alignment accuracy.

Mold preparation is carried out in three steps. First a 10 cm x 10 cm glass plate (Schott D263T, thickness: 1 mm) is prepared by optical contact lithography and lift-off. This mold consists of transparant and non-transparant parts. The transparant parts are 12 x 12 μm^2 and alignment markers on an otherwise non-transparant mold. The mold is made non-transparant by deposition of a 150 nm titanium layer. Second, the transparant parts are modified with FIB milling to define the 3D structures. In the third step, the mold is treated with an anti-adhesion layer by deposition of a thin silicon oxide layer followed by silanization. The mold is then loaded on the mask holder of the mask aligner. A schematic of the mold preparation is found in Fig. 2.25.

The substrate is an SOI photonic chip and is loaded on the vacuum chuck. Small drops of PAK-01 are dispensed where necessary and the process is started. The vacuum mode of the MA-6 mask aligner is best suited to ensure a minimal residual layer between the 3D component and the photonic circuit on the chip.

While mold and substrate are aligned using the alignment markers as a reference, the polymer can freely flow between the two. Prior to exposure, the distance between mold and substrate is decreased in steps of a few micrometers. After each step alignment is adjusted when necessary, until contact is obtained. Then, the imprint is started with exposure during the last cycle. The UV-light cures the PAK-01 under the transparant parts of the mold while the liquid under the non-transparant titanium is left uncured. When the imprint is ready, demolding takes place automatically and the chip is unloaded. The uncured PAK-01 is removed by IPA.

Fig. 2.26 shows an early result of fabricating wedges for redirecting light on top of SOI grating couplers. It is clear that adhesion of the small wedged areas to the chip is not straightforward. Changes to the mold design were necessary to overcome this problem. Good results were obtained by expanding the transparant area surrounding the transparant squares so that a larger contact area

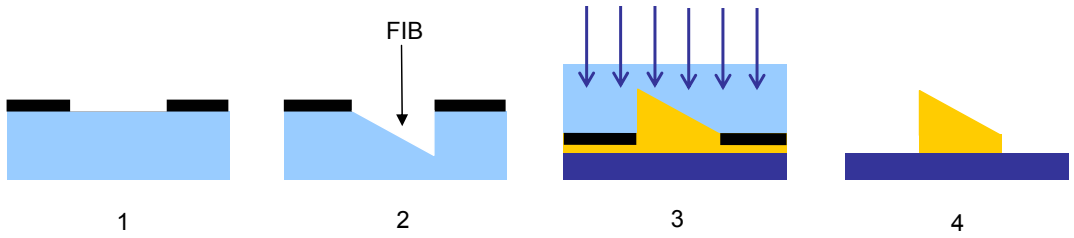

Figure 2.25: 3D imprint: (1) Mold preparation by optical lithography and lift off of a non-transparant layer, (2) wedge fabrication by FIB milling, (3) imprint and UV-curing, (4) demolding and removal of the uncured polymer.

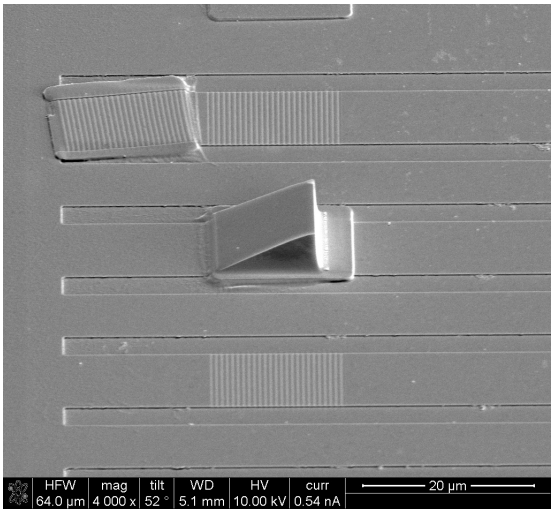

Figure 2.26: Fabricated polymer wedges on top of grating couplers: (from top to bottom) bad adhesion, good adhesion, no adhesion of the wedge to the chip.

is formed between the polymer and the chip ensuring good adhesion. Results on the optical performance of these structures are presented in section 5.4.2.

UV-based imprinting using a conventional mask-aligner with a FIB-fabricated mold is a very powerful technique. We focused on a chip-scale process, but a wafer-scale approach is within reach. A practical solution to perform UV-molding using a 3D FIB-fabricated mold on 8 inch wafers is by using a step-and-repeat process with a small die-size stamp. The small stamp can be fabricated by FIB and used as the mold. This mold is then mounted into the stepper, aligned with respect to the wafer features and pressed into the liquid imprint resist prior to UV-curing. This process is repeated for all dies on the wafer. There exists a number of tools on the market to perform this process. As an example the IMPRIO 55 (Molecular Imprints) should allow for a throughput of one 8 inch wafer per hour. An alternative solution is to work with a wafer-scale imprint process using a large mask of a size equal to the

substrate wafer. Those imprint machines allow for a much higher throughput (30-90 wafers per hour, Obducat HVM NIL), but the FIB-milling of such a big mold is much more expensive.

2.3.6.5 Photonic circuit fabrication

Within the framework of ePIXnet's NIL joint research activity, thermal nano imprint lithography for the fabrication of SOI nanophotonic components has been demonstrated in collaboration with MIC-DTU (Technical University of Denmark). The fabrication of SOI-based nanophotonic devices is done using thermal NIL using a 5 x 5 cm stamp containing the desired pattern cut out of an 8 inch SOI master wafer. The mold is modified by optical contact lithography and RIE etching to obtain a 50/50 wafer-scale protrusion coverage. This is necessary to allow for sufficient polymer flow during the imprint process so as to avoid too long imprint times for obtaining a thin residual layer.

The nanophotonic devices are fabricated in a 5 x 5 cm SOI substrate cut out from an 8 inch SOI wafer purchased from SOITEC with the following layer stack: 220 nm top silicon layer and a 2 m buried oxide. A 190 nm thin 50k PMMA film is spin coated onto the SOI substrate and mold and substrate are loaded into an EVG 520HE, which is a 4 inch wafer parallel plate bonding tool. Given that both mold and substrate are square wafers whereas the machine only accepts standard circular 4 inch wafers, dummy wafer material of the same thickness as the SOI mold and substrate is used to fill the empty space in the setup and stabilize the imprint setup. The following optimized imprint parameters are used:

Imprint pressure	Imprint temperature	Imprint time
13 bar	190^{o}C	1 h

This nanoimprint process results in a good filling of the mold features. Demolding is done manually using a scalpel. The nanoimprinted patterns are then transferred into the top silicon layer of the SOI by an optimized SF6-based RIE etching process. Fig. 2.27 depicts an image of an imprinted mach-zehnder interferometer, optically characterized in a horizontal setup with cleaved facets for input and output.

To facilitate characterization of nanoimprinted photonic structures, grating couplers are very suitable, as we will see in chapter 3. The fabrication of grating couplers using thermal nanoimprint lithography is not straightforward as it requires a two-level etching process. We have implemented this process by a double-step imprinting process. First, an SOI photonic chip is fabricated by thermal imprint, according to the parameters above. Next, a silicon mold with 630 nm period gratings is fabricated by e-beam lithography, aluminum deposition, lift-off and RIE etching. The feature height of the mold is 280 nm. A 500

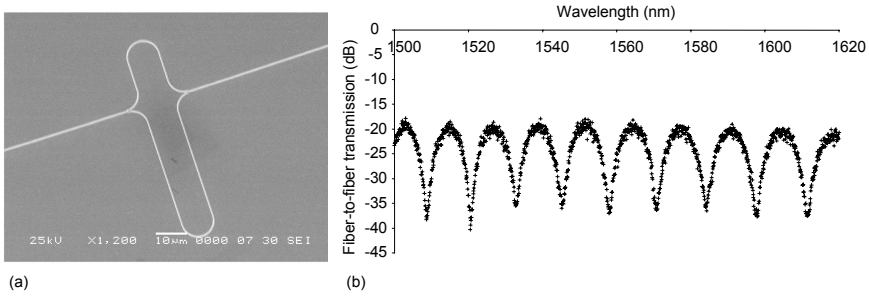

Figure 2.27: SOI Mach-Zehnder interferometer fabricated by a single-step thermal Nanoimprint Lithography process: (a) SEM-picture, (b) fiber-to-fiber transmission as a function of wavelength.

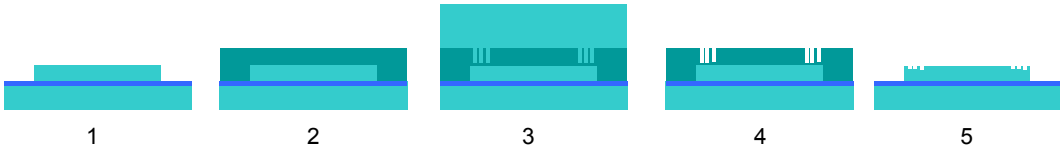

Figure 2.28: Grating coupler fabrication on SOI waveguides using a thermal nanoimprint process on top: (1) fabrication of the waveguides, (2) spincoating of PMMA, (3) imprint and thermal curing, (4) demolding and (5) break-through etch and shallow etch.

nm PMMA is spin-coated on top of the SOI chip. The mold is aligned to the substrate so that the position of the grating lines is perpendicular to the waveguides. Imprint is performed using the same parameters, but the etching time is shortened to limit the etch depth to 60 nm. Fig. 2.28 shows the process flow schematically. A microscope image of a set of waveguides that include the fabricated grating couplers is shown in Fig. 2.29, along with detailed views by SEM. The results on the optical performance of the fabricated grating couplers are discussed in the next chapter.

Within the framework of a collaboration between Dalian University of Technology in China and Ghent University, a novel simple two-step nanoimprint technique was developed for the fabrication of low-index contrast photonic integrated circuits using the PSQ-L polymer system. PSQ-L is a novel UV-curable inorganic-organic hybrid polymer with good optical properties, such as low loss, small birefringence, and excellent environmental stability [73]. By blending of the two polymers PSQ-L145 and PSQ-L151, precise and continuous control of the refractive index is possible to obtain values between 1.4543 and 1.5154 at a wavelength of 1550 nm. Fig. 2.30 shows the UV-imprint-based process to fabricate PSQ-L photonic circuits. Unlike conventional imprint processes, the imprint step is used to structure the cladding layer rather than the

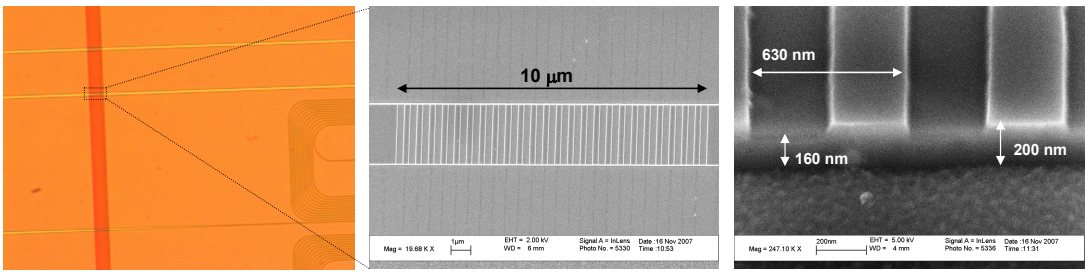

Figure 2.29: SOI grating couplers fabricated by a double-step thermal nanoimprint lithography process: (a) set of waveguides with the integrated grating coupler, (b) SEM-picture of the grating coupler, (c) SEM-picture of the tilted sample.

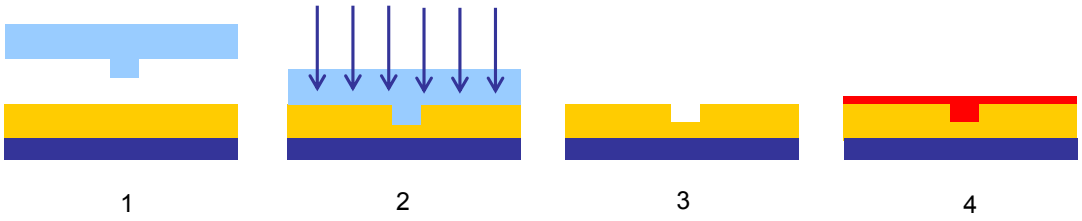

Figure 2.30: UV-imprint-based process to fabricate PSQ photonic circuits: (1) spincoating of the low refractive index polymer and PDMS mold preparation, (2) imprint and UV-curing, (3) demolding, (4) spincoating of the high refractive index polymer layer.

core layer and is followed by a spin-coating step to fill the imprinted features in the cladding layer to define the core of the waveguides. This process smartly avoids the difficulties related to controlling the thickness of the residual layer since the residual cladding layer thickness does not need to be controlled accurately as long as it is thick enough to eliminate the substrate leakage loss. First results have been obtained by applying the PDMS mold manually [74]. However, a mask aligner is also a good candidate for the fabrication of these waveguide circuits since the residual layer thickness of the imprinted polymer layer is not critical.

2.4 Nanoimprint lithography based patterning of fiber facets

2.4.1 Process and set-up

UV-based nano imprint lithography on fiber facets has been proposed and demonstrated only recently [75], so its potential remains largely unexplored, especially when other materials and more sophisticated fiber components are to be fabricated. In [76] a number of approaches have been described for the patterning of materials other than polymers on fiber facets but they all rely on conventional nano imprint techniques including pattern transfer techniques by lift-off or etching, which are all challenging processes to implement and optimize. Moreover, they require multiple processing steps and extensive fiber handling.

Our approach to define nano- and microstructures on fiber facets is by UV-NIL or UV-NITL, the first for defining polymer structures, the second for defining metal structures. The set-up is schematically represented in Fig. 2.31. The mold is prepared for UV-NIL or UV-NITL according to procedures described above and then put on a vacuum chuck to remain fixed. The fiber is prepared by simple cleaving and mounted on a micro-mechanical x,y,z-stage. A drop of PAK-01 is dispensed onto the mold. Then the fiber is dipped in the drop and moved to the pattern of interest. Then, the drop is squeezed between the fiber facet and the mold by bringing the fiber closer to the mold surface. Doing so, the mold cavities formed by the nanopattern are filled with the liquid. Next, the polymer is cured by UV-light at room temperature, either by illuminating with a glass fiber guide connected to the external UV-source (Fig. 2.32 (a)) or by illuminating with the fiber itself connected to the UV-source (Fig. 2.32 (b)). As an example, the schematic of Fig. 2.32 depicts the UV-NITL process. After curing, the fiber is lifted and demolded from the mold which is tightly hold on the chuck by suction. Any remaining uncured material is then removed by iso-propyl alcohol and blow-drying.

For those applications where maximal interaction between the optical fiber mode and the pattern on the facet is wanted, this technique has a number of distinct advantages over existing techniques. First of all, the pattern can be oriented in any direction by tilting the fiber at a pre-defined angle. Second, the pattern can be aligned with respect to the fiber core by self-alignment using UV-curing through the fiber core. Third, the number of processing steps in which the fiber is involved is kept to an absolute minimum. In fact, this technique relies primarily on the mold preparation steps so that actual fiber handling is only required in the last step. Such a single-step process is especially interesting for processing multiple fibers in parallel.

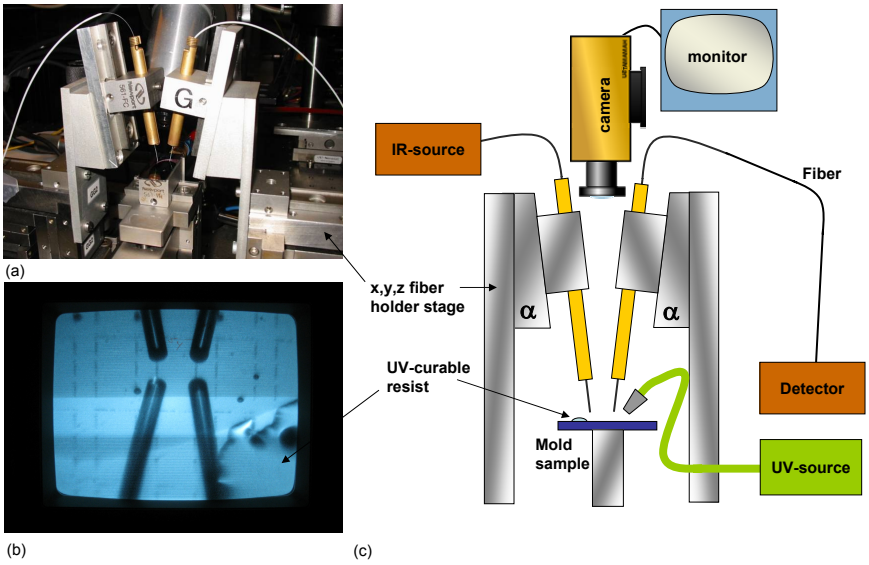

Figure 2.31: Set-up for UV-NITL on fibers: (a) picture of the setup: the mold sample is put on a vacuum chuck, the fibers are mounted by fiber holders, (b) camera image, (c) schematic of the setup.

We note that NIL-based patterning of fiber facets solves many of the processing difficulties due to the small substrate size by applying the lithography processes themselves to a carrier chip or wafer of larger size. We will show that DUV fabricated molds are very suitable for NIL-based fiber patterning, both in terms of resolution as in terms of design freedom.

2.4.2 Results

Figures 2.33 (a.1) and (a.2) show the result of UV-NITL using process flow (a) of Fig. 2.32. The full grating area on the mold was 500 μm x 1000 μm. The gold grating area transferred to the fiber is defined by the area of the resist volume in contact with the mold. It is slightly bigger than the cross section of the fiber cladding.

Figure 2.33(b.1) and (b.2) show the result of UV-NITL using process flow (b) of Fig. 2.32 on a single-mode fiber with a core-diameter of 9 μm. In this case the full grating area on the mold was 10 μm x 10 μm. By UV-curing through the fiber core, only the cylinder-shaped resist volume extending from the fiber core gets cured. Consequently, the imprint and transfer of the metal occurs only for the area of this volume in contact with the mold. As a result the metal pattern is perfectly aligned with the fiber core. The fiber was tilted 10 degrees with respect to the vertical. UV-light was applied through the fiber core by connecting the output of an EFOS Ultracure 100ss-plus system with the connector of the single-mode fiber. Curing time was set to 300 seconds. Remaining

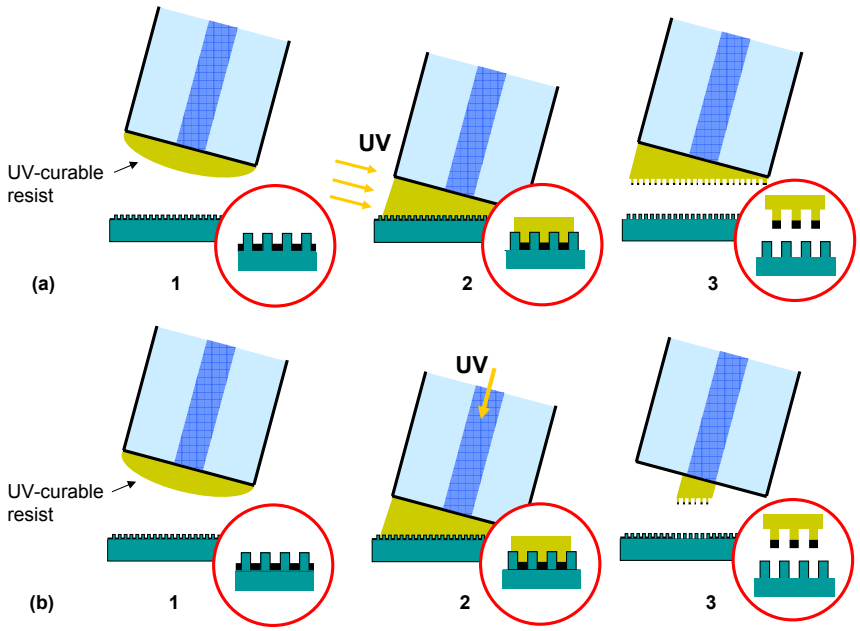

Figure 2.32: UV-nano imprint and transfer lithography (NITL) on a fiber facet using a specially prepared mold carrying the metal pattern in the mold trenches. Process flow (a) is the standard UV-NITL process: (1) positioning of the fiber with low-viscous UV-curable resist over the mold, (2) imprinting and UV-curing, (3) pattern transfer and mold release. Process flow (b) is a self-aligned UV-NITL process: (1) positioning of the fiber with low-viscous UV-curable resist over the mold, (2) imprinting and UV-curing through the fiber core, (3) pattern transfer and mold release.

uncured PAK-01 was removed by dispensing IPA onto the fiber end and subsequent blow-drying. The elliptical shape of the grating area is explained by the fiber tilt. Left of the grating in Fig. 2.33 (b.2) some excess material can be seen. These are pieces of the gold grating lines that did not break off at the edge of the cured polymer portion but a bit further. This problem is inherent to the self-alignment process and gets worse when thicker metal layers are transferred. However, this is a problem inherent to the transfer of one-dimensional periodic patterns. With two-dimensional patterns, such as metal dots instead of lines, this problem does not occur.

Components fabricated by the self-aligned UV-NITL process are critically subject to damage and handling. The smaller the size of the core and the larger the tilt of the fiber, the more fragile is the fabricated component. For those applications where the fragility is problematic, or where structures are desired which are larger than the size of the core, an active alignment procedure combined with external UV-curing is preferred instead of self-alignment. This procedure will be further detailed in chapter 6 where we will discuss an application of a fiber component based on a sub-micron period metal grating on the facet.

UV-NITL with sub-100 nm resolution has been demonstrated. The silicon master mold was fabricated by DUV-lithography and prepared for UV-NITL. Fig. 2.34 shows the result of UV-NITL using process flow (a) of Fig. 2.32. The transfer was not successful everywhere on the sample. This however aids the SEM inspection. Two regions are shown in detail. The first is a region of incomplete transfer clearly showing the gold structures that are completely or only partly covering the polymer protrusions on the fiber facet. The second is a region of complete transfer. The opening of the gold horseshoe is 80 nm.

2.5 Conclusion

In this chapter, we described various techniques for micro- and nanopatterning. In particular, we focused on UV-based nanoimprintlithography (UV-NIL) and other NIL-related techniques for micro- and nanopatterning. We explored the potential of using a conventional mask-aligner as a flexible tool for nanoimprint. We also explored the potential of DUV-lithography as base technology for the fabrication of master templates. Novel processes including double UV-NIL with lift-off for the fabrication of metal nanostructures on non-transparant substrates, 3D patterning and UV-NITL were proposed and demonstrated.

We described methods for micro- and nanopatterning of very small fiber facets. Existing methods are primiraly based on direct-write technologies, whereas NIL-based techniques offer a much higher potential, especially for integrated photonics. UV-NIL and UV-NITL on fiber facets are very suitable

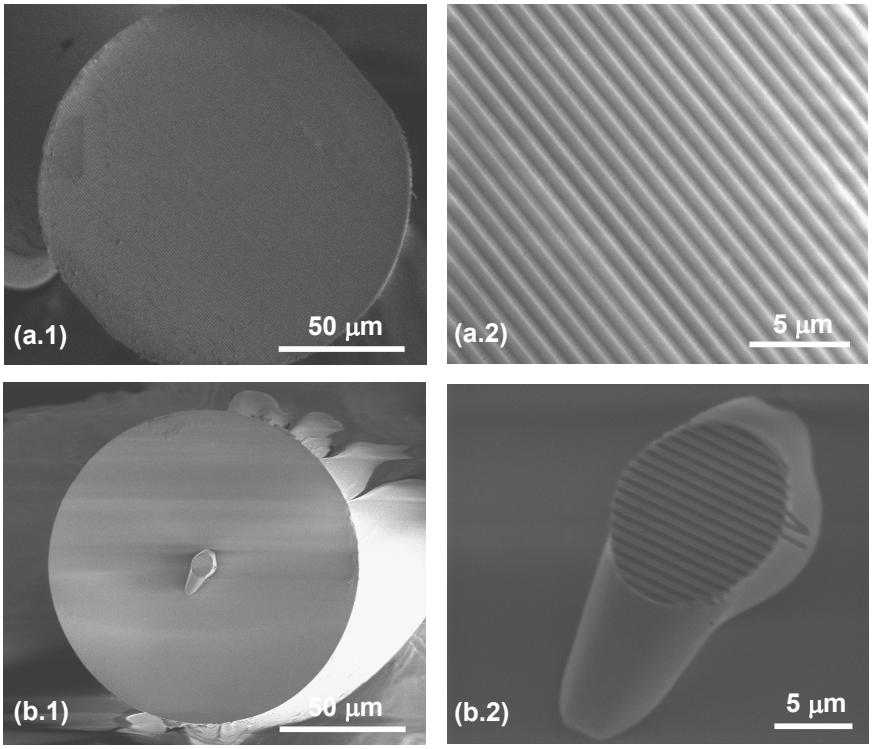

Figure 2.33: SEM pictures of metal gratings on fiber facets fabricated by UV-NITL. (a) UV-NITL of a gold grating, (a.1) facet view, (a.2) detail of the grating. (b) UV-NITL of a gold grating using self-alignment by UV-curing through the fiber core, (b.1) facet view, (b.2) detail of the grating.

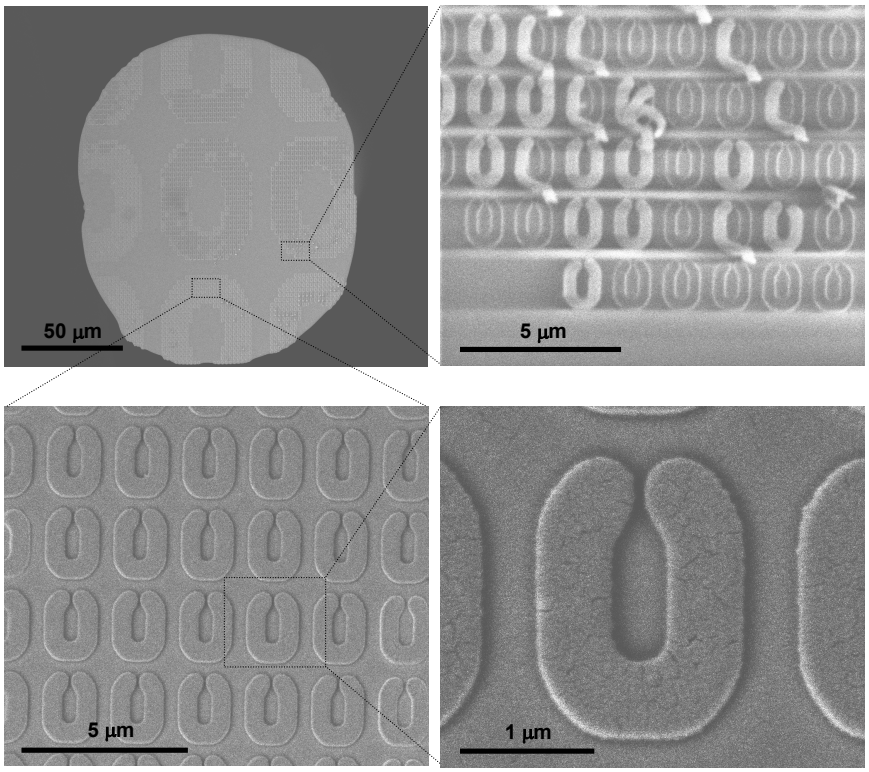

Figure 2.34: SEM pictures of gold nano-horseshoes on fiber facets fabricated by UV-NITL.

techniques for implementing light-coupling interfaces with integrated waveguides. This will become clear in chapters 5 and 6. A key component in these coupling schemes are grating couplers, which will be the subject of the next chapters.

Bibliography

[1] R.M. Langford, G. Dale, P.J. Hopkins, P.J.S. Ewen, A.K. Petford-Long "Focused ion beam micromachining of three-dimensional structures and three-dimensional reconstruction to assess their shape" *J. of Micromechanics and Microengineering* 12, pp. 111-114, 2002.

[2] T. E. Murphy "Design, Fabrication and Measurements of Integrated Bragg Grating Optical Filters" *PhD thesis*, Massachusetts Institute of Technology, 2001.

[3] K. Naessens "Excimer laser ablation of microstructures in polymers for photonic applications" *PhD thesis*, Ghent University, 2004.

[4] http://www.epixfab.eu/

[5] R. Baets, P. Dumon, W. Bogaerts, G. Roelkens, D. Taillaert, B. Luyssaert, G.R.A. Priem, G. Morthier, P. Bienstman, D. Van Thourhout "Silicon-on-insulator based Nano-photonics: Why, How, What for?," *Proc. of Group IV Photonics*, FA1, p.168-170, Belgium, 2005.

[6] G. Van Steenberghe "Parallel optical interconnections integrated on a printed circuit board" *PhD thesis*, Ghent University, 2006.

[7] V.S. Shah, L. Curtis, R.S. Vodhanel, D.P. Bour, W.C. Yang "Efficient power coupling from a 980 nm, broad-area laser to a single-mode fiber using a wedge-shaped fiber endface" *J. of Lightwave Technol.* 8, pp. 1313-1318, 1990.

[8] S.M. Yeh, Y.-K. Lu, S.Y. Huang, H.H. Lin, C.H. Hsieh, W.H. Cheng "A novel scheme of lensed fiber employing a quadrangular pyramid shaped fiber endface for coupling between high-power laser diodes and single-mode fibers" *J. of Lightwave Technol.* 22 (19), pp. 1374-1378, 2004.

[9] M. Udrea, H. Orun, A. Alacakir "Laser polishing of optical fiber end surface" *Optical Engineering* 40 (9), pp. 2026-2030, 2001.

[10] H. Karstensen, J. Wieland, R. Dal'Ara, M. Blaser "Parallel optical link for multichannel interconnections at gigabit rate" *Optical Engineering* 37 (12), pp. 3119-3123, 1998.

[11] S.K. Eah, W. Jhe, Y. Arakawa "Nearly diffraction-limited focusing of a fiber axicon microlens" *Rev. Sci. Instrum.* 74 (11), pp. 4969-4971, 2003.

[12] B. Hecht, B. Sick, U.P. Wild, V. Deckert, R. Zenobi, O.J.F. Martin "Scanning near-field optical microscopy with aperture probes: fundamentals and applications" *J. of Chemical Phys.* 112 (18), pp. 7761-7774, 2000.

[13] M. Muranishi, K. Sato, S. Hosaka, A. Kikukawa, T. Shintani, K. Ito "Control of aperture size of optical probes for scanning near-field optical microscopy using focused ion beam technology" *Jap. J. of Appl. Phys.* 36 (7B), pp. 942-944, 1997.

[14] A. Partovi, D. Peale, M. Wuttig, C. A. Murray, G. Zydzik, L. Hopkins, K. Baldwin, W. S. Hobson, J. Wynn, J. Lopata, L. Dhar, R. Chichester, J. H. Yeh "High-power laser light source for near-field optics and its application to high-density optical data storage" *Appl. Phys. Lett.* 75, pp. 1515-1557, 1999.

[15] E. Cubukcu, E. A. Kort, K. B. Crozier, F. Capasso "Plasmonic laser antenna" *Appl. Phys. Lett.* 89, 093120, 2006.

[16] L. Tang, S.E. Kocabas, S. Latif, A.K. Okyay, D.S. Ly-Gagnon, K.C. Saraswat, D.A.B. Miller "Nanometer-scale germanium photodetector enhanced by a near-infrared dipole antenna" *Nature Photonics* 2 (4), pp. 226-229, 2008.

[17] E.J. Smythe, E. Cubukcu, F. Capasso "Optical properties of surface plasmon resonances of coupled metallic nanorods" *Opt. Express* 15 (12), pp. 7439-7447, 2007.

[18] E.J. Smythe, E. Cubukcu, F. Capasso "Coupled Metallic Antenna Nanorod Arrays" *CLEO 2007* Baltimore (USA), QThE1, 2007.

[19] G. Giannini, L. Mastrogiacomo, S. Cabrini, A. Gerardino, A. Nottola, V. Foglietti, E. Cianci "Microfabrication of diffractive optical elements onto the active region of optical fiber termination" *Proc. MICRO tec. 2000.-VDE World Microtechnologies Congress* Berlin (Germany), 2, pp. 695-697, 2000.

[20] P.S. Kelkar, J. Beauvais, E. Lavallee, D. Drouin, M. Cloutier, D. Turcotte, P. Yang, L. K. Mun, R. Legario, Y. Awad, V. Aimez "Nano patterning on optical fiber and laser diode facet with dry resist" *J. Vac. Sci. and Technol. A* 22 (3), pp. 763-746, 2004.

[21] G.M. Kim, B.J. Kim, E.S. Ten Have, F. Segerink, N.F. Van Hulst, J. Brugger "Photoplastic near-field optical probe with sub-100 nm aperture made by replication from a nanomould" *J. Microsc.* 209, pp. 267-271, 2003.

[22] K. Kajikawa, K. Mitsui "Optical fiber biosensor based on localized surface plasmon resonance in gold nanoparticles" *Proc. of SPIE* Bellignham (USA), 5593, pp. 494-501, 2004.

[23] S.M. Kim, K.W. Jo, J.H. Lee "Design and fabrication of a microlens on the sidewall of an optical fiber with a metallized 45 degrees end face" *Appl. Opt.* 44 (19), pp. 3985-3991, 2005.

[24] M. Dickey, M. Stewart, G. Wilson, "NNIN Nanotechnology Open Textbook, Chapter 5 - Advanced Lithography" 2006

[25] C.R.K. Marrian, D.M. Tennant, "Nanofabrication" *J. Vac. Sci. Technol. A* 21, S207-S215, 2003.

[26] S.Y. Chou, P.R. Krauss, P.J. Renstrom "Imprint of Sub-25 Nm Vias and Trenches in Polymers" *Appl. Phys. Lett.* 67 (21), pp. 3114-3116, 1995.

[27] M. Okai, S. Tsuji, N. Chinone, T. Harada "Novel Method to Fabricate Corrugation for a Lambda/4-Shifted Distributed Feedback Laser Using a Grating Photomask" *Appl. Phys. Lett.* 55 (5), pp. 415-417, 1989.

[28] http://www.itrs.net/Links/2003ITRS/ERD2003.pdf *Ed. 2003*

[29] S.Y. Chou, P.R. Krauss, W. Zhang, L. Guo, L. Zhuang "Sub-10 nm imprint lithography and applications" *J. Vac. Sci. Technol. B* 15, pp. 2897-2904, 1997.

[30] S.Y. Chou, P.R. Krauss, W. Zhang, L. Guo, L. Zhuang "Fabrication of 60-nm transistors on 4-in. wafer using nanoimprint at all lithography levels" *Appl. Phys. Lett.* 83, pp. 1632-1634, 2003.

[31] D. J. Resnick, W. J. Dauksher, D. Mancini, K. J. Nordquist, T. C. Bailey, S. Johnson, N. Stacey, J. G. Ekerdt, C. G. Willson, S. V. Sreenivasan, N. Schumaker "Imprint lithography for integrated circuit fabrication" *J. Vac. Sci. Technol. B* 21, pp. 2624-2631, 2003.

[32] C.-y. Chao, L. J. Guo, "Polymer micro-ring resonators fabricated by nanoimprint technique" *J. Vac. Sci. Technol. B* 20, pp. 2862-2866, 2002.

[33] S.Y. Chou, S.Y. Keimel, J. Gu "Ultrafast and direct imprint of nanostructures in silicon" *Nature* 2002, pp. 835-837, 2002.

[34] J. Seekamp, S. Zankovych, A. H. Helfer, P. Maury, C. M. Sotomayor Torres, G. Boettger, C. Liguda, M. Eich, B. Heidari, L. Montelius, J. Ahopelto "Nanoimprinted passive optical devices" *Nanotechnology*, 13, pp. 581-586, 2002.

[35] C.-S. Kee, S.-P. Han, K. B. Yoon, C.-G. Choi, H. K. Sung, S. S. Oh, H. Y. Park, S. Park, H. Schift "Photonic band gaps and defect modes of polymer photonic crystal slabs" *Appl. Phys. Lett.*, 86, pp. 051101/1-051101/3, 2005.

[36] M.B. Christiansen, M. Scholer, S. Balslev, R.B. Nielsen, D.H. Petersen, A. Kristensen "Wafer-scale fabrication of polymer distributed feedback lasers" *J. Vac. Sci. Technol. B*, 24(6), pp. 3252-3257, 2006.

[37] M.B. Christiansen, M. Scholer, A. Kristensen "Integration of active and passive polymer optics" *Opt. Express*, 15(7), pp. 3931-3939, 2007.

[38] V. Reboud, P. Lovera, N. Kehagias, M. Zelsmann, C. Schuster, F. Reuther, G. Gruetzner, G. Redmond, C.M.S. Torres "Two-dimensional polymer photonic crystal band-edge lasers fabricated by nanoimprint lithography" *Appl. Phys. Lett.*, 91(15), 2007.

[39] D. Nilsson, S.Balslev, A. Kristensen "A microfluidic dye laser fabricated by nanoimprint lithography in a highly transparent and chemically resistant cyclo-olefin copolymer (COC)" *J. Micromech. Microeng.*, 15(2), pp. 296-300, 2005.

[40] W. Wu, B. Cui, X.-y. Sun, W. Zhang, L. Zhuang, L. Kong, and S. Y. Chou, "Large area high density quantized magnetic disks fabricated using nanoimprint lithography," Journal of Vacuum Science & Technology, B: Microelectronics and Nanometer Structures, vol. 16, pp. 3825-3829, 1998.

[41] G. M. McClelland, M. W. Hart, C. T. Rettner, M. E. Best, K. R. Carter, and B. D. Terris, "Nanoscale patterning of magnetic islands by imprint lithography using a flexible mold," Applied Physics Letters, vol. 81, pp. 1483-1485, 2002.

[42] M. Beck, F. Persson, P. Carlberg, M. Graczyk, I. Maximov, T. G. I. Ling, and L. Montelius, "Nanoelectrochemical transducers for (bio-) chemical sensor applications fabricated by nanoimprint lithography" *Microelectron. Eng.*, 73-74, pp. 837-842, 2004.

[43] J. D. Hoff, L.-J. Cheng, E. Meyhoefer, L. J. Guo, A. J. Hunt "Nanoscale Protein Patterning by Imprint Lithography" *Nano Lett.*, 4, pp. 853-857, 2004.

[44] W. Reisner, K. J. Morton, R. Riehn, Y. M. Wang, Z. Yu, M. Rosen, J. C. Sturm, S. Y. Chou, E. Frey, R. H. Austin "Statics and Dynamics of Single DNA Molecules Confined in Nanochannels" *Phys. Rev. Lett.*, 94, pp. 196101/1-196101/4, 2005.

[45] M. C. McAlpine, R. S. Friedman, and C. M. Lieber "Nanoimprint Lithography for Hybrid Plastic Electronics" *Nano Lett.*, 3, pp. 443-445, 2003.

[46] M. D. Austin, S. Y. Chou "Fabrication of 70 nm channel length polymer organic thin-film transistors using nanoimprint lithography" *Appl. Phys. Lett.*, 81, pp. 4431-4433, 2002.

[47] X. Cheng, Y. Hong, J. Kanicki, L. J. Guo "High-resolution organic polymer light-emitting pixels fabricated by imprinting technique" *J. Vac. Sci. Technol. B*, 20, pp. 2877-2880, 2002.

[48] Y. Huang, G. T. Paloczi, J. K. S. Poon, A. Yariv "Bottom-up soft-lithographic fabrication of three-dimensional multilayer polymer integrated optical microdevices" *Appl. Phys. Lett.*, 85, pp. 3005-3007, 2004.

[49] A. Kumar, G.M. Whitesides "Features of Gold Having Micrometer to Centimeter Dimensions Can Be Formed through a Combination of Stamping with an Elastomeric Stamp and an Alkanethiol Ink Followed by Chemical Etching" *Appl. Phys. Lett.*, 63 (14), pp. 2002-2004, 1993.

[50] Y.L. Loo, R.L. Willett, K.W. Baldwin, J.A. Rogers "Additive, nanoscale patterning of metal films with a stamp and a surface chemistry mediated transfer process: Applications in plastic electronics" *Appl. Phys. Lett.*, 81 (3), pp. 562-564, 2002.

[51] A. Ruiz, A. Valsesia, F. Bretagnol, P. Colpo, F. Rossi "Large-area protein nano-arrays patterned by soft lithography" *Nanotechnology*, 18 (50), 2007.

[52] "Alternative Lithography", edited by C.M.S. Torres *Kluwer Academic Publishers*, 2002.

[53] H. C. Scheer, H. Schulz "A contribution to the flow behavior of thin polymer films during hot embossing lithography" *Microelectronic Engineering* 56, pp. 311-332, 2001.

[54] S.V. Sreenivasan, I. McMackin, F. Xu, D. Wang, N. Stacey, D. Resnick "Enhanced nanoimprint process for advanced lithography applications" *Semiconductor Fabtech* 25, 2005.

[55] N.V. Le, W.J. Dauksher, K.A. Gehoski, K.J. Nordquist, E. Ainley, P. Mangat "Direct pattern transfer for sub-45 nm features using nanoimprint lithography" *Microelectronic Engineering* 83, pp. 839-842, 2005.

[56] J. Israelachvili "Intermolecular and surface forces" *Academic Press* ISBN 0-12-375181-0

[57] H. Schmitt, L. Frey, H. Ryssel, M. Rommel, C. Lehrer "UV nanoimprint materials: Surface energies, residual layers, and imprint quality" *J. Vac. Sci. Technol. B*, 25 (3), pp. 785-790, 2007.

[58] M. Otto, M. Bender, B. Hadam, B. Spangenberg, H. Kurz "Characterization and application of a UV-based imprint technique" *Miroelectronic Engineering* 57-58, pp. 361-366, 2001.

[59] A. Kocabas, A. Aydinli "Polymeric waveguide Bragg grating filter using soft lithography" *Opt. Express*, 14 (22), pp. 10228-10232, 2006.

[60] M. Bender, M. Otto, B. Hadam, B. Spangenberg, H. Kurz "Multiple imprinting in UV-based nanoimprint lithography: related material issues" *Microelectronic Eng.*, 61-62, pp. 407-413, 2002.

[61] G. Roelkens "Heterogeneous III-V/Silicon Photonics: Bonding Technology and Integrated Devices" *PhD*, Ghent University, 2005.

[62] C. Stuart, Q. Xu, R.J. Tseng, Y. Yang, H.T. Hahn, Y. Chen, W. Wu, R.S. Williams, "Nanofabrication module integrated with optical aligner" *J. Vac. Sci. Technol. B* 24 (2), pp. 539-542, 2006.

[63] D. G. Choi, J.H. Jeong, Y.S. Sim, E.S. Lee, W.S. Kim, B.S. Bae "Fluorinated organic-inorganic hybrid mold as a new stamp for nanoimprint and soft lithography" *Langmuir*, 21 (21), pp. 9390-9392, 2005.

[64] A. Fuchs, B. Vratzov, T. Wahlbrink, Y. Georgiev, H. Kurz "Interferometric in situ alignment for UV-based nanoimprint" *J. Vac. Sci. Technol. B*, 22 (6), pp. 3242-3245, 2004.

[65] P. Voisin, M. Zelsmann, R. Cluzel, E. Pargonm, C. Gourgon, J. Boussey "Characterisation of ultraviolet nanoimprint dedicated resists" *Microelectronic Eng.*, 84(5-8), pp. 967-972, 2007.

[66] www.scientific.net/pdffile/46235.pdf

[67] G.Y. Jung, S. Ganapathiappan, D.A.A. Ohlberg, D.L. Olynick, Y. Chen, W.M. Tong, R.S. Williams "Fabrication of a 34 x 34 crossbar structure at 50 nm half-pitch by UV-based nanoimprint lithography" *Nano Lett.*, 4 (7), pp. 1225-1229, 2004.

[68] U. Plachetka, M. Bender, A. Fuchs, B. Vratzov, T. Glinsner, F. Lindner, H. Kurz "Wafer scale patterning by soft UV-nanoimprint lithography" *Microelectronic Eng.*, 73-74, pp. 167-171, 2004.

[69] U. Plachetka, N. Koo, T. Wahlbrink, J. Bolten, M. Waldow, T. Ploetzin, M. Foerst, H. Hurz "Fabrication of Photonic Ring Resonator Device in Silicon Waveguide Technology Using Soft UV-Nanoimprint Lithography" *IEEE Phot. Technol. Lett.* 20 (7), pp. 490-492, 2008.

[70] J.-W. Kim, K.-Y. Yang, S.-H. Hong, H. Lee "Formation of Au nano-patterns on various substrates using simpliefied nano-transfer printing method" *Appl. Surf. Sci.* 254, pp. 5607-5611, 2008.

[71] H. Schmid, B. Michel "Siloxane polymers for high-resolution, high-accuracy soft lithography" *Macromolecules*, 33 (8), pp. 3042-3049, 2000.

[72] J. Schrauwen "Focused Ion Beam for nanophotonic applications" *PhD thesis*, 2009.

[73] H.B. Zhang "A study on liquid hybrid material for waveguides - Synthesis and property of PSQ-Ls for waveguides" *J. Macromolec. Sci. Part a - Pure Appl. Chem.* 45(3), pp. 232-237, 2008

[74] J. Teng, S. Scheerlinck, H. Zhang, X. Jian, M. Zhao, G. Morthier, D. Van Thourhout, R. Baets "Fabrication of polymer ring resonators by a novel imprint technique" submitted to IEEE Phot. Technol. Lett.

[75] J. Viheriala, T. Niemi, J. Kontio, T. Rytkonen, M. Pessa "Fabrication of surface reliefs on facets of singlemode optical fibres using nanoimprint lithography" *Electronic Lett.*, 43 (3), pp. 150-152, 2007.

[76] J. Viheriala, N. Tapio, M. Pessa "A method for patterning an optical element" *European Patent Application* EP 1795927 A1, 2005.

[77] A. Borreman, S. Musa, A.A.M. Kok, M. B. J. Diemeer, A. Driessen "Fabrication of Polymeric Multimode Waveguides and Devices in SU-8 Photoresist Using Selective Polymerization" *Proc. IEEE/LEOS Benelux Chapter Symposium*, p. 83 (2002).

[78] http://mems.gatech.edu/msmawebsite/members/processes/processes-files/SU8/SU-8.htm

[79] MicroChem Nano^{TM} SU-8 Negative Tone Photoresist Formulations 2-25: data sheets and http://www.microchem.com/products/pdf/SU-82000DataSheet2100and2150Ver5.pdf

[80] S. MacDonald, G. Hughes, M. Stewart, F. Palmieri, C. G. Willson, "Design and fabrication of highly complex topographic nano-imprint template for dual Damascene full 3-D imprinting" *Proceedings of SPIE-The International Society for Optical Engineering* , vol. 5992, pp. 786-794, 2005.

3

Out-of-plane grating couplers

THE coupling problem is an important problem in nanophotonics. Efficient and broadband coupling of light into or out of photonic chips is not straightforward due to the mismatch between the mode size of an optical fiber and the typical mode size in a photonic chip waveguide. The problem is of increasing importance when the chip is made in a high refractive index contrast material system such as silicon-on-insulator. Out-of-plane grating couplers are a thouroughly studied and elegant solution to the coupling problem. Grating couplers play an important role in our work and will be reviewed in this chapter.

3.1 Introduction

In this chapter, we review the principles of grating couplers for out-of-plane coupling into and out of photonic integrated circuits. For an in-depth theoretical and experimental study and comparison of simulation methods we refer to [1] and [2]. In these references, all of the design work was targeted towards grating couplers defined by etching a grating into a waveguide layer. In this chapter, we introduce a novel kind of grating coupler defined by deposition of a grating on top of the waveguide rather than etching into the waveguide. We will also explain the relevance of this approach.

3.2 Basics and definitions

Let us consider an output grating coupler (Fig. 3.1 (a)). A grating coupler is a periodic variation of the refractive index and can take different forms, as depicted in Fig. 3.1 (b). When a guided mode with propagation constant β is incident on the grating, scattering by the subsequent refractive index contrast interfaces will cause diffraction. The propagation constant of the diffracted waves β_z are related to β via:

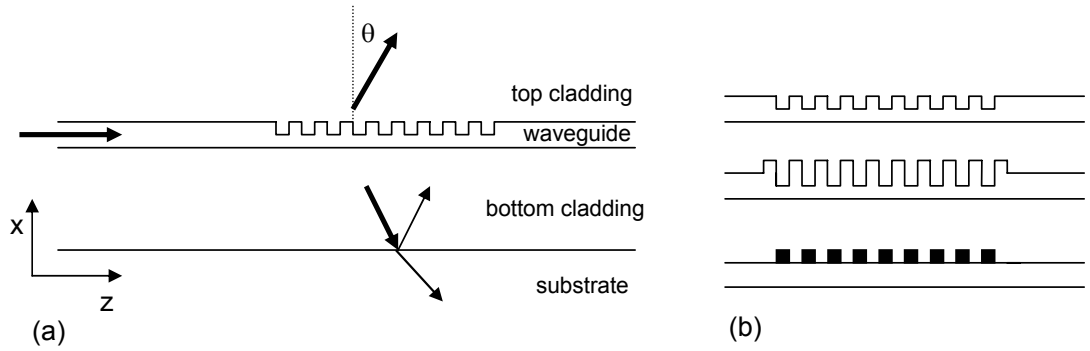

Figure 3.1: (a) Output coupling from a thin film waveguide using a grating coupler. (b) Different possible grating coupler lay-outs.

$$\beta_z = \beta + m\frac{2\pi}{\Lambda} - j\alpha/2, m = 0, \pm 1, \pm 2, ... \tag{3.1}$$

where Λ is the period of the grating and m is the order of diffraction.
The real part of Eq. 3.1 is the well known Bragg condition:

$$\beta_{\mathbf{z}} = \beta + \mathbf{mK} \tag{3.2}$$

with $\beta = \frac{2\pi}{\lambda_0} n_{eff}$ and $K = \frac{2\pi}{\Lambda}$. Bragg's condition gives the direction of the diffraction orders. A schematic representation of this relationship is shown in

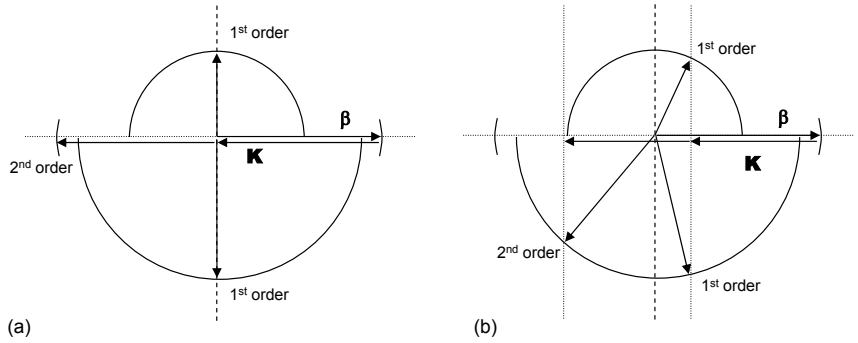

Figure 3.2: Wave-vector diagram for a waveguide grating coupler. (a) Diagram corresponding to a second-order grating, (b) Diagram corresponding to a grating with one diffraction order into the low index half space and with two diffraction orders into the high index half space.

the wave-vector diagram in Fig. 3.2, depicting the wave vector diagrams of two different types of grating couplers. The radius of the half circles is determined by the refractive index of the top- and bottom cladding respectively and is equal to $|k_0 n_{1,2}|$. The first case depicted in Fig. 3.2 is a so-called second-order grating: the first diffraction order couples light out of the waveguide in the vertical direction and the second diffraction order reflects light back into the waveguide. This case only occurs for a wavelength $\lambda = n_{eff}\Lambda$ and is also called the resonant case. However, the grating couplers we work with throughout this work are of the second type in Fig. 3.2. In this type of grating coupler the period is chosen such that the first diffraction order couples light in the direction which is slightly off the vertical. This is a much more advantageous design as it avoids the second order reflection back into the waveguide. As is clear from the graph, there will be diffraction towards the upper low index half space as well as towards the lower high index half space.

Bragg's condition tells us which diffraction orders can occur, but says nothing about the diffraction efficiencies. Here, the imaginary part of Eq. 3.1 comes into play. When the guided mode is incident on the grating, energy from the guided mode leaks into the diffracted orders, so that the energy from the guided mode decreases exponentially:

$$P_{wg}(z) = P_{wg}(z = 0)\exp(-\alpha z). \tag{3.3}$$

This leackage factor α is also called the coupling strength or grating strength. It determines the length scale needed for the light to be extracted from the waveguide (the inverse of the coupling strength is defined as the coupling length $L_c = (\alpha)^{-1}$). The grating strength is largely determined by the refractive index contrast induced by the grating element and also by the shape of the grating element. We will come back to this later in this chapter. For a uniform grating,

the coupling strength is constant as a function of z. When α is high, the grating is called a strong grating. The higher α, the stronger is the grating and the shorter is the coupling length. When α is small, the grating is called a weak grating.

In a finite structure there is not exactly one vector for which diffraction occurs, but a range of propagation vectors around the one predicted by the Bragg condition. The extent of this range or in other words the bandwidth will depend on the coupling strength of the grating coupler. For very weak gratings, α is very low and the spectrum of the outcoupled light will be very sharp. For stronger gratings, the bandwidth will increase.

The grating couplers we use in this work are designed to couple light between optical fibers and waveguides efficienctly. A high coupling strength is the key to design them. Given that the core diameter of a single mode optical fiber has a diameter of about 10 μm, light should be extracted from the waveguide over a length scale as short as about 10 μm to couple to the fiber with relevant efficiency. The coupling efficiency is optimal when the overlap between the field profile of the mode supported by the single mode fiber and the field profile of the field diffracted by the grating is maximal. In particular, for the guided mode of a single mode fiber approximated by a Gaussian profile with beam diameter of 10.4 μm and for an exponentially decaying field profile with coefficient α, the maximum overlap is 80 % and occurs for $\alpha = 0.13$, which corresponds to a coupling length of $L_c = 3.8\mu m$. An overlap of 97 % can be obtained by locally varying the grating strength, for example by varying the filling factor of the grating or the etch depth. As a result of the high grating strength, the bandwidth will also be relatively large.

Modeling tools are needed to calculate the energy that is extracted from the waveguide and to incorporate side-effects such as the reflection from interfaces close to the grating coupler (see Fig. 3.1 (a)). Once the field of the outcoupled light is known, the coupling efficiency to fiber can be calculated from the following overlap integral:

$$\eta = \left| \int \int_S E \times H^*_{fiber} dS \right|^2 \tag{3.4}$$

where S is the facet of the fiber.

3.3 Simulation tools

In this work, we worked with two different and complementary simulation methods to model grating couplers: eigenmode expansion method and finite-difference time domain (FDTD) method. All our simulations are 2D simulations. That means we assume the structure to be invariant in one of the three dimensions. Fig. 3.3 shows the original 3D model and the corresponding 2D

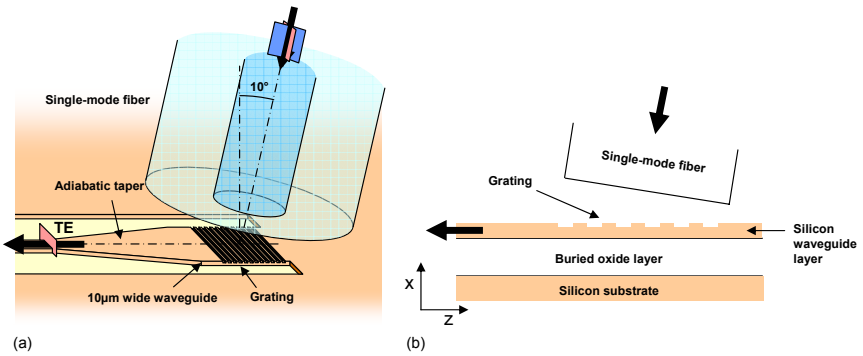

Figure 3.3: (a) Original 3D model of fiber-to-waveguide coupling via a grating coupler etched in an SOI waveguide. (b) 2D simulation model.

simulation model for the standard fiber-to-waveguide coupling scheme via an SOI grating coupler.

3.3.1 Eigenmode expansion

Eigenmode expansion works as follows. The structure is geometrically defined in a simulation space of certain dimensions and divided into sections. In each section the refractive index does not change along the propagation direction z. This is shown in Fig. 3.4. In a first step the eigenmodes of every section are calculated. These modes are the guided modes as well as a number of radiation modes. The total field in the section can be written as a linear combination of these eigenmodes. In a 2D-problem these sections are slab waveguides. All these sections together form the total structure or stack. By using a mode-matching technique at the interfaces between the sections, the scattering matrix of the entire stack is calculated. This scattering matrix gives the transmission through or reflection from the stack and hence of the entire structure. The fields at any point in the (x,z)-plane can be calculated for a given excitation. We always use the fundamental mode of the input waveguide as excitation. Perfectly matched layers (PML) are used as a boundary condition. This is an artificial material that absorbs the incident radiation and does not reflect it back into the simulation space. We use CAMFR, a two-dimensional fully vectorial simulation-tool based on eigenmode expansion and mode propagation with perfectly matched layer (PML) boundary conditions [4].

To obtain numerically stable results with eigenmode expansion using CAMFR, it is important to scan the parameter space of N, d and PML, whereby N is the number of modes that are taken into account in the calculations, d is the distance between the structure and the boundaries, and PML is the PML thickness of the boundaries. Typically, a convergence analysis is performed whereby a certain output variable - for example the transmission through the stack - is

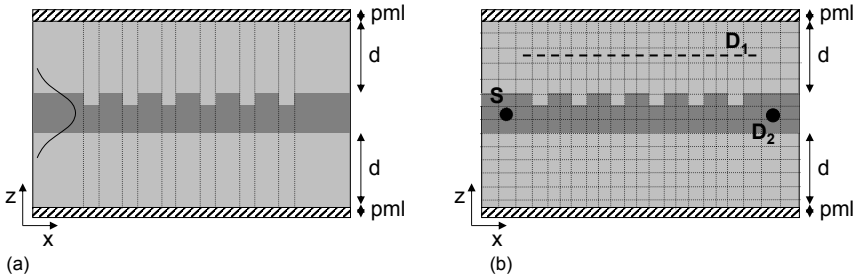

Figure 3.4: (a) Eigenmode expansion method. The structure is divided into sections. In each section the refractive index does not change along the propagation direction. (b) Finite difference time domain method (FDTD). The computational domain is divided into small cells (in practice much smaller than in the figure). S represents a source, D_1 and D_2 represent detectors.

followed as a function of these parameters. Based on such an analysis, a set of parameters is chosen that leads to stable results.

When the structure contains lossy materials such as metals, CAMFR contains complementary methods to deal with these materials. We will come back to this issue when we discuss the design of metal grating couplers in the next chapter.

For the simulation of a grating coupler, the waveguide mode is incident from the left and is normalized to the input power. The refractive index of the area between grating and fiber can be matched to the index of the fiber, representing an index matching glue which is sometimes used in practice to enhance the coupling efficiency. In a first step reflection and transmission of the entire structure is calculated. Second, the power flux and overlap with the fiber mode is calculated from the field diffracted by the grating. The fraction of the input power that couples to the fiber mode is then defined as the coupling efficiency.

3.3.2 Finite difference time domain

This method works by discretizing Maxwell's laws in space and time. The electric and magnetic fields are calculated in each point of the spatial grid on subsequent steps in the time domain. The derivatives in Maxwell's laws are hereby replaced by finite differences. All calculations are done in the time domain so that the spectral response of the system can be easily determined by a Fourier-transform of an impuls response.

A small grid is necessary to obtain accurate results: the size of a cell should be small enough compared to the wavelength of the simulation and should also be small enough to cover the smallest structures in the simulation area with sufficient cells. However, using smaller cells and hence more grid points

results into longer calculation times. To limit the calculation times, the commercial simulation package *OmniSim* 4.0 (*Photon Design*) allows to work with a so-called subgrid. This is a local grid which can be applied to a curtain region in the simulation structure with cell sizes that are a factor smaller than the cell sizes of the basic grid. By using subgrids, calculation times can be greatly reduced [**?**].

To calculate the coupling efficiency of a grating coupler, we typically worked with a source that excites the fundamental Gaussian mode of the single-mode fiber. The fundamental waveguide mode is excited upon incidence of this fiber mode. Detectors were placed above the grating and in the waveguide to calculate how much power of the original incident fiber mode couples to the waveguide mode. This is the coupling efficiency. Just like in eigenmode expansion, we used PML boundary conditions to avoid reflections at the boundaries of the computational domain.

3.3.3 3D approximation using 2D calculations

The coupling problem is a 3D-problem. Results from 2D calculations thus need to be interpreted correctly in order to obtain coupling efficiency data corresponding to the 3D situation. In particular, the waveguides have limited width and the waveguide-to-fiber coupling efficiency will be less than what is calculated in a 2D simulation. To quantify this 3D-effect, we calculate the overlap integral between the waveguide mode and the fiber mode. We assume that the electric field of the fundamental mode of the finite width waveguide $\psi(x, y)$ can be written as a multiplication $\psi_1(x).\psi_2(y)$ of the lateral mode profile $\psi_1(x)$ and the transversal mode profile $\psi_2(y)$. This assumption is valid when the waveguide width is large enough with respect to its height. The overlap integral can thus be written as [5]:

$$\eta = \left| \int\int E(x)E(y=y_0,z)Ae^{-\frac{(x-x_0)^2+(z-z_0)^2}{w_0^2}} e^{jn\frac{2\pi}{\lambda z \sin\theta}} dxdz \right|, \qquad (3.5)$$

where the constant A represents the normalization of the Gaussian beam and w_0 is equal to 5.2 μm, as we saw in section 3.2. The formula can be separated in two terms, one dependent on x and the other dependent on z. If we call the x-dependent term ξ, the coupling efficiency to fiber is the coupling efficiency of a 2-D problem multiplied by the correction factor ξ. We calculate ξ for the silicon-on-insulator (SOI) material system consisting of a 220 nm top silicon layer and a 2 μm buried oxide layer. The result of this calculation is plotted as a function of waveguide width in Fig. 3.5. Over the inspected waveguide width range (1 μm up to 40 μm), the effective index of the fundamental TE mode that is supported by these waveguides varies only slightly and differs from the effective index of the SOI slab mode (2.8309) by less than

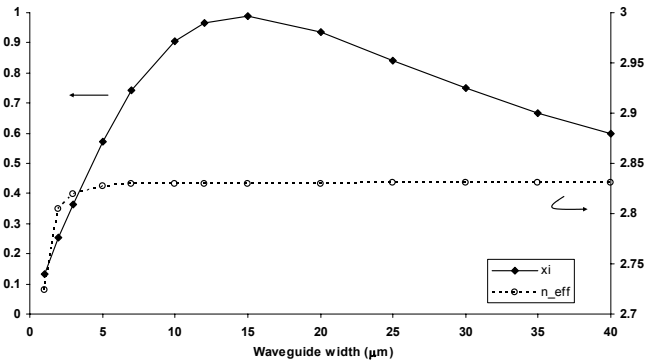

Figure 3.5: 3D-correction factor for calculating the coupling efficiency for the full 3D-case from 2D simulations as a function of SOI waveguide width.

1% for the waveguides with a width of at least 2 μm. This indicates that the approximation is valid. From Fig. 3.5, it follows that there is an optimal waveguide width for which the coupling efficiency calculated in 2D differs by only 0.5 % from the 3D case. The optimal waveguide width is 15 micron and the 3D-correction factor is 0.995. Furthermore, it follows that there is reasonable coupling to smaller and wider waveguides. The 3D-correction factor is above 50 % for waveguide widths above 2 micron.

The 3D effect is demonstrated by the experimental results plotted in Fig. 3.6. The coupling efficiency of SOI grating couplers of width 10 μm and 3 μm is plotted. The 10 μm wide grating couplers are used as a standard for SOI photonic circuits and were fabricated on the silicon platform using DUV lithography and ICP etching. The 3 μm wide grating couplers were fabricated by thermal nanoimprint lithography and RIE etching. The difference in coupling efficiency matches with the calculated 3D-correction factor. The slight difference in spectral maximum is due to differences in the grating geometry primiraly related to the different fabrication.

3.4 Experimental tools

The set-up we used for evaluating the coupling efficiency of grating couplers and grating coupler based devices is depicted in Fig. 3.7. The sample containing waveguides with grating couplers is fixed on the vacuum chuck. An input fiber is connected to an IR source and an output fiber is connected to a detector. Depending on the application, we used a broadband superluminescent light-emitting diode (SLED) as the source together with a spectrum analyser as the detector or a tunable laser source in conjunction with a power detector. Polarization wheels are used to control the polarization of the light at the input of the device. The angle of incidence of the light corresponds to the angle be-

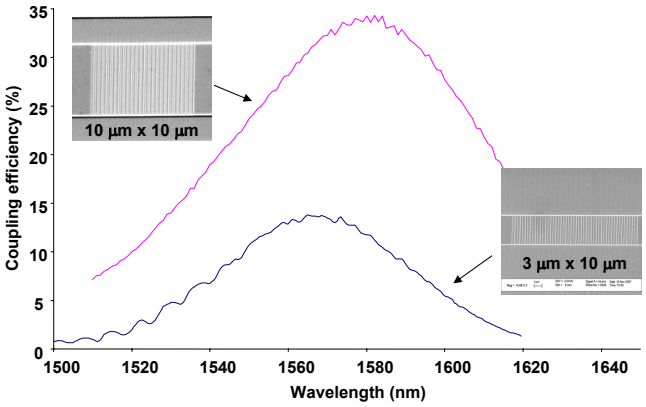

Figure 3.6: Comparison of the experimentally determined coupling efficiency between SOI grating couplers of width 10 μm (fabricated with DUV lithography and ICP etching) and width 3 μm (fabricated by nanoimprint lithography and RIE etching).

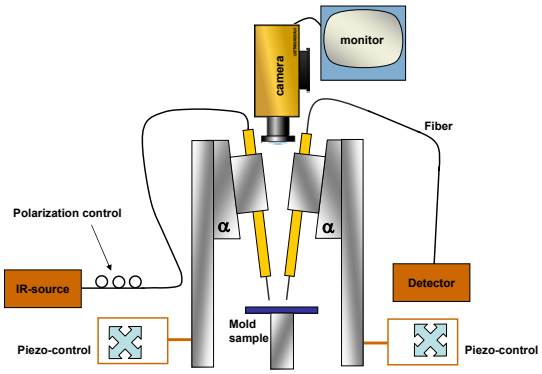

Figure 3.7: Measurement setup for vertical fiber-to-waveguide coupling. The angle of incidence α can be changed.

tween the vertical and the fiber holder α which can be changed manually. This set-up was used for characterization of fibers with angled facet, grating couplers with polymer angled facet overlayers, metal-grating couplers, and metal grating based fiber probes.

The fiber-in fiber-out transmission experiment with near-to-vertical coupling (θ=10^o) makes the calculation of the coupling efficiency rather simple. There are no resonances and thus no unwanted second-order reflections from the grating and thus no unwanted cavity formation. If we assume that the input and output coupling efficiency are the same, the relation between the transmission T and the efficiency η is given by:

$$T = \eta_{in}\eta_{out} = \eta^2 \Rightarrow \eta = \sqrt{T}. \tag{3.6}$$

If the coupling conditions at the input and output are not exactly the same, the efficiency is slightly underestimated and the bandwidth slightly overestimated. Thus care should be taken that the two grating couplers or systems under test are close to identical. This is especially important when serial processes are used for the fabrication such as electron beam lithography. To overcome this problem, a fiber-in cleaved facet-out measurement could be carried out instead of a fiber-in fiber-out measurement. The advantage is that only one system has to be fabricated. However, this measurement requires high quality facets, preferably coated with an anti-reflection coating. If this is not the case, the interpretation of measurement data from such a measurement is very difficult due to high reflections at the facet and/or additional scattering due to facet imperfections. For more details about this measurement technique, we refer to [1]. In this work, we chose for the fiber-in fiber-out technique for its simplicity and straightforward interpretation of measurement data.

3.5 State-of-the-art: fiber coupling

Simple uniform grating couplers are most easy to fabricate and are currently used as a standard for SOI integrated circuits [7]. For SOI, over 30 % coupling efficiency has been demonstrated [1] for these couplers and 69 % has been obtained by including a bottom mirror [8]. With more elaborate non-uniform and asymmetric grating designs even higher coupling efficiencies should be possible [9], [14]. Given that one-dimensional structures are highly polarization dependent, a polarization diversity scheme based on a two-dimensional grating coupler can be used in practical applications [11]. Moreover, by working with elliptically shaped grating lines or dots, focusing of light can be obtained [12].

All of these grating couplers have in common that the grating is designed in such a way that optimal coupling occurs when the optical fiber is slightly tilted with respect to the vertical axis, typically 10° off the vertical. This is necessary to avoid a large secondary order Bragg reflection back into the waveguide. Such reflections might deteriorate the optical performance of the integrated circuit and also reduce the coupling efficiency. However, the requirement of slightly tilting the fiber compromises the applicability of these grating couplers for testing and packaging purposes. First of all, the tilting needs the be done in the right vertical plane, namely the plane defined by the waveguide and the normal to the waveguide. When the incidence plane is rotated with respect to the optimal plane, the coupling efficiency decreases. Moreover, for packaging, the tilting requires angled polishing of the fiber ferrule and mounting of the ferrule under an angle with respect to the substrate normal direction, which is a costly complication in the packaging.

A coupling scheme in which the fiber is in a perfectly vertical position with respect to the waveguide plane is much more attractive. Fiber ferrule polishing

becomes unnecessary, alignment of the fiber to the grating coupler allows full rotational freedom of the fiber, and the space volume needed for testing is minimal. This understanding has led to novel designs for the grating coupler. One very promising approach is to incorporate extra slits in the waveguide layer that act as a mirror in order to achieve destructive interference of the second order Bragg reflections [10]. Slanted gratings couplers based on angled slits are another solution [13]. However, the fabrication of these types of grating couplers is extremely challenging [14], [15]. We came up with a simple alternative approach for vertical coupling which will be the subject of chapter 5.

3.6 State-of-the-art: free-space coupling

Compact grating couplers also allow for coupling to and from photonic chips in free-space. This means that photonic chips can be excited or read-out from a distance without the need for optical fibers. What is needed is an appropriate illumination and read-out system. When using a laser as the illumination source, the laser beam diverges and the illuminated spot is much bigger than the beam size escaping the laser source. In particular, the illuminated area S is equal to $\pi(L \tan \frac{\lambda}{\pi w})^2$ with λ the wavelength of the laser, L the distance between laser source and chip and w the radius of the laser beam. As an example, a 1.55 μm laser with a diaphragm of 5 μm illuminates an area as big as 20 cm x 20 cm at a distance of 1 m. Due to the strong divergence, the power that can be coupled into a photonic chip P_{in} is only a fraction of the original power and the power coupled back out is only a fraction thereof. When each grating coupler covers an area of $S_{grating}$, the power accepted by the grating coupler is $P_{in} = \frac{S_{grating}}{S} P$ so that the power coupled out of the chip is: $P_{out} = \eta^2 P_{in}$.

Let us take the example of SOI photonic chips illuminated from a distance of 1m. For a 1mW source, the power accepted by a grating coupler is 4 pW. Thus, the power coupled back out is of the order of 1 pW depending on the efficiency of the grating couplers. This power level seems extremely low. Nevertheless, with InGaAs cameras from Xenics it is no problem to detect these low power levels. As an example, XenICs cameras equipped with Peltier cooling elements allow the detection of power levels in the order of 10 fW [16] (the cooling is necessary to reduce the noise level). The example illustrates that photonic chips can be used in a remote setup, being illuminated and read out from a distance. This enables the excitation and read-out of multiple components on a chip and even multiple chips at the same time. At Ghent University, the potential of remote read-out of photonic chips is being explored for optical markers [16], [17], and for rapid, quantitative and large-scale parallel detection of biomolecules using SOI microring-based photonic chips [18].

3.7 Low-index versus high-index contrast waveguide platforms

In this work, we concentrate on high-index contrast waveguide platforms and silicon-on-insulator in particular. All of the components described in the next chapters are based on high index contrast grating couplers and are designed and demonstrated for the SOI platform. However, they may also find applications for low-index contrast platforms. In this section we would like to make one step aside and focus on grating couplers for low-index contrast waveguide platforms.

In the literature, compact grating couplers have only been reported for high-index contrast material platforms for the simple reason that low-index contrast gratings do not offer the grating strength needed to couple light over a short length scale. Grating couplers for low-index contrast waveguides do exist but they are very long gratings defined over several hundreds of micrometers long and thus not suited to achieve efficient coupling to an optical fiber. Here we present a simple approach to increase the grating strength by integrating another material.

To obtain a grating at an interface, a refractive index variation is needed. Conventional grating couplers are defined by etching a grating with the desired period and filling factor into the waveguide layer. For high index contrast waveguide platforms such as silicon-on-insulator or indiumphosphide membranes, this approach has proven extremely valuable. However, for low index contrast waveguide platforms, this approach is not interesting at all as the index variations are too small to obtain a strong grating needed for the grating coupler.

Let us compare the coupling strength of a grating etched in a high index contrast silicon-on-insulator (SOI) platform with a grating etched in a low index contrast alumina-on-quartz (AOQ) platform. The details of both waveguide platforms are found in Table 3.1. The coupling strength α is extracted from the power transmission of the fundamental waveguide mode calculated for an increasing number of grating periods. The SOI grating coupler has a period of 630 nm and the AOQ grating coupler has a period of 1050 nm. These periods are close to the periods predicted by Bragg's condition but not too close to avoid second order reflections back into the waveguide. In both cases, a filling factor of 50 % is chosen. In Fig. 3.8, the calculated coupling strength is plotted as a function of etch depth.

For the high-index contrast SOI waveguide, the strength of the grating can be tuned over a wide range by controlling the etch depth. In the low-index contrast AOQ waveguide, the grating strength is much lower and far less tunable. Even for gratings etched very deeply into the polymer membrane, the grating strength remains very low. As a result, out-of-plane coupling of light

Table 3.1: Grating coupler data for low/high index contrast waveguide platforms

Platform	n_{core}	n	Core thickness	Cladding thickness
SOI	3.476	1.444	200 nm	2 μm
AOQ	1.7	1.45	400 nm	3 μm

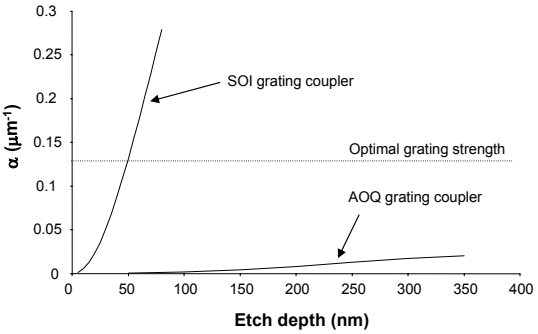

Figure 3.8: Calculated coupling strengths of a conventional silicon-on-insulator (SOI) grating coupler and an alumina-on-quartz (AOQ) grating coupler as a function of etch depth. Details of the waveguide platforms are found in Table 3.1.

from waveguide to fiber using etched grating couplers can only be made very efficient for a high-index contrast platform such as SOI, but remains very inefficient for a low-index contrast platform such as AOQ.

The key to solve the coupling problem for the low-index contrast AOQ platform is to enhance the index variations of the grating between the core and the cladding. At this point we would like to introduce a second type of grating coupler. Instead of etching a grating in the waveguide layer, this type of grating coupler is defined by depositing a grating on top of the waveguide, as is illustrated in Fig. 3.1 (b). This type of grating coupler gives a lot more freedom in controlling the coupling strength as a different material can be chosen to provide a suitably high index contrast and thus a suitably high coupling strength of the grating coupler. Such a material is silicon.

In Fig. 3.9 the calculated coupling strength is plotted of a grating coupler consisting of a silicon grating on top of an AOQ waveguide as a function of grating height. The same period and filling factor are chosen as for the etched AOQ grating coupler investigated in Fig. 3.8: 1.05 μm and 50 %. We conclude that the coupling strength of the silicon grating on top of the alumina waveguide as a function of grating height follows the same curve as the coupling strength of the etched SOI grating as a function of grating depth. Henceforth, the silicon grating coupler on alumina can provide waveguide-to-fiber coupling efficiencies that are as high as conventional SOI grating couplers.

In Fig. 3.10, the coupling efficiency of a silicon grating coupler for the alumina-on-quartz waveguide platform is plotted as a function of wavelength.

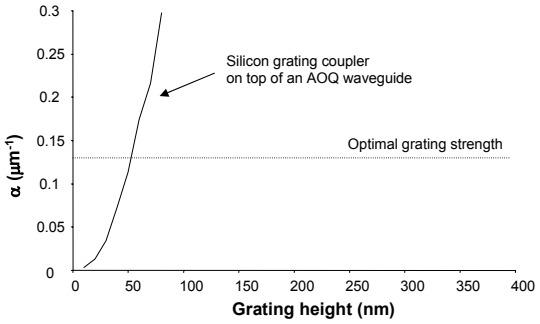

Figure 3.9: Calculated coupling strength of a silicon grating coupler on top of an alumina-on-quartz (AOQ) waveguide as a function of grating height.

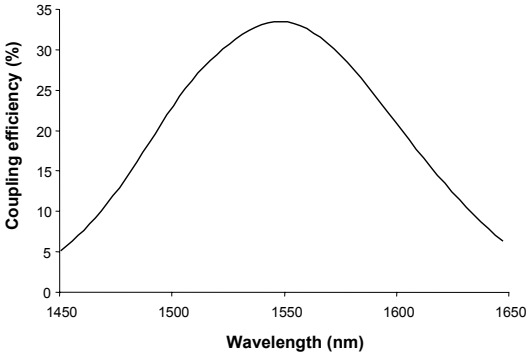

Figure 3.10: Coupling efficiency of a silicon grating coupler for the AOQ platform. Period = 1050 nm, filling factor = 50 %, height of silicon grating = 50 nm calculated by FDTD.

A coupling efficiency of 35 % and a 1 dB bandwidth of 60 nm is calculated using 1-D FDTD calculations. Silicon is not the only material that can be used to enhance the coupling strength of a grating and obtain efficient waveguide-to-fiber grating couplers. Other materials can be used as long as they provide a high enough refractive index contrast. In this work we will investigate the use of metals to provide this index contrast on top of SOI waveguides. This is the subject of the next chapter.

3.8 Conclusion

In this chapter, we reviewed the working principle, simulation and characterization of grating couplers and discussed the state-of-the-art. We introduced a novel method for coupling between a waveguide and a single mode fiber by placing a high-index contrast grating on top of the waveguide rather than etching into the waveguide. This idea allowed us to come up with a design for compact and efficient grating couplers for coupling between single-mode

fibers and low-index contrast waveguides, a component that has not yet been explored in the literature. In the next chapter, we will explore this extra degree of freedom further and investigate the use of metals for designing efficient grating couplers for silicon-on-insulator waveguides.

Bibliography

[1] D. Taillaert "Grating couplers as interface between optical fibers and nanophotonic waveguides" *PhD thesis* Ghent University, 2005.

[2] G. Roelkens "Heterogeneous III-V/Silicon Photonics: Bonding Technologies and Integrated Devices" *PhD thesis* Ghent University, 2007.

[3] J. Schrauwen, D. Van Thourhout, R. Baets "Focused-ion-beam fabricated vertical fiber couplers on silicon-on-insulator waveguides" *Appl. Phys. Lett.* 89 (14), 141102, 2006.

[4] P. Bienstman, R. Baets "Optical modeling of photonic crystals and VCSELs using eigenmode expansion and perfectly matched layers" *Opt. Quantum Electron.* 34(5), pp. 349-354, 2001.

[5] D. Taillaert, P. Bienstman, R. Baets "Compact efficient broadband grating coupler for silicon-on-insulator waveguides" *Opt. Lett.* 29(23), pp. 2749-2751, 2004.

[6] T. Claes "Metalen nanostructuren voor efficiënte en breedbandige koppeling van licht naar geïntegreerde optische circuits" *Master thesis*, Ghent University, 2006.

[7] http://www.epixnet.org

[8] F. Van Laere, G. Roelkens, J. Schrauwen, D. Taillaert, P. Dumon,W. Bogaerts, D. Van Thourhout, R. Baets "Compact and highly efficient grating couplers between optical fiber and nanophotonic waveguides in bonded InP-membranes" *IEEE Conference on Optical Fiber Communications (OFC)*, paper PDP15, OSA, 2006.

[9] G. Roelkens, D. Van Thourhout, R. Baets, R. Noetzel, M. Smit "High efficiency silicon-on-insulator grating coupler based on a poly-silicon overlay" *Opt. Express* 14(24), 11622, 2006.

[10] G. Roelkens, D. Van Thourhout, R. Baets "High efficiency grating couplers between silicon-on-insulator waveguides and perfectly vertical optical fibers" *Opt. Lett.* 32(11), pp. 1495-1497, 2007.

[11] D. Taillaert, H. Chong, P.I. Borel, L.H. Frandsen, R.M. De La Rue, R. Baets "A compact two-dimensional grating coupler used as a polarization splitter" *IEEE Photon. Technol. Lett.* 15(9), pp. 1249-1251, 2003.

[12] F. Van Laere, T. Claes, J. Schrauwen, S. Scheerlinck,W. Bogaerts, D. Taillaert, L. OFaolain, D. Van Thourhout, R. Baets "Compact Focusing Grating Couplers for Silicon-on-Insulator Integrated Circuits" *Photon. Technol. Lett.* 19(23), p.1919-1921, 2007.

[13] B. Wang, J. H. Jiang, G. P. Nordin "Embedded slanted grating for vertical coupling between fibers and silicon-on-insulator planar waveguides" *IEEE Photon. Technol. Lett.* 17(9), 1884-1886, 2005.

[14] G. Roelkens, D. Vermeulen, D. Van Thourhout, R. Baets, S. Brision, P. Lyan, P. Gautier, J.-M. Fedeli "High efficiency diffractive grating couplers for interfacing a single mode optical fiber with a nanophotonic silicon-on-insulator waveguide circuit" *Appl. Phys. Lett.* 92(13), 131101, 2008.

[15] J. Schrauwen, F. Van Laere, D. Van Thourhout, R. Baets "Focused-ion-beam fabrication of slanted grating couplers in silicon-on-insulator waveguides" *IEEE Photon. Technol. Lett.*, 19(11), p.816-818, 2007.

[16] Y. De Koninck, P. De Heyn, T. Meynen "Optische markers: IR-ID" *Verslag vakoverschrijdend project*, Ghent University, 2007.

[17] M. Verbist "Retroreflectieve optische marker-chips met individueel afgestemde filters" *Master Thesis*, Ghent University, 2008.

[18] K. De Vos, G. Girones, Y. De Koninck, P. Bienstman, E. Schacht, R. Baets "SOI biosensor platform based on arrayed microring resonators" *Unpublished*, 2008.

4
Metal grating coupler

A Metal grating coupler is a special type of grating coupler. The grating is made of metal and is deposited on top of the waveguide rather than etched into the waveguide. In this chapter, we will discuss the purpose and design of metal grating couplers on silicon-on-insulator. For the fabrication of metal grating couplers, we implement various methods discussed in chapter 2 and compare the experimental results.

4.1 Introduction

In this chapter, we introduce and investigate grating couplers made of metal. We present a theoretical study of these couplers for SOI waveguides and an experimental study whereby different fabrication methods are explored. Metals make up a significant fraction of the periodic table. Roughly spoken, a diagonal line drawn from boron (B) to polonium (Po) separates the metals at the left from the nonmetals at the right of the diagonal. Metals are well known for some specific macroscopic properties: most metals are shiny, ductile and conduct electricity, while most non-metals are not shiny, rather brittle and do not conduct electricity. We start this chapter with an introduction to the optical properties of metals.

4.2 Metals

4.2.1 Optical properties

The optical properties of metals originate from the response of the electrons in the metal to an optical field. As a first approximation, a metal can be considered as a linear, homogeneous and isotropic medium with a dielectric constant ϵ, a permeability μ and a conductivity σ. For such a material, Maxwell's equations can be written in the following form:

$$\begin{aligned} \nabla \cdot E &= 0 && (4.1)\\ \nabla \cdot H &= 0 && (4.2)\\ \nabla \times E + \mu \frac{\partial H}{\partial t} &= 0 && (4.3)\\ \nabla \times H - \epsilon \frac{\partial E}{\partial t} &= \sigma E && (4.4)\\ & && (4.5) \end{aligned}$$

By considering monochromatic light and assuming the plane wave solution to Maxwell's equations,

$$E = E_0 e^{j\omega t - j} \tag{4.6}$$

the wave equations for a metal can be written:

$$\nabla^2 E + \beta^2 E = 0 \qquad \text{where} \qquad \beta^2 = \omega^2 \mu (\epsilon + \frac{\sigma}{j\omega}). \tag{4.7}$$

These equations are identical to those of a non-conducting medium if a complex dielectric constant, $\epsilon' + j\epsilon'' = \epsilon + \frac{\sigma}{j\omega}$ is defined. We define a complex

refractive index, $n = n' + jn''$ so that $n^2 = \epsilon' + j\epsilon'' \equiv \epsilon$ where n'' is the extinction coefficient. Now the plane wave equation can be rewritten:

$$E = E_0 e^{\frac{-2\pi n'' z}{\lambda}} e^{(j\omega t - \frac{2\pi n z}{\lambda})}. \tag{4.8}$$

The second exponential of the plane wave equation is imaginary, corresponding to the oscillatory part of the wave. The first exponential is real and quantifies the absorption of the wave. When light is travelling through a metal, the effect of n'' is an exponential decay of the wave amplitude in the direction of propagation. As the power of the wave is proportional to the squared modulus of the electric field, the so-called absorption coefficient α is two times larger than the decay constant in the equation above:

$$\alpha = \frac{4\pi n''}{\lambda_0}, \tag{4.9}$$

The optical properties of metals distinguish from the optical properties of dielectrics because of the different atomic structure.

In a dielectric, electrons are tightly bound to the host atoms, whereas in a metal, electrons are very loosely bound to the atoms. A good description of a metal is the so-called free-electron model, in which the metal is described as a collection of ions that are fixed in space, and a gas of free conduction electrons that interact with themselves and with the ions through the Coulomb force [3]. The interacting system of ions and electrons is basically a plasma where the ions have much larger inertia than the electrons. When the plasma interacts with an electromagnetic field, the electrons will execute a forced oscillation relative to the ions. The amplitude and phase of this oscillation relative to the driving field will depend on its frequency relative to the eigen oscillation frequency of the plasma, ie. the plasma frequency ω_p. For gold, ω_p is about 10^{16} rad/s, which corresponds to a plasma wavelength of 137 nm, which is in the deep UV range.

The plasma oscillation is damped due to scattering effects. This is taken into account in the Drude model [4], which expresses the complex dielectric function as follows:

$$\epsilon = \epsilon_o(1 - \frac{\omega_p^2}{\omega(\omega + j\gamma)}), \tag{4.10}$$

where γ represents the collision rate of the electrons and determines the damping of the plasma oscillation. The Drude model is a simple and convenient model that explains some of the most fundamental properties of metals. Below the plasma frequency, ie. in the visible and infrared part of the spectrum, ϵ is negative and the incident electromagnetic radiation is back reflected by the plasma, penetrating into the metal only over a distance of the order

$\frac{\lambda}{2\pi\sqrt{|\epsilon'|}}$, which is about 20 nm in the case of gold at a wavelength of 1550 nm. The very high reflectivity is thereby directly related to the refractive index contrast between the metal and the air:

$$R = \frac{|n-1|^2}{|n+1|^2}. \tag{4.11}$$

Above the plasma frequency however, the real part of ϵ is positive and the metal becomes transparant. It is thus clear that the optical properties of metals are very dependent on the wavelength. Figure 4.1 plots experimentally determined complex dielectric constant and complex refractive index data of gold as a function of wavelength. In the telecom wavelength region, the dispersion is relatively weak and linearly dependent on the wavelength.

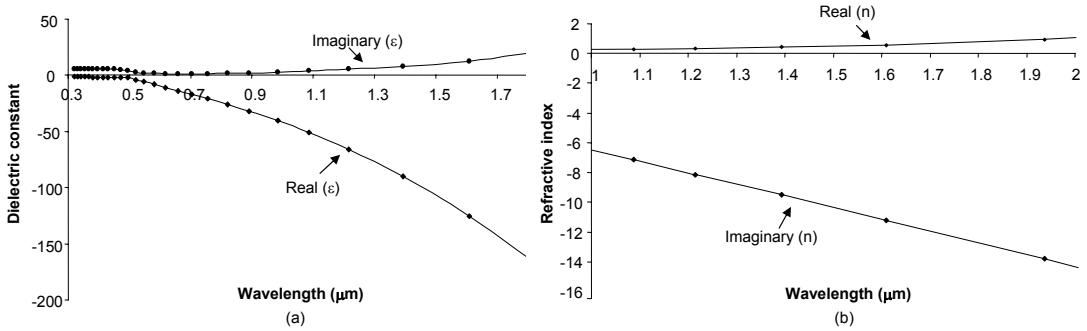

Figure 4.1: (a) Wavelength dependent dielectric constant of gold. (b) Wavelength dependent refractive index of gold in the infrared telecom region. Data retreived from [1]

We plotted the complex refractive index of a number of common metals and a number of dielectrics for comparison in Fig. 4.2. The plotting is done in the complex plane, representing the real and imaginary part of the refractive index at a wavelength of 1550 nm. The refractive index contrast between any two materials is defined as the distance between the points corresponding to the complex refractive index of the two materials.

4.2.2 Surface plasmons

In this section, we address a specific optical phenomenon typical for metals: surface plasmons.

A surface plasmon is a collective oscillation of the electron gas on the interface between a metal and a dielectric. Theoretically, surface plasmons simply arise as purely two-dimensional solutions of Maxwell's equations that propagates as a transverse magnetic (TM) wave with the following propagation

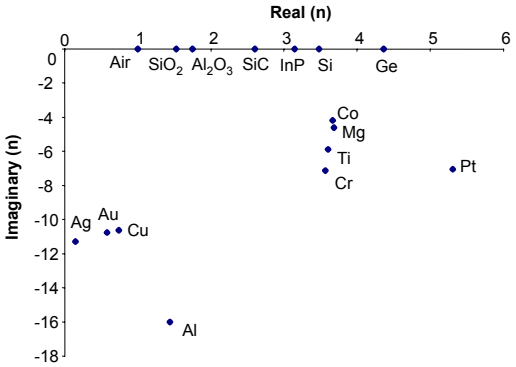

Figure 4.2: Real and imaginary part of the refractive index of various common materials at a wavelength of 1550 nm.

constant along the metal-dielectric interface (for a derivation of the dispersion relation from Maxwell's equation, see for instance [5]):

$$\beta_{sp} = \frac{\omega}{c}\sqrt{\frac{\epsilon_m \epsilon_d}{\epsilon_m + \epsilon_d}}, \tag{4.12}$$

with ϵ_m and ϵ_d the dielectric constants of the metal and the dielectric respectively. The surface plasmon mode has an evanescent tail in both the dielectric and the metal. This characteristic nature of surface plasmons follows from the requirement that the real parts of the dielectric constants ϵ' of the media on either side of the interface have opposite signs. This is the case above the frequency $\frac{\omega_p}{\sqrt{2}}$. The surface plasmon mode is confined to the metal-dielectric interface with a high intensity precisely at the interface of the metal (see Fig. 4.3 (a)). This fact makes this mode very sensitive to changes in the refractive index in the vicinity of the metal and is therefore very suitable to probe such interfaces. The excitation of surface plasmons is the principle behind surface plasmon resonance biosensing [6].

Surface plasmons are attenuated during propagation, basically due to dissipation in the metal. The propagation length of a surface plasmon is given by $L_{sp} = 1/2\beta''_{sp}$. For gold L_{sp} is about 250 μ at a wavelength of 1550 nm and less than a micron in the blue part of the visible spectrum. For a thin metal film, the situation is somewhat different. If the film is sufficiently thin, ie. ≤ 50 nm, the surface plasmon modes at the upper and lower interfaces interact, giving rise to symmetric and asymmetric modes. The asymmetric mode spreads well into the dielectric cladding and the energy density of the mode drops to zero in the metal [8]. As a result, this mode can propagate for a much longer distance than its symmetric counterpart and is called a long-range surface plasmon mode. The propagation length of long range surface plasmon modes can go up to several millimeters depending on the thickness of the metal layer.

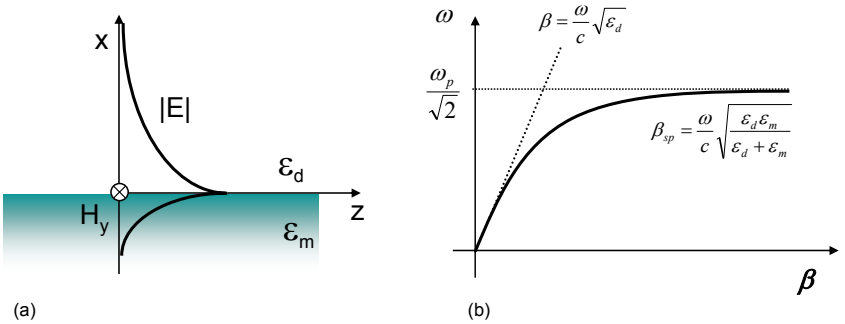

Figure 4.3: The surface plasmon. (a) Schematic of the characteristic field profile of a surface plasmon at a metal-dielectric interface. (b) Dispersion relation of a surface plasmon. The light line represents the dispersion relation of light in the dielectric medium.

Excitation of surface plasmons can be done using different schemes. From the position of the light line relative to the surface plasmon dispersion curve in Fig. 4.3 (b), it follows that a surface plasmon mode cannot be excited by simply shining light onto the metal. One approach to overcome the momentum mismatch is to excite surface plasmons using a prism coupler [9]. This scheme requires careful angular tuning of the setup [10]. Another approach is by using metal features like protrusions [11] or a grating structure [12]. End-fire coupling can also be used and is especially attractive for excitation of long range surface plasmons, given the high overlap integral between the long range surface plasmon mode and the gaussian mode of an optical fiber [7]. For further details and an experimental implementation of this coupling scheme we refer to [13].

Intra-chip excitation of surface plasmon modes is also possible and has been demonstrated on the SOI platform. A first approach is by placing the metal layer next to a silicon waveguide. Coupling occurs between the dielectric mode in the wire waveguide and the surface plasmon mode supported at the vertical edge of the metallic layer. The principle of this is directional coupling and works for TE polarization [14]. A second approach is by placing the metal layer on top of the silicon waveguide. Coupling occurs between the dielectric mode in the waveguide and the surface plasmon mode supported at the metal-silicon and metal-air interface. The principle of this is straightforward end-fire coupling and works for TM-polarization [15].

We note that intra-chip excitation of surface plasmons is a very interesting approach towards highly miniaturized and sensitive biosensors. In [15], a novel concept for an integrated biosensor is proposed based on a surface plasmon interferometer integrated in SOI. The key element of this biosensor is a gold layer embedded in a silicon waveguide over a length of about 10 μm. The gold layer is embedded in such a way that the fundamental dielectric mode in

the SOI waveguide is in cut-off so that the only two modes supported are the two surface plasmon modes, one at the upper interface of the gold layer and one at the bottom interface. When the two modes are excited, they interfere and the interference signal is coupled back into the SOI waveguide. This interferometer can sense very small differences in the refractive index at the upper gold interface, which makes it an interesting candidate for a biosensor.

In this work, we do not aim for the excitation of surface plasmon modes. Instead, we make use of a metal to induce a periodic perturbation of dielectric SOI waveguides in order to couple to dielectric SOI modes. In particular, we concentrate on TE polarization, as this is the most interesting polarization for nanophotonic circuits [16]. In this polarization the magnetic field is oriented normal to the waveguide and so does not couple to TM-polarized surface plasmon modes at the interfaces.

4.3 Metal grating couplers for Silicon-on-Insulator circuits

4.3.1 Rationale

Metals are generally avoided in integrated optics because of their intrinsic property to absorb electromagnetic radiation. Consequently, the implementation of optical functions based on metallic components in dielectric waveguide platforms such as SOI remains rather unexploited. Nevertheless, metals are widely used for the implementation of other non-optical functions. Metals are good conductors and thus provide an ideal platform for applying voltages and currents for use as electrodes and electrical interconnections. Metals heat up when a current goes through them, which is interesting for implementing thermal elements. Metals distinguish from other materials by their dense atomic packing which is interesting for defining biomolecular binding sites for sensing applications via controlled adsorption of molecules. Metals are also interesting from a fabricational point of view. They are relatively easy to define and structure. Depending on the type of metal, they can be deposited by resistive Joule-evaporation, localized electron-beam evaporation or plasma sputtering and can be structured by various techniques including lift-off techniques and etching techniques or CMOS compatible techniques such as Chemical Mechanical Polishing (CMP).

In this chapter, we exploit the very high refractive index contrasts provided by metals to implement a very generic optical function: coupling of light. The reasons to investigate metal grating couplers are the following. First of all, metal gratings are relatively easy to fabricate. The fact that the grating can be deposited rather than etched is an advantage. Etching over a predefined depth

is a difficult task that requires accurate control of the etching conditions by process optimization. In case of metal deposition, process conditions are much less critical and still well controllable. Second, the metal grating coupler offers a flexibly means of defining an optical access point to an integrated photonic circuit after the fabrication of the circuit itself. This is especially interesting in a research environment, where fabrication may suffer from a rather low yield. The use of a metal grating coupler allows to define the position of the coupler after circuit fabrication in a post-processing step at a point in the circuit best suited for experimental validation. An example of the fabrication of gold grating couplers in a post-processing scheme can be found in reference [18]. And finally third, by using a metal, the optical coupling function of the metal grating coupler can be combined with one or more non-optical functions such as an electric function.

In reference [19] a metal grating on top of a dielectric waveguide has been described for optical coupling whereby the individual metal grating fingers are used as electrode fingers. The waveguide modes are in fact surface plasmon modes supported by the metal-dielectric waveguide interface. By applying voltages the local refractive index of the dielectric is changed via the free-carrier plasma effect and the coupling efficiency can be altered for use as a light modulator. In our work however, we focused on the excitation of dielectric modes supported by the waveguide rather than on surface plasmon modes supported at the interfaces. Also for this application, the combination of electric and optical functions is of high interest. One example currently investigated is a light emitting diode based on semiconductor quantum dot nanocrystals. A schematic is shown in Fig. 4.4 [20]. The nanocrystals are dispersed in a conducting polymer film sandwidched between a silicon-on-insulator waveguide containing a metal grating coupler serving as the first electrode and a top gold layer serving as the second electrode at a distance of a few 100 nm above the grating. By applying a voltage between the two electrodes a well-distributed electric field will be built up over the polymer layer. This will excite the quantum dots and stimulate the emission of photons in the telecom region, which can be coupled in directly to the silicon waveguide by means of the metal grating coupler.

4.3.2 Design and simulation methods

In the previous chapter simulation methods based on eigenmode expansion and finite difference time domain calculations were introduced and numerical stability issues were put forward. For lossy materials such as metals, electromagnetic fields penetrate only weakly into structures made of metal. The result is that the eigenmodes in a slab that contains metals have rather abrupt features. To deal with this type of structures to calculate the eigenmodes, a

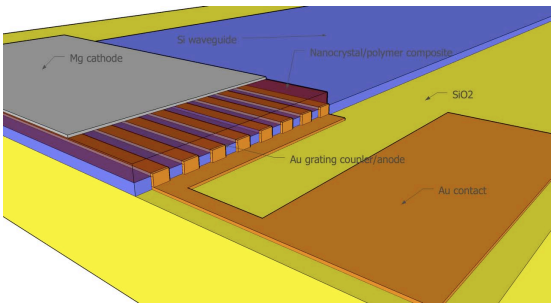

Figure 4.4: Schematic of a quantum dot light emitting diode based on a metal grating coupler serving as one of the electrodes.

solver has been incorporated into CAMFR - the so-called series solver - which calculates the eigenmodes in two steps. First, estimates of the modes are calculated based on a plane wave expansion using M modes and next, these estimates are refined using the full dispersion relations. The value of M is an extra parameter in the parameter space that further contains the number of modes N, the PML thickness and the distance d from the waveguide to the edge of the computational domain. All should be chosen adequately to obtain numerically stable results. For most cases, we found numerically stable results for N=130, M=3, PML=-0.3 μm and d=9 μm. The accuracy of these results was verified by comparison with FDTD calculations and we found agreement within 1 %. Unlike with CAMFR, in FDTD calculations it is not possible to take dispersion into account. We will come back to the dispersion issue further on.

4.3.3 Coupling efficiency

In the previous chapter, the concept of a grating for coupling between a fiber and a waveguide was introduced. This grating was defined by etching. Here we study grating couplers made of metal and deposited on top of the waveguide. We use CAMFR to calculate the power that is diffracted upward P_{up} upon incidence of the fundamental waveguide mode. A scheme of the simulation lay-out and a definition of the grating parameters is found in Fig. 4.5. All simulations are run with the assumption that the grating is used with an index matching fluid between the grating and the fiber facet, unless otherwise stated. We do this for two reasons: (1) in the absence of reflections at the fiber facet, the highest coupling efficiency can be achieved and (2) it is the most likely configuration in a packaged system. The influence of the refractive index of the top cladding will be discussed.

Metals are lossy and so will be metal grating couplers. We will show however that despite of the absorption losses, metal grating couplers provide surprisingly high coupling efficiencies when designed in an appropriate way. To assess the absorption loss, it is calculated from the reflection R, the transmis-

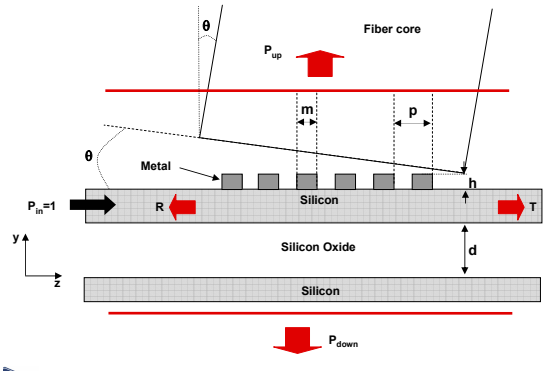

Figure 4.5: Layout of a metal grating coupler simulation. Grating parameters are period p, filling factor ff=$\frac{m}{p}$ and height h. Refractive index values of the SOI layer stack are $n_{silicon} = 3.476$, $n_{oxide} = 1.444$, $n_{cladding} = n_{fiber} = 1.46$. Number of grating teeth = 20.

sion T, the upward diffracted power P_{up} and the downward diffracted power P_{down} extracted from the simulations:

$$Loss = 1 - R - T - P_{up} - P_{down}. \tag{4.13}$$

From Bragg's condition, it follows that a grating of period $\frac{\lambda_o}{n_{eff}}$ will lead to vertical coupling. For an SOI waveguide with a fiber index matched top cladding, the effective index of the TE polarized fundamental mode is $n_{eff} = 2.8424$, which results into a grating period of 550 nm. This is merely an estimate. As mentioned in the previous chapter, simulations are required to find a more accurate value. Figure 4.6 plots the reflection as well as the upward and downward diffracted power for a gold grating of height 50 nm and with a filling factor of 50 % in a two-dimensional parameter space at a wavelength of 1550 nm. The x-parameter is the period of the grating, the y-parameter is the buried oxide layer thickness of the SOI layer stack. The number of grating periods is 20.

From the intensity values of the diffracted power it follows that the refractive index modulation induced by the gold on top of the silicon is indeed sufficiently strong for the light in the waveguide to get diffracted. As expected, very large reflections are calculated for periods corresponding to a second order grating (second diffraction order reflects back into the waveguide; $p = \frac{\lambda_o}{n_{eff}}$; indicator point A on Fig. 4.6) and a third order grating (third diffraction order reflects back into the waveguide; $p = \frac{3\lambda_o}{2n_{eff}}$; indicator point B on Fig. 4.6). For the second order grating, the first order is diffracted vertically but with moderate intensity. For periods in between, reflections are very low: below 5 % and even below 0.05 % for periods of about 0.7 μm. For those periods, the power diffracted upward and downward reaches values between 13 % and 65 % depending on the buried oxide layer thickness.

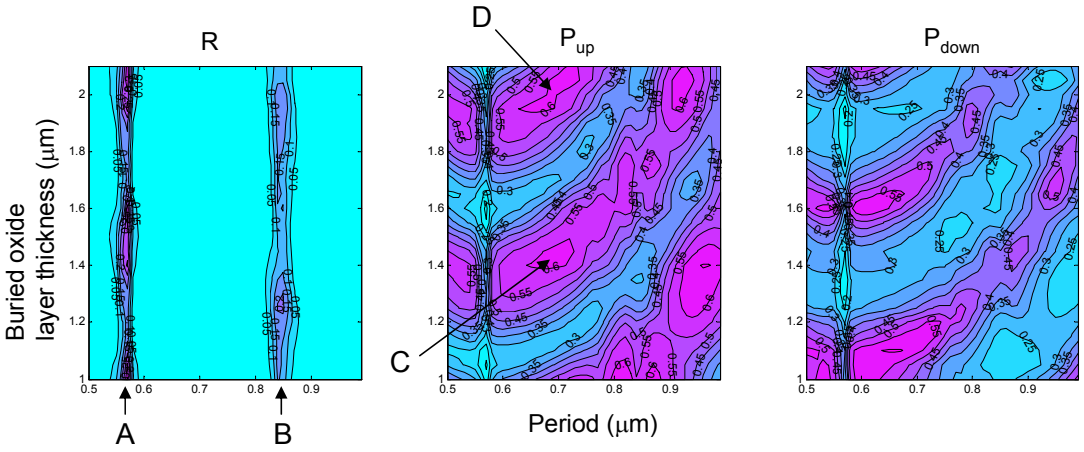

Figure 4.6: Reflected and upward and downward diffracted power fraction for a gold grating of height 50 nm and filling factor 50 % on SOI waveguide.

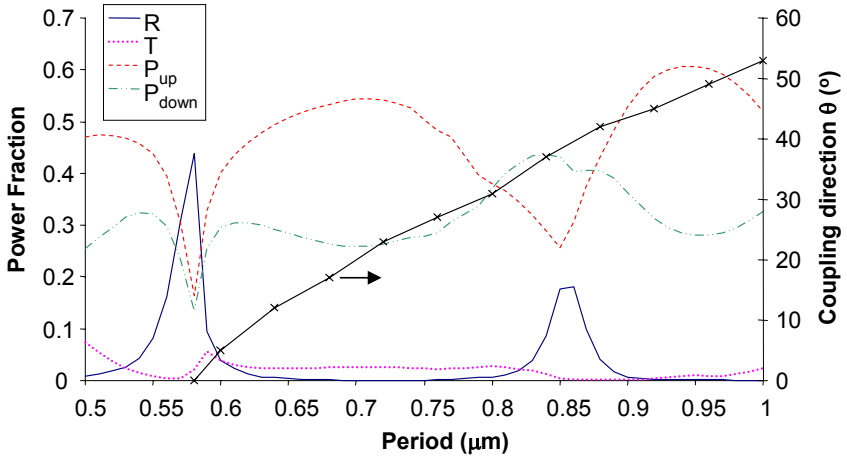

Figure 4.7: Power distribution by a gold grating of height 50 nm and filling factor 50 % on SOI waveguide with a fiber index matched top cladding.

The period of the grating determines the angle of diffraction which defines the fiber orientation θ with respect to the vertical. For a buried oxide layer thickness of 2 μm (indicator point C on Fig. 4.6) the reflection, transmission and upward and downward diffracted power is plotted together with the coupling direction in Fig. 4.7 for an index-matched top cladding and in Fig. 4.8 for air as top cladding.

The buried oxide layer thickness determines the intensity of the diffraction. This can be explained as follows. When a guided mode enters the grating zone the grating coupler diffracts light in the upward direction as well as in the

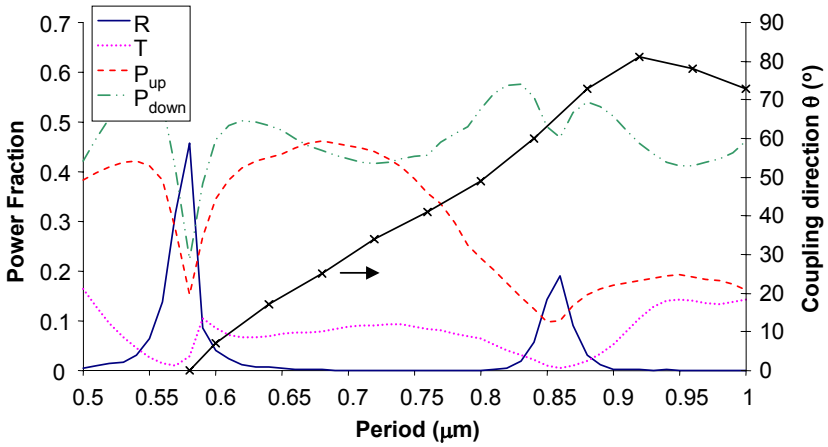

Figure 4.8: Power distribution by a gold grating of height 50 nm and filling factor 50 % on SOI waveguide with an air top cladding.

downward direction, thus creating an upward propagating and a downward propagating wave with the direction of propagation θ defined by the grating period. The downward propagating wave partially reflects at the oxide-substrate interface and becomes an upward propagating wave of slightly lower amplitude which will interfere with the original upward propagating wave. For a given buried oxide layer thickness d constructive interference will occur for those grating periods for which the phase condition for constructive interference is met:

$$2kd\cos[\theta(p)] = m2\pi. \tag{4.14}$$

This explains the periodic behaviour of the diffracted power as a function of buried oxide layer thickness. Maximal upward coupling (constructive interference in the upward direction) is accompanied by minimal downward coupling (destructive interference in the downward direction) and vice versa. By including a top and/or a bottom mirror, the maximal power in the upward or downward direction can be greatly enhanced as all the power can be reflected by the mirror and directed into one of both directions. With such a mirror the coupling efficiency for uniform gratings can be up to 80 %. For further details we refer to section 3.5. This approach is possible in combination with metal grating couplers too, but will not be further discussed in this work.

For the design of a grating coupler Figure 4.6 illustrates the importance of working with appropriately chosen parameters for the SOI layer stack. For near-to-vertical coupling and avoiding high reflections back into the waveguide, a period of about 0.7 μm seems optimal. For this period, a buried oxide layer thickness of 1.4 μm (indicator point C on Fig. 4.6) or 2 μm (indicator point D on Fig. 4.6) for upward coupling is optimal. Note that a maximum in the

upward coupling corresponds to a minimum in downward coupling and vice versa. We read from Fig. 4.7 that the optimal angle of diffraction for optimal coupling is 20 ^{o}.

Let us now focus on the absorption losses and the coupling efficiency of different metal grating couplers. For a grating period of 680 nm, P_{up} and $Loss$ are plotted at a wavelength of 1550 nm in a two-dimensional parameter space. The x-parameter is the filling factor of the grating and the y-parameter is the height of the grating. The calculations are presented for a gold grating and a silver grating in Fig. 4.9 and for a platina and titanium grating in Fig. 4.10. As a comparison, we add P_{up} of a standard etched SOI grating coupler in Fig. 4.11 (a) and of a silicon grating coupler consisting of a silicon grating on top of the silicon waveguide in Fig. 4.11 (b). In this figure, the etch depth of the grating and the height of the silicon grating are taken as the y-parameter respectively. We note that it is difficult to achieve full numeric stability over the scanned parameter space which explains the discontinuities in the figures. However, the numeric stability is sufficient to interpret the results. The filling factor is scanned between 0.05 and 1 and the height/etch depth is scanned between 5 nm and 200 nm.

The height and the filling factor of the metal grating seem of great influence on the distribution of the power. The directionality of an etched SOI grating coupler reaches maximum values for etch depth values of about 70 nm and filling factor values of about 0.5. This is in agreement with simulation and experimental results reported in reference [21]. The profiles of the etched silicon grating and the silicon grating on top seem to be divided into two parts. This is because strong second order Bragg reflections occur for certain combinations of the grating etch depth/height and filling factor.

The directionality of a metal grating coupler depends on the type of metal. For gold and silver, they reach maximum values for grating height values of only 20-40 nm (see Fig. 4.9). Unlike SOI gratings, filling factors less than 0.5 are preferable with an optimum of about 0.3. For gold or silver grating couplers reflections take place, but they are very low for filling factors below 0.5 (less than 2 %). They become higher for higher filling factors but stay well below 10 %.

Compared to the directionality profile of SOI grating couplers in Fig. 4.11, the maximum in the profile of gold and silver grating couplers in Fig. 4.9 is shifted towards the bottom. In other words, for the same height of the grating on top of the silicon waveguide, the upward diffracted power is higher for a metal grating than for a silicon grating. This can be explained by the refractive index difference. The index contrast is much higher in the case of a metal than in the case of silicon. Therefore, the strength of the grating and thus the diffracted power is higher for smaller grating teeth.

This holds for gold and silver gratings but does not explain the behaviour of platina and titanium gratings. Where the influence of absorption losses

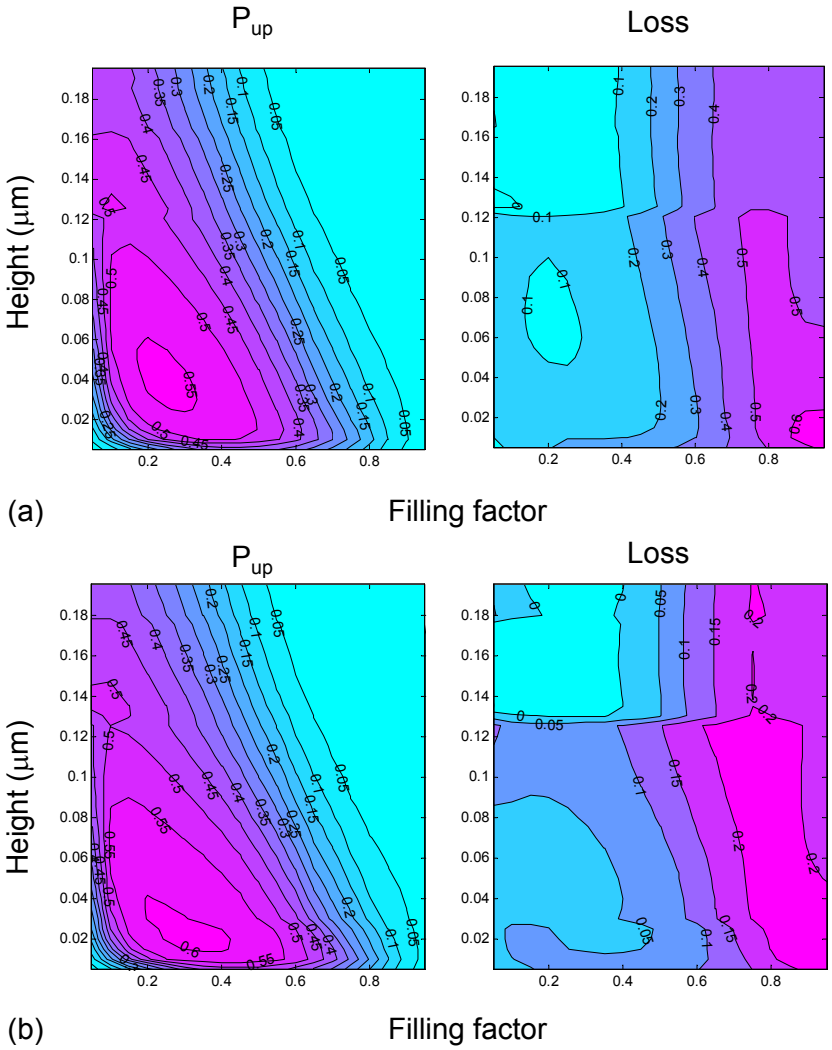

Figure 4.9: Directionality profile and loss profile of a metal grating coupler of period 680 nm. The metal is (a) gold and (b) silver.

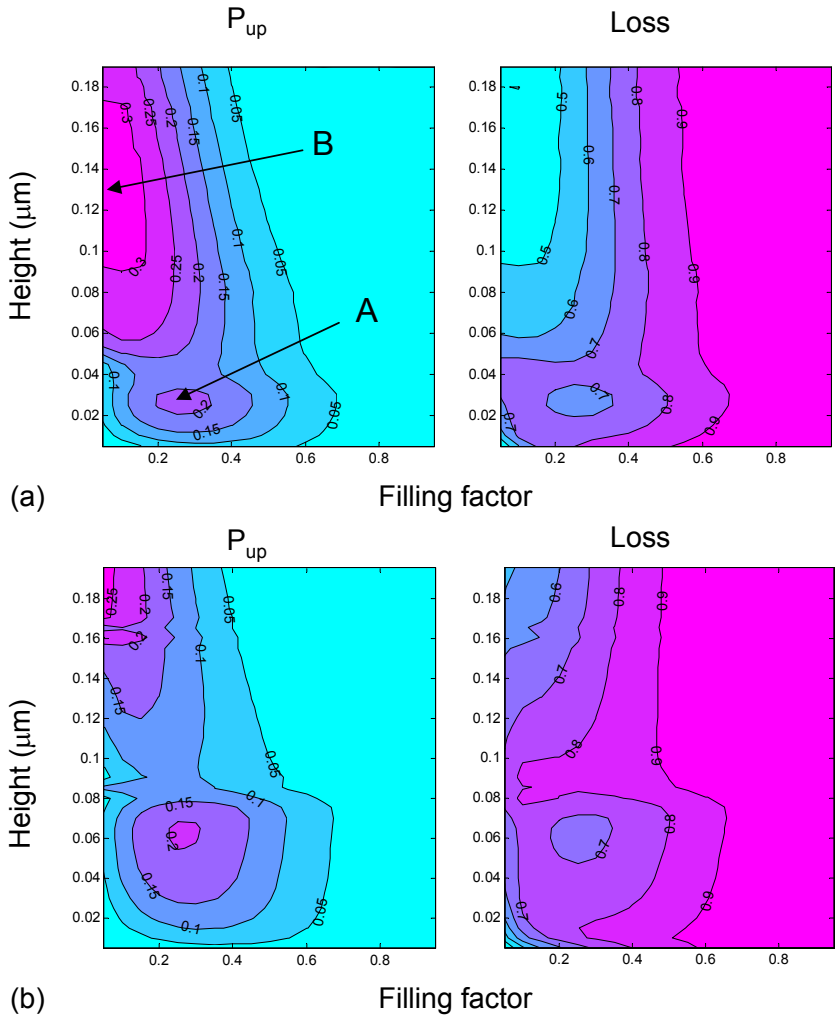

Figure 4.10: Directionality profile and loss profile of a metal grating coupler of period 680 nm. The metal is (a) platina and (b) titanium.

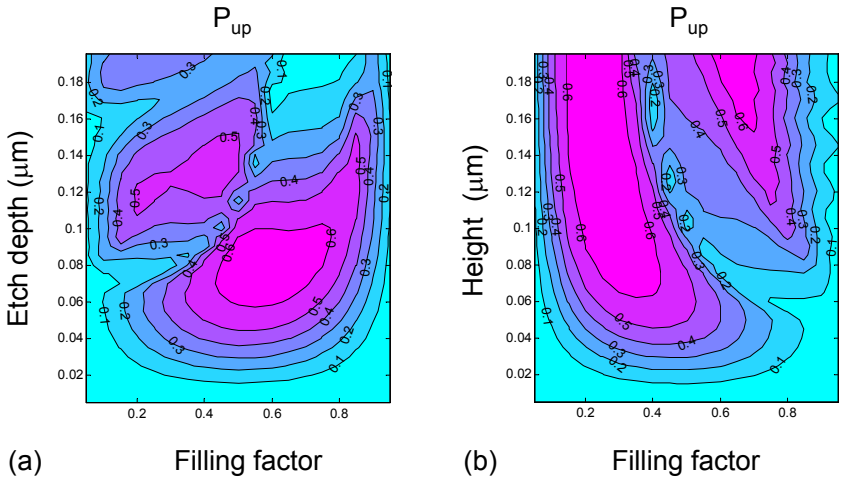

Figure 4.11: Directionality profile of (a) a standard etched SOI grating coupler of period 680 nm and (b) a silicon grating coupler consisting of a silicon grating on top of the SOI waveguide.

plays only a minor role for noble metals such as gold and silver gratings, they become crucial for other metals like platina and titanium. As for silicon, gold and silver, we expect a maximum for small grating teeth (indicator point A in Fig. 4.10 (a)). Nevertheless, we observe only a local maximum. A global maximum is found for extremely low filling factors and much higher grating heights (indicator point B in Fig. 4.10 (a)). The same is true for the directionality profile of the titanium grating coupler in Fig. Fig. 4.10 (b). This is caused by absorption losses. For a silicon grating, there is no absorption loss, whereas for a metal grating, the loss increases almost linearly with increasing filling factor (see Fig. 4.9 (c) and Fig. 4.10 (c)) and are much higher in absolute values for gold and silver than for platina and titanium. These metals are so lossy that the competition between diffraction and absorption loss cannot be won at a filling factor of about 0.3 and lower filling factors are needed to obtain the high directinality. Although directionality values are lower than for SOI gratings or gold and silver gratings, the coupling might be of value for some applications.

We used CAMFR and the procedure outlined above to find optimal grating parameters of a number of metal grating couplers on top of SOI waveguides for optimal coupling to a single-mode fiber at a wavelength of 1550 nm ($\pm$ 10 nm). Then, the optimal fiber orientation was calculated and the waveguide-to-fiber coupling efficiency was assessed by FDTD simulations. We plotted the result for a gold and a platina grating coupler in Fig. 4.12. For all gratings, the 1dB bandwidth is about 40 nm. As expected the gold grating is much more efficient because it is less lossy than the platina grating. Roughly, half of the efficiency is reached with a platina grating coupler.

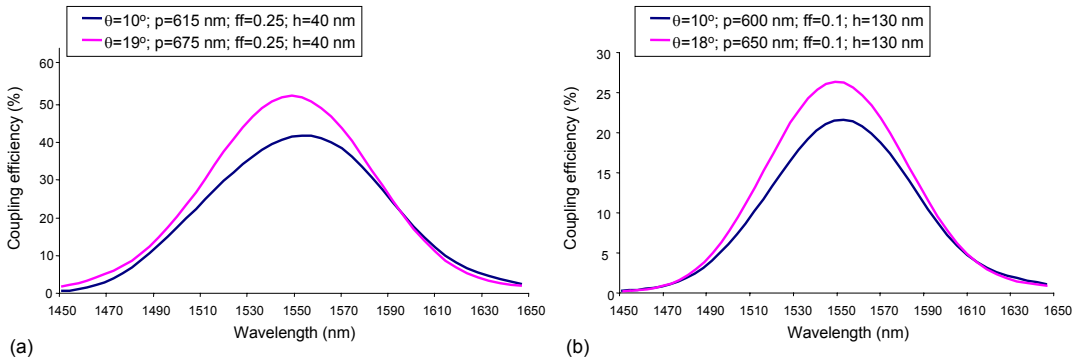

Figure 4.12: Waveguide-to-fiber coupling efficiency of metal grating couplers with optimal grating parameters and fiber orientations, calculated by FDTD. (a) Gold grating, (b) platina grating.

For a number of other grating couplers made of common metals on top of an SOI waveguide the results of the calculations are summarized in table 4.1. Optimal grating parameters of an SOI grating coupler defined by etching and of a silicon grating couplers consisting of a silicon grating on top of an SOI waveguide are added for comparison. The grating parameters were found by the procedure outlined in this section using CAMFR. The coupling efficiency was calculated with FDTD. Index-matching gel was assumed between the grating and the fiber.

Material	n_{metal}	p (nm)	ff	h (nm)	θ^o	η (%)
Ag	0.15-11.30j	685	0.3	20	20	57
Au	0.58-10.75j	675	0.25	40	19	53
Cu	0.72-10.65j	670	0.25	40	19	49
Al	1.45-15.96j	690	0.2	30	20	48
Pt	5.31-7.04j	680	0.1	130	18	27
Ti	3.69-4.62j	680	0.1	160	22	23
Si	3.476	680	0.3	80	25	56
SOI	-	660	0.6	80	14	57

Table 4.1: Grating parameters for optimal coupling to a single-mode optical fiber in TE polarization using index matching fluid between grating and fiber.

In conclusion, for an SOI layer stack with a buried oxide layer thickness of 2 μm the optimal fiber orientation is about 20 degrees for metal grating couplers. Other fiber orientations may be desired that are less off-vertical, for instance for the design of two-dimensional gratings used for polarization splitting [21]. Also for packaging purposes (see chapter 5) and testing set-ups (see chapter 6), diffraction closer to the vertical is more advantageous. We note that silicon as

well as metal gratings can be designed such that coupling is obtained towards the downward direction. This is coupling through the substrate and can be of interest for certain applications.

All the calculations presented in this section were done for a single wavelength. However, we mentioned earlier that the refractive index of a metal highly depends on the wavelength. However, although the refractive index of a metal is highly dependent on the wavelength, the refractive index contrast will change by only a few percent. As a result the coupling efficiency as a function of wavelength will vary only within 0.1 %. For this is the reason why the wavelength dependence of the refractive index can be neglected when designing metal grating couplers.

As we will see, some fabrication techniques and material issues require the use of a buffer layer between the waveguide and the metal. Two types of buffer layers will be used: titanium to increase the adhesion between silicon and gold and alumina to protect the silicon from ion damage during the FIB process. In general, when the distance between the grating and the waveguide is increased, the coupling efficiency becomes lower as the grating strength decreases, regardless of the material used as a buffer layer. When a dielectric is used such as alumina, the coupling efficiency decreases exponentially with increasing buffer layer thickness. However, when a metal is used such as titanium, the penalty is higher because of absorption losses.

4.4 Fabrication and measurements

In the following, we present our experimental work. Of the metal grating couplers designed in the previous section, we chose to fabricate gold grating fiber-to-waveguide couplers. We aimed at near-to-vertical coupling with a 10^o offset with respect to the vertical. We exploited different techniques for the fabrication of gold grating couplers: focused ion beam (FIB) milling, e-beam lithography and nanoimprint lithography. The coupling efficiency of the fabricated grating couplers was experimentally determined by fiber-to-fiber measurements using the vertical measurement setup with the fibers mounted at 10^o with respect to the vertical. The fiber-to-waveguide coupling efficiency was found by taking the square root of the measured data. This is of course an approximation and only valid when both gratings are identical. SEM inspection of pairs of gratings revealed intra-chip non-uniformity of the FIB and e-beam lithography processes that were developed. The main reason for that is different milling/writing conditions on different spots on the sample causing focusing errors of the ion/electron beam. Moreover, alignment of the gratings was done manually causing grating lines that are not perfectly perpendicular to the waveguide axes. Nevertheless, we obtained good agreement with simulation results.

4.4.1 Focused ion beam milling

Gold grating couplers were fabricated on top of 10 μm broad shallowly etched rib waveguides defined in an SOI layer stack containing a 1 μm thick buried oxide layer. The process flow is depicted in Fig 4.13. First, gold layers were defined on top of the waveguides by image reversal photolithography and lift-off. Thickness of the gold was 40 nm. Next, the grating with a period of 620 nm was defined by FIB milling with a 30 keV Focused Ion Beam (FIB) of Gallium$^+$-ions with a beam current of 50 pA. Two such gratings were defined on the waveguide separated by about 5 mm. Etching was done in Enhanced Etch mode meaning that during the etching, I_2 was delivered through a needle close to the beam spot.

In the absence of gold I_2 molecules are adsorbed on the Si surface which facilitates the extraction of Si atoms from the collision cascade caused by the ion bombardment by the formation of volatile species. As a result, smaller doses are needed and less ion damage is generated. In the presence of gold the process will be more complicated but we expect that this principle holds and that ion implantation will be limited to a certain extent by working in a I_2 environment. The result of the FIB milling process is depicted in Fig. 4.14: the grating is well defined but the etching could not be limited to the thin gold layer, even with very low ion beam doses. Given that gold is very easily and rapidly etched by the focused ion beam, etching and amorphization of the underlying silicon could not be avoided. This was experimentally proven by the measurement data depicted in Fig. 4.16 (a), indicating a clear influence of the ion beam exposure dose on the coupling effiency. For that reason these grating couplers did not perform well. Even the best fabricated grating with period of 620 nm and filling factor of 40 % demonstrated a coupling effiency of hardly 5 % whereas for this grating 20 % is expected from FDTD-simulations.

Given the problem of ion penetration into the silicon when etching the gold layer, a second generation of gold grating couplers was fabricated with an alumina (Al_2O_3) buffer layer between the gold and the waveguide. A 50 nm thick alumina layer was found to sufficiently protect the silicon from implantation Gallium$^+$-ions accelerated by an electron voltage of 30 keV [22]. Moreover, its etch rate is much lower than the etch rate of silicon. The alumina layer was deposited by e-beam evaporation prior to gold layer deposition and grating definition. The complete process flow is depicted in Fig. 4.13. The result of FIB milling with an alumina buffer layer is shown in Fig. 4.15. In this case, no etchant gas was used. Comparison with Fig. 4.14 learns that the alumina buffer layer seems to provide an effective etch stop layer. No etching damage could be determined by SEM inspection. This was confirmed by optical characterization of the gratings showing no dependence of the ion beam exposure dose on the coupling efficiency. The best fabricated grating coupler had a period of 600 nm and filling factor of 40 % and demonstrated a coupling ef-

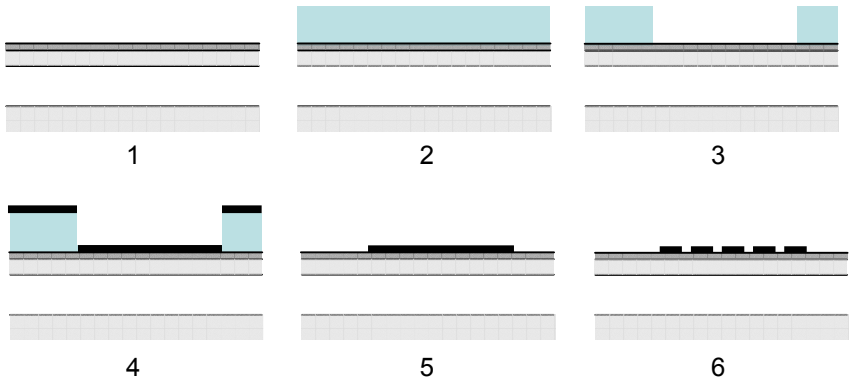

Figure 4.13: Gold grating fabrication on SOI waveguides by FIB: (1) Alumina deposition, (2) Resist spinning, (3) Lithography and development of the resist, (4) gold evaporation, (5) lift-off and (6) FIB milling.

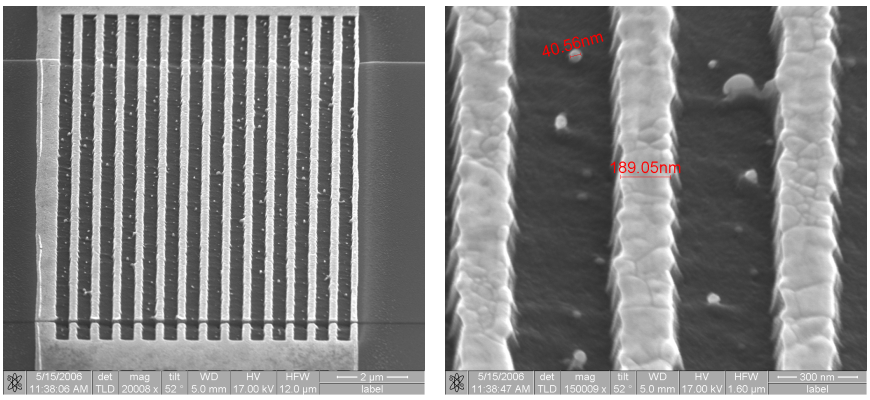

Figure 4.14: FIB milling of a gold grating directly on top of an SOI waveguide layer.

ficiency of over 13 %. The experimental results are in excellent agreement to simulation results.

We note that the alumina buffer layer between the silicon waveguide and the gold grating lowers the theoretical coupling efficiency. However, the ion implantation damage has such a detriminal effect that avoiding it by adding the buffer layer is more beneficial.

4.4.2 Nanoimprint and lift-off

To assess the influence of the metal grating filling factor on the performance of the grating coupler, double UV-NIL was used to define gratings with varying grating parameters on a bare SOI chip. For this purpose a master mold was ordered via the silicon platform containing 220 nm deep gratings with periods of 610, 620, 630 and 640 nm, varying filling factors roughly between 20% and

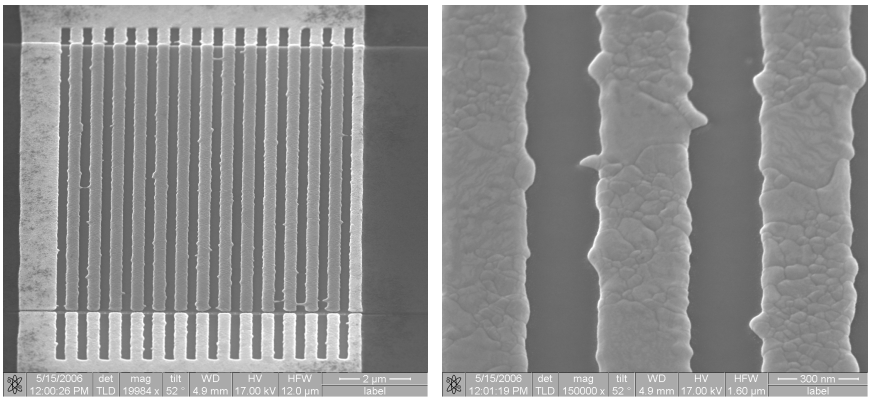

Figure 4.15: FIB milling of a gold grating on top of an SOI waveguide with Al_2O_3 buffer layer between the silicon and the gold.

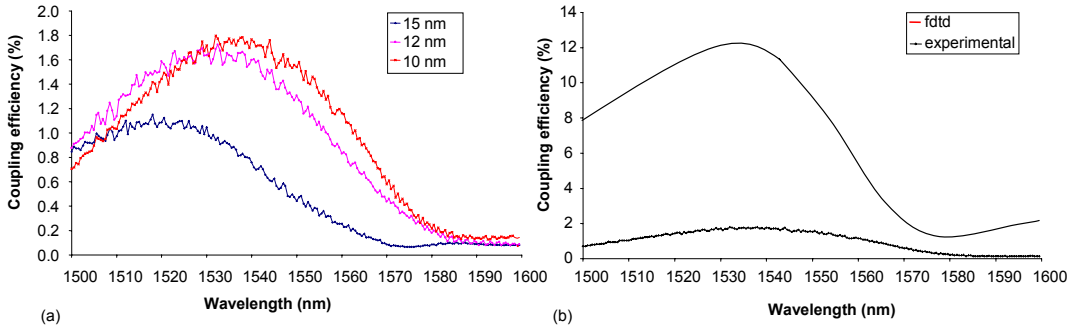

Figure 4.16: Experimentally determined fiber-to-waveguide coupling efficiency of FIB fabricated gold grating couplers directly on top of silicon. (a) Coupling efficiencies of gold gratings with period of 600 nm and height 50 nm as a function of ion beam exposure dose. (b) Coupling efficiency of a gold grating with period = 600 nm, filling factor = 50 %, grating height = 50 nm. The buried oxide layer thickness is 1 μm. FDTD simulation results are added for comparison.

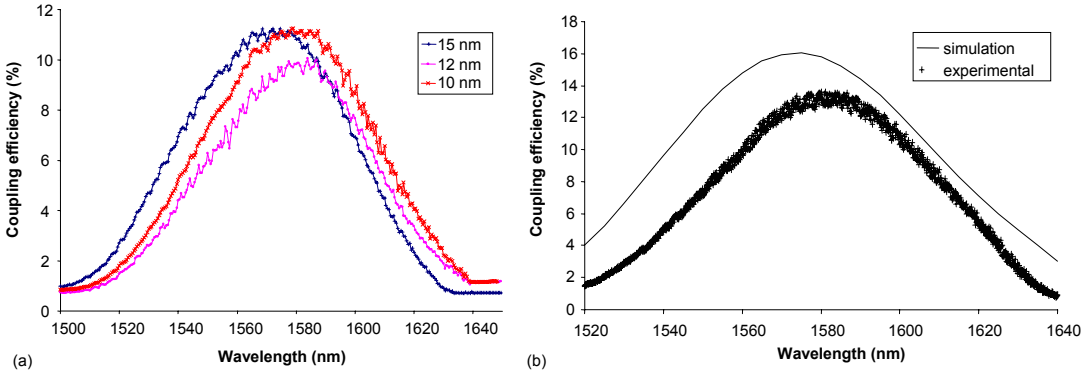

Figure 4.17: Experimentally determined fiber-to-waveguide coupling efficiency of FIB fabricated gold grating couplers on top of an alumina buffer layer between silicon and gold. (a) Coupling efficiencies of gold gratings with period of 580 nm and height 50 nm as a function of ion beam exposure dose. (b) Coupling efficiency of a gold grating with period = 580 nm, filling factor = 50 %, grating height = 50 nm. The buried oxide layer thickness is 1 μm. FDTD simulation results are added for comparison.

80 % and with distances between the gratings ranging from 200 μm up to 1000 μm. From the master, a UV-transparant mold was fabricated according to the technique described in section 2.3.6.1. This mold was then used for imprinting the grating structures in J-resist using the MA-6 Mask Aligner as the imprint tool. A 20 nm thin gold layer was deposited by evaporation prior to lift-off in acetone. The SEM pictures in Fig. 4.18 depict an overview and a detailed view of the fabricated gold gratings.

These gold grating couplers were not fabricated on top of silicon waveguides but on top of bare SOI substrates containing a silicon slab waveguide. These samples allowed to study experimentally the influence of the grating filling factor on the coupling efficiency. For an input power of 0.8 mW delivered by the input fiber, the power fraction (in %) captured by the output fiber is plotted in Fig. 4.19 (a). Each set of two grating couplers consists of two identical gratings with the same filling factor. The distance between the two grating couplers is the same for each set, i.e. 200 μm. We conclude that higher filling factors result into a lower coupling efficiency combined with a spectral shift. The relative change in coupling effiency and spectral position of the maximum is in quantitative agreement to simulation results.

Once the light is coupled into the SOI slab waveguide via the grating, it is diffracted in the waveguide plane. Consequently, only a fraction of the input power is coupled out by the second grating. The highest fiber-to-fiber coupling effiency is obtained for two gratings with a distance of 175 μm.

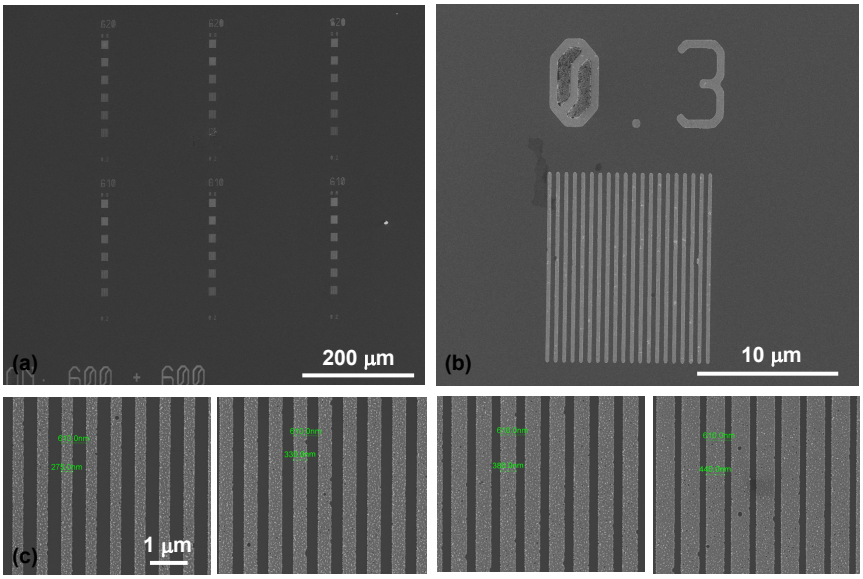

Figure 4.18: Gold gratings defined on a bare SOI substrate by nanoimprint and lift-off. (a) Overview, (b) single grating and (c) detail of the gratings with period of 610 nm and filling factors of 45, 55, 60 and 70%.

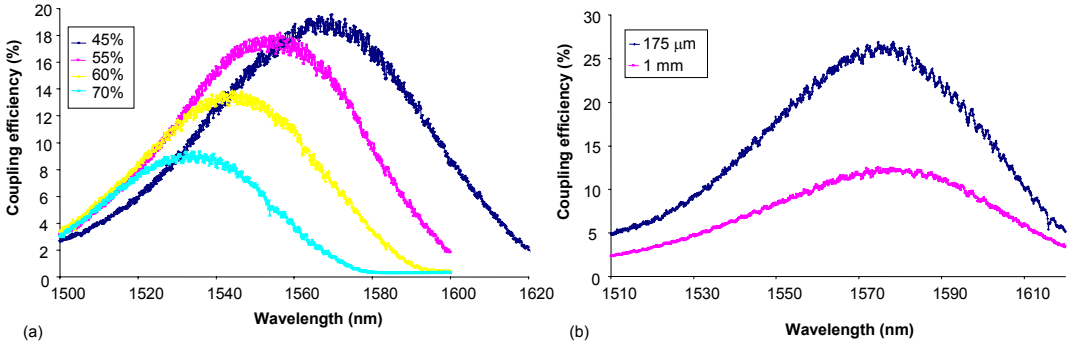

Figure 4.19: Experimentally determined fiber-to-waveguide coupling efficiency of nanoimprint fabricated gold grating couplers. (a) Output power as a function of wavelength of four sets of gold grating couplers with varying grating filling factors. Period = 610 nm, grating height = 20 nm, number of periods = 20. (b) Output power for two sets of gratings separated by 175 µm and 1000 µm. The buried oxide layer thickness is 2 µm.

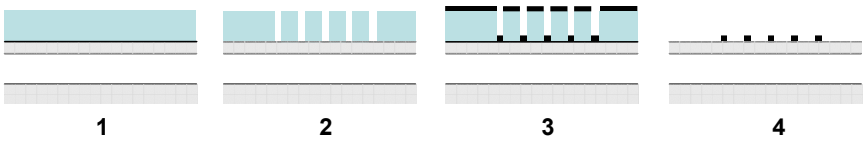

Figure 4.20: Gold grating fabrication on SOI waveguides by e-beam lithography: (1) resist spinning, (2) e-beam writing and development, (3) gold evaporation, (4) lift-off.

4.4.3 Electron beam lithography

Gold gratings were fabricated by e-beam lithography and lift-off. For these devices, an SOI layer stack was chosen with 2 μm of oxide. For the e-beam lithography, we worked with two SOI samples containing 220 nm x 10 μm waveguides. They were cleaned and shortly dipped into a buffered HF solution to remove native oxide on the silicon structures. On one of the samples, PMMA e-beam resist (Brewer Science PMMA 950K 5% SBC) was spun at 4000 rpm for 40 seconds and baked for 2 minutes at 180^o C. Both samples were loaded into the FEI Novalab system vacuum chamber. Next, e-beam lithography with an electron energy of 30 keV, current of 44 pA, area step size of 4.8 nm and doses between 40 and 270 μAs/cm^2 was applied to write 54 pairs of gold gratings containing 20 grating lines with a period of 610 nm into the resist. The dose variation was intended to fabricate gratings with varying filling factor. The uncoated sample served as the reference sample for alignment of the gratings on the waveguides. This is necessary as the PMMA coated SOI sample could not be visualized without e-beam exposure. The length of the grating lines was set to 40 μ m in order to compensate for any alignment errors and the distance between the first grating and the second grating on each waveguide was set to 0.5 mm. The reason for the rather short distance is to avoid big differences in e-beam writing conditions between each grating in the grating pair.

The relatively thick layer of electron beam resist was needed to obtain good lift-off conditions. When the electron beam enters the resist it spreads out, resulting in an undercut profile when the resist is developed [17]. The sample was developed in an MIBK:IPA (1:3) solution during 30 seconds. Gold adheres badly to silicon. So, 3 nm of Ti was sputtered prior to evaporation of 20 nm of gold. Finally, the gold was lift off in acetone by putting the sample in the acetone at an increased temperature (50 ^{o}C) for about one hour with regular rinsing. A scheme of the process flow is depicted in Fig. 4.20.

The fabrication of gratings was successful only when the exposure dose was high enough, i.e. gratings written with a dose above 160 μAs/cm^2. The grating parameters were measured after fabrication. The period of the gratings is 630 nm, which is 20 nm off target and the filling factor depends on the dose factor. Higher doses result into wider gold grating lines and thus higher filling factor. For the gratings with the smallest grating lines (lowest dose), the width

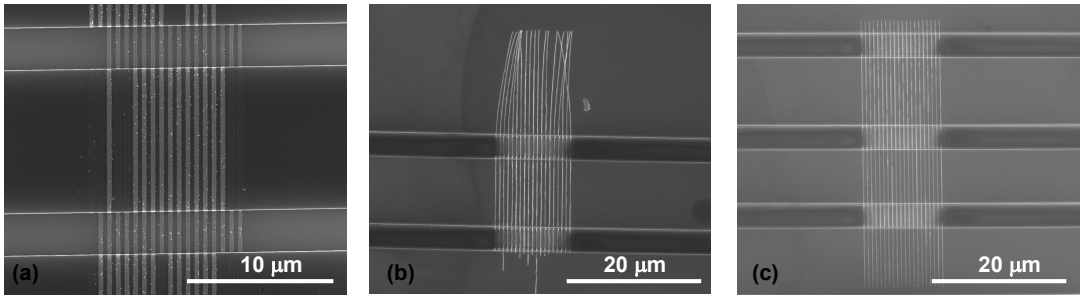

Figure 4.21: Adhesion of gold gratings on SOI waveguides defined by e-beam lithography, (a) without intermediate titanium layer, (b) with intermediate titanium layer but grating lines of width 140 nm, (c) with titanium layer and grating lines of width 180 nm.

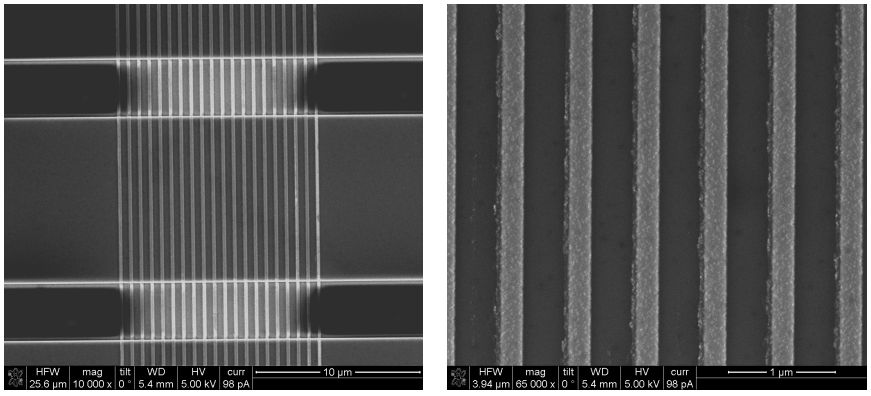

Figure 4.22: Gold grating on SOI waveguide defined by e-beam lithography. Period = 630 nm, filling factor = 30 %, height = 20 nm, 3 nm Ti adhesion layer.

of the individual grating lines was 140 nm or less and adhesion problems occur. This is visible at the termination of the grating lines. We note that without the intermediate titanium layer also wider grating lines would not adhere well to the silicon substrate (see Fig. 4.21). All other gratings were well defined. We assume that the ”rabbit ear”-like structures are rests of PMMA that were not removed during the lift-off process. The grating filling factor varied between 20 % and 33 % which is the parameter space that we targetted.

Unlike the techniques previously described, e-beam lithography allowed us to define gratings directly in contact with the silicon top waveguide layer and with a very low filling factor. The coupling efficiency varied only slightly as a function of filling factor. The measurement and simulation data are plotted in Fig. 4.23. A fiber-to-waveguide coupling efficiency of 30 % was demonstrated in absence of an index matching glue and a coupling efficiency of 34 % was demonstrated in the presence of an index matching glue. A 1dB

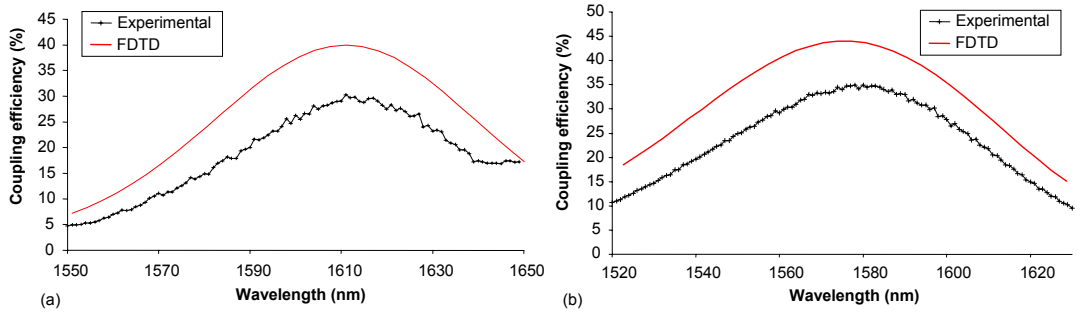

Figure 4.23: Experimentally determined fiber-to-waveguide coupling efficiency of an e-beam fabricated gold grating coupler with parameters: period = 630 nm, filling factor = 30 %, grating height = 20 nm and a 3 nm Ti adhesion on top of an SOI waveguide, (a) in absence of index matching glue and (b) in presence of index matching glue. The buried oxide layer thickness is 2 μm. FDTD simulation results are added for comparison.

bandwidth of 40 nm was measured. The spectral position of the coupling efficiency maximum agrees well with the simulation. As we mentioned before, this maximum is mainly determined by the grating period which turned out to be 630 nm instead of the designed 610 nm. As a result, the maximum is at 1580 nm instead of 1550 nm in the presence of an index matching environment. In terms of efficiency, there is a discrepancy between the simulation and experimental result. There are a number of reasons to explain this. First of all, a titanium adhesion layer was used to promote the adhesion between the gold and the silicon. Titanium is highly absorbing in the telecom spectral region. Although it is a very thin layer of only 3 nm, it causes a 4 % reduction in coupling efficiency. Second, the grating lines are not perfectly perpendicular to the waveguide axis leading to a slight underestimation of the coupling efficiency.

4.5 Conclusion

In this chapter, we introduced a novel type of grating coupler based on a metal grating. Although metals are lossy, we demonstrated that the very strong refractive index contrast between metals and silicon can be exploited for the design of highly efficient grating couplers. A theoretical study of uniform gratings on top of an SOI layer stack taught that the highest coupling efficiencies are obtained for gold and silver grating couplers. A design method for metal grating couplers was proposed and we found that the coupling efficiency is optimal for metal gratings with a low filling factor. A key advantage of metal gratings as compared to dielectric gratings is that only very thin layers suffice

for obtaining optimal coupling efficiencies. This is very interesting from a fabricational point of view. We explored a number of nanopatterning techniques for defining gold grating couplers. The best grating couplers were fabricated using electron beam lithography and demonstrated a coupling efficiency of 34 % and a 1dB bandwidth of 40 nm between SOI waveguides and optical fibers oriented at a 10^o angle with respect to the vertical axis. Good agreement was found between simulation and experimental results.

Bibliography

[1] P.B. Johnson, R.W. Christy "Optical Constants of the Noble Metals" *Phys. Rev. B*, pp. 4370-4379, 1972.

[2] E.D. Palik "Handbook of Optical Constants of Solids" *Academic Press Inc.* ISBN 0-12-544420-6, 1985.

[3] C. Kittel "Introduction to solid state physics" *Wiley*, 7 edition, 1995.

[4] N. W. Ashcroft, N. D. Mermin "Solid state physics" *Holt, Rinehart and Winston*, USA, 1976.

[5] H. Raether "Surface Plasmons on Smooth and Rough Surfaces and on Gratings" *Springer-Verlag*, Berlin, 1988.

[6] J. Homola "Present and Future of Surface Plasmon Resonance Biosensors" *Anal. Bioanan. Chem.* 377, pp. 528-539, 2003.

[7] T. Nikolajsen, K. Lesooon, I. Salakhutdinov, S. Bozhevolyi "Polymer-based surface-plasmon-polariton stripe waveguides at telecommunication wavelengths" *Appl. Phys. Lett.* 82 (5), pp. 668-670, 2003.

[8] J. Dionne "Planar metal plasmon waveguides: frequency-dependent dispersion, propagation, localization, and loss beyond the free electron model" *Phys. Rev. B* 72, 075405, 2005.

[9] E. Kretschmann, H. Raether "Radiative Decay of Non Radiative Surface Plasmons Excited by Light" *Z. Naturforsch.* A, 23, p. 2135, 1968.

[10] J. Roels "Optische excitatie van oppervlakteplasmonen voor sensortoepassingen" *Master Thesis*, Ghent University, 2005.

[11] K.N Victorovich "Interference effects with surface plasmons" *PhD thesis*, Leiden University, 2008.

[12] J. Conway "Efficient coupling to the nanoscale" *PhD thesis*, University of California, 2006.

[13] W. De Cort "Ontwerp en realisatie van een optische schakelaar op basis van oppervlakteplasmonen en vloeibare kristallen" *Master thesis*, Ghent University, 2006.

[14] M. Hochberg, T. Baehr-Jones, C. Walker, A. Scherer "Integrated Plasmon and Dielectric Waveguides" *Opt. Express* 12, pp. 5481-5486 (2002).

[15] P. P. P. Debackere, S. Scheerlinck, P. Bienstman, R. Baets "Surface plasmon interferometer in silicon-on-insulator: novel concept for an integrated biosensor" *Opt. Express* 14 (16), pp. 7063-7072 (2006).

[16] W. Bogaerts "Nanophotonic Waveguides and Photonic Crystals in Silicon-on-Insulator" *PhD thesis*, Ghent University, 2004.

[17] T. Claes "Metalen nanostructuren voor efficiënte en breedbandige koppeling van licht naar geïntegreerde optische circuits" *Master thesis*, Ghent University, 2006.

[18] Z. Zhang, M. Dainese, L. Wosinski, M. Qiu "Resonance-splitting and enhanced notch depth in SOI ring resonators with mutual mode coupling" *Opt. Express*, vol. 16 (7), pp. 4621-4630, 2008

[19] T.G. Brown "Optoelectronic device for coupling between an external optical wave and a local optical wave for optical modulators and detectors" *US Patent* 5.625.729. 1997

[20] B. De Geyter "Light emitting diode integrated on SOI" *Master thesis proposal*, 2008.

[21] D. Taillaert "Grating couplers as interface between optical fibers and nanophotonic waveguides" *PhD thesis*, Ghent University, 2005.

[22] J. Schrauwen, D. Van Thourhout, R. Baets "Focused-ion-beama fabricated vertical fiber couplers on silicon-on-insulator waveguides" *Appl. Phys. Lett.* 89(14), 141102, 2006.

5

Angled facets for vertical coupling

REFRACTION is a well known phenomenon: when looking into a pool, the bottom of the pool always appears closer than it actually is. In this chapter, we use refraction to adjust the coupling direction of grating couplers. This allows for novel coupling approaches between optical fibers and photonic circuits. We propose and demonstrate vertical coupling using angled facet components integrated with grating couplers as well as angled facet components integrated on a fiber facet.

5.1 Introduction

Coupling light into photonic chips with high efficiency is a very important challenge and is being addressed by several research groups. The grating coupler approach seems to gain more and more attention due to the freedom in design parameters and choice of materials. However, grating couplers have one important drawback: the coupling direction and the coupling efficiency cannot be varied independently.

The most striking example of this problem is the attempt to use grating couplers for perfectly vertical coupling between photonic chips and optical fibers. The origin of this challenge is quite fundamental: when the first Bragg diffraction order is used for perfectly vertical coupling, the second Bragg diffraction order causes large reflections. As a result, the directionality is much lower and the coupling efficiency towards the perfectly vertical direction is very inefficient. Moreover, such reflections are unwanted as they lead to cavity formation within the photonic circuit. To avoid those reflections a solution has been proposed consisting of reflectors in the waveguide by etching slits (see section 3.5 and references therein for further details). However, this approach is not completely satisfactory because the second order Bragg reflections are only canceled in a narrow wavelength range. Moreover, the fabrication of these couplers requires two-level processing with very high alignment accuracy (better than 10 nm), which is only possible with very enhanced patterning technology systems such as DUV-steppers.

Another example was highlighted in the previous chapter: for a given buried oxide layer thickness of the photonic circuit layer stack, the maximal coupling efficiency is obtained for just one optimal grating period and consequently, for just one in-plane coupling direction. As a result, for coupling to any other direction than the optimal one, there will be a penalty in terms of coupling efficiency.

In this chapter we present an approach to adjust the coupling direction of grating couplers using angled facets. Doing so, an extra degree of freedom is added so that coupling direction and coupling efficiency can be varied independently.

5.2 Concept

Light coupled out of a grating coupler is redirected by means of an angled facet. The angled facet is implemented in the form of a polymer wedge on top of the grating coupler. The structure is depicted in Fig. 5.1 (a). The polymer wedge contains an angled facet, which introduces an interface between the polymer and the air background. Due to the difference in refractive index, this facet will redirect the light that is coupled out of the grating coupler by re-

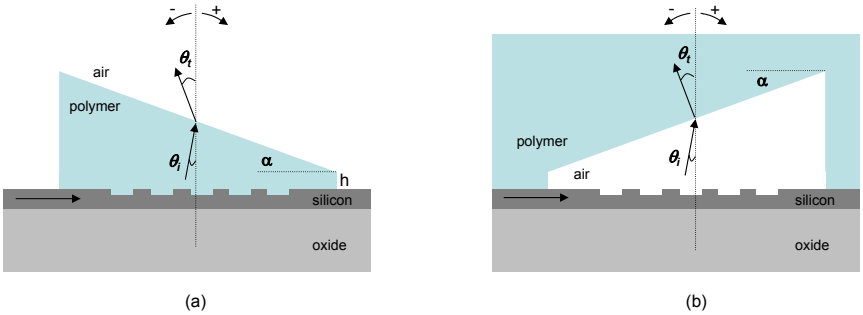

Figure 5.1: Light coupled out of a grating coupler is redirected by means of an angled facet of (a) a polymer wedge or (b) an air wedge on top of the SOI grating coupler.

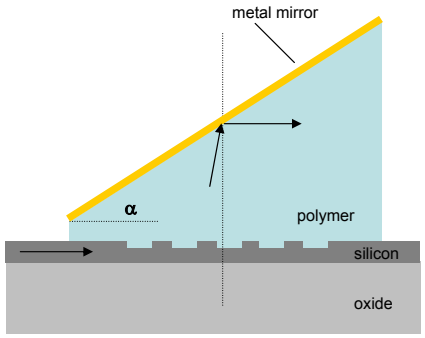

Figure 5.2: Light coupled out of a grating coupler is redirected to the horizontal by means of an angled facet and a mirror.

fraction. By appropriately designing the angle α of the facet, the new coupling direction can be chosen. Fig. 5.1 (b) shows the inverse structure of the polymer wedge based on the same principle.

Redirection of light from grating couplers can be carried out by polymer wedges, but also by more elaborate structures. Fig. 5.2 shows an example of an angled facet combined with a mirror that allows for redirecting the light by reflection into the horizontal direction, for instance for coupling to horizontal fibers. Angled facets in two orthogonal directions in space are also possible and allows for redirection out-of-the plane. In this work, we focus on vertical coupling using polymer and air wedges and the fabrication thereof.

5.3 Design

Conventional one-dimensional as well as two-dimensional SOI grating couplers are designed such that light with a wavelength of 1550 nm is coupled into a direction which is slightly off the vertical axis, typically by about 8^o to 10^o. The design of polymer or air wedges to redirect the light into a different direc-

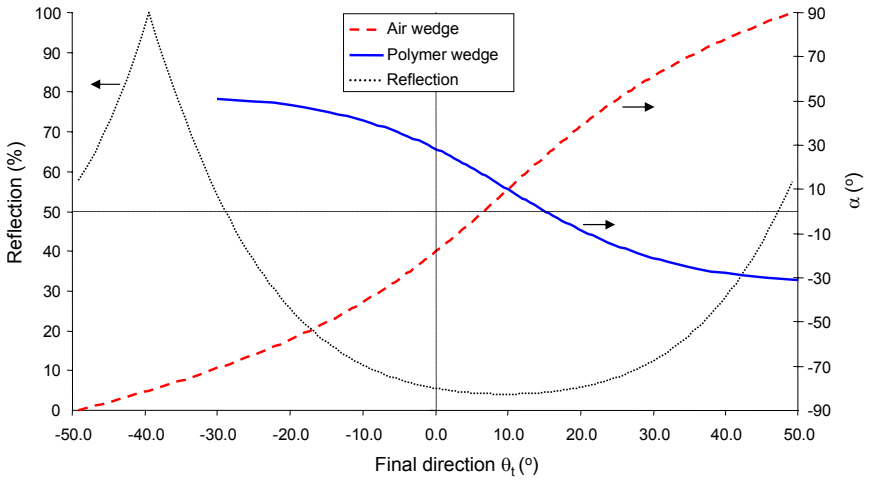

Figure 5.3: Angle of the facet α needed to redirect light from a grating coupler which couples into the 9^o off-vertical direction using a polymer wedge or an air wedge as a function of the final propagation direction θ_t. The reflection at the polymer-air interface is added. The sign of the angle is according to the convention in Fig. 5.1.

tion is based on the laws of refraction (Snell's laws). Fig. 5.3 shows what angle α is needed for the angled facet to couple the light from the grating coupler into any final direction θ_t. Most polymers have a refractive index of about 1.5 at a wavelength of 1550 nm and this value is taken for the calculation. It is assumed that the coupling direction of the grating coupler is $\theta_i = +9^o$. The graph shows that big part of the space is accessible. However, a large fraction suffers from losses due to reflections at the polymer-air interface. The reflection stays under 10 % for an opening angle of about 35^o around the central angle of + 9^o.

Coupling into the vertical direction is obtained either by a polymer wedge with facet angle $\alpha = 25^o$ or by an air wedge with facet angle $\alpha = 18^o$. These values are read from the graph and follow directly from Snell's laws:

$$n_1 \sin(\alpha - \theta_i) = n_2 \sin \alpha \tag{5.1}$$

for a polymer wedge, and

$$n_1 \sin \alpha = n_2 \sin(\alpha + \theta_i) \tag{5.2}$$

for an air wedge, with n_1 and n_2 the refractive indices of polymer and air background respectively. In the next sections, we fabricate and demonstrate both polymer and air wedges.

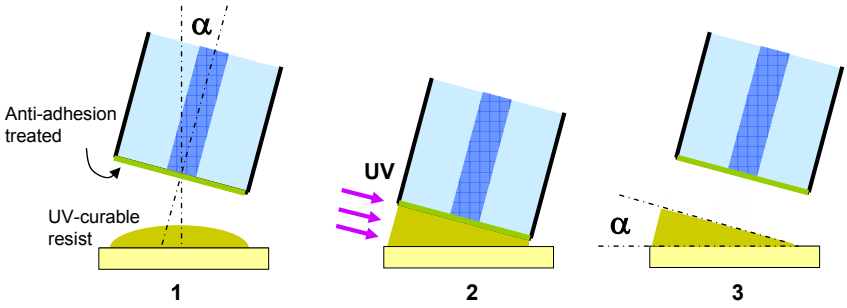

Figure 5.4: Single-step prototype fabrication of angled facets on a substrate using fiber molding. (1) The straight-cleaved fiber is tilted and treated with an anti-adhesion layer, (2) UV-curable resist is squeezed between the fiber facet and the silicon sample, (3) demolding of the fiber.

5.4 Fabrication and measurements

5.4.1 Polymer wedges by fiber molding

Fabrication was explored in two ways. The first technique was proto-type fabrication using fiber molding whereby a fiber is used as the template to create an angled facet. Fiber molding works as depicted in Fig. 5.4. The fiber end is treated with an anti-adhesion layer, then the fiber is introduced into the uncured polymer while it is tilted at the desired angle and after UV-curing and demolding of the fiber, the angled facet remains. In this way, polymer wedges are formed with an area as big as the facet of the fiber, ie. 120 μm diameter. To align the position of the wedge with respect to the grating coupler, we used passive alignment with the aid of the camera image.

We used an SOI chip containing 10 μm broad waveguides etched in the 220 nm top silicon waveguide layer. They contain standard grating couplers with 630 nm period and 70 nm etch depth as well as a mode filter to filter out higher order modes. This sample was mounted on the vacuum chuck prior to polymer wedge fabrication using fiber molding. The performance of the fabricated wedges was evaluated by fiber-to-fiber measurements and the best obtained result is plotted in Fig. 5.5. The losses of the fabricated wedges are as high as 3 dB, which is much higher than expected. We attribute the high loss primiraly to the unaccuracy of the passive alignment procedure for positioning the wedges over the gratings. As a result the distance between the grating couplers and the facets can vary over several tens of micrometers and will not be identical for both gratings. Another cause for the loss is excess polymer present on the sample prior to UV-curing. Due to polymer pieces sticking out of the surface very close to the polymer wedge after UV-curing and given that the wedge area is equal to the fiber facet area, the vertically positioned fibers are hindered during alignment and cannot be brought very

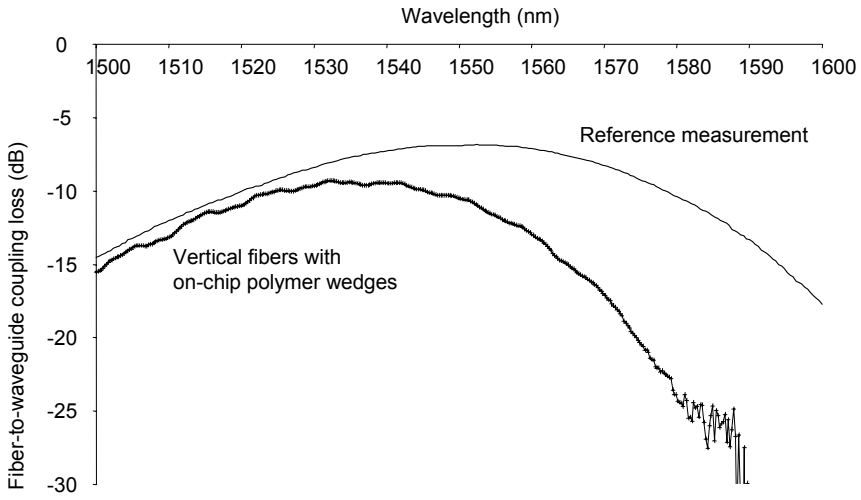

Figure 5.5: Experimentally determined fiber-to-waveguide coupling spectrum extracted from a fiber-to-fiber measurement with two vertically positioned fibers with polymer wedges on the grating couplers fabricated by fiber molding. For comparison, a reference measurement without polymer wedges and a fiber tilt of 10^o is added.

close to the wedge. Although the coupling losses are higher than expected, the measurement results proove that vertical coupling using polymer wedges is possible and more efficient than vertical coupling without polymer wedges.

5.4.2 Polymer wedges by 3D nanoimprint

Much better results were obtained by 3D nanoimprint, whereby a polymer is imprinted and UV-cured using a three-dimensional mold. A 3D mold containing 29^o angled facets was made with focused ion beam milling starting from a mask with alignment markers defined on a glass plate covered by a 150 nm titanium layer. For further details we refer to section 2.3.6.4.

We compared the performance of two different polymers - PAK-01 and SU-8 - molded by a FIB-made 3D mold. The imprint was done with the MA-6 Suss Mask Aligner in vacuum mode. A SEM picture of the final structures is depicted in Fig. 5.6 and the measurement results are depicted in Fig. 5.7 and show that the integration of the polymer wedges for vertical coupling can be done without loss in fiber-to-waveguide coupling efficiency. The coupling efficiency of the SU-8 wedges is systematically a few dB's lower than the PAK wedges. The difference is too big to be attributed to differences in the optical absorption loss between the two polymers. The main cause of the difference can be qualitatively understood from the difference in viscosity between PAK-01 (75 mPa.s) and SU-8 10 (1300 mPa.s). The lower viscosity PAK-01 leaves a much thinner residual layer compared to the high viscosity SU-8. As a result,

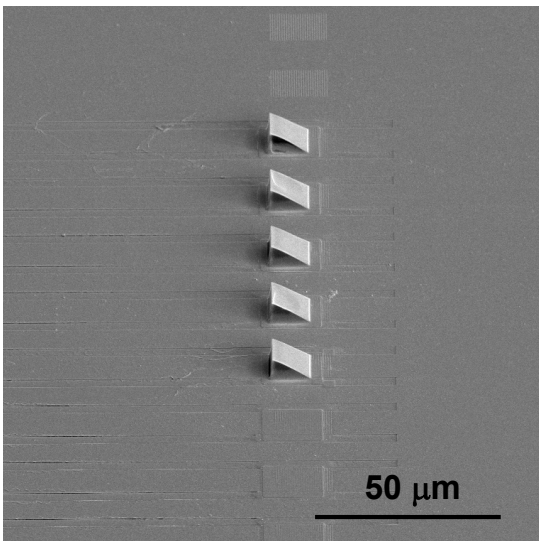

Figure 5.6: Polymer (PAK-01) wedges fabricated by nanoimprint lithography with the MA-6 Mask Aligner on top of broad SOI waveguides and aligned to the grating couplers.

the vertical distance between the grating and the angled facet and - consequently - between the grating and the vertically positioned fiber is lower for the PAK-01 wedges, leading to a higher coupling efficiency. This is in qualitative agreement with the plot in Fig. 5.7. Unlike fiber molding, which is merely suitable for prototyping, this process scheme holds the potential for a wafer-scale process.

5.4.3 Air wedges by molding on fiber facets

In chapter 2, we introduced the molding technique as a very suitable and simple technique to structure fiber facets and its tremendous advantages over conventional direct write techniques. In this section, we apply this technique to make fibers with an angled facet in a single processing step for usage in a vertical fiber-to-waveguide coupling scheme. The simple molding technique works as follows. We used the fabrication set-up depicted in Fig. 2.31. The process is depicted in Fig. 5.9. Starting point is a straight-cleaved single-mode fiber and an anti-adhesion treated silicon sample. The fiber end does not undergo any treatment. The sample is fixed on a vacuum chuck and the fiber is mounted on one of the x,y,z-stages. The fiber holder is set to make an angle of 18^o with respect to the vertical. The fiber end is then immersed for a few seconds in the liquid UV-curable drop of PAK-01 to cover the facet of the fiber. Next, the fiber is brought close to the anti-adhesion treated silicon surface and the resist gets squeezed between the fiber facet and the silicon surface. Once contact is achieved, the resist is cured by UV-light from an EFOS Ultracure 100ss-plus

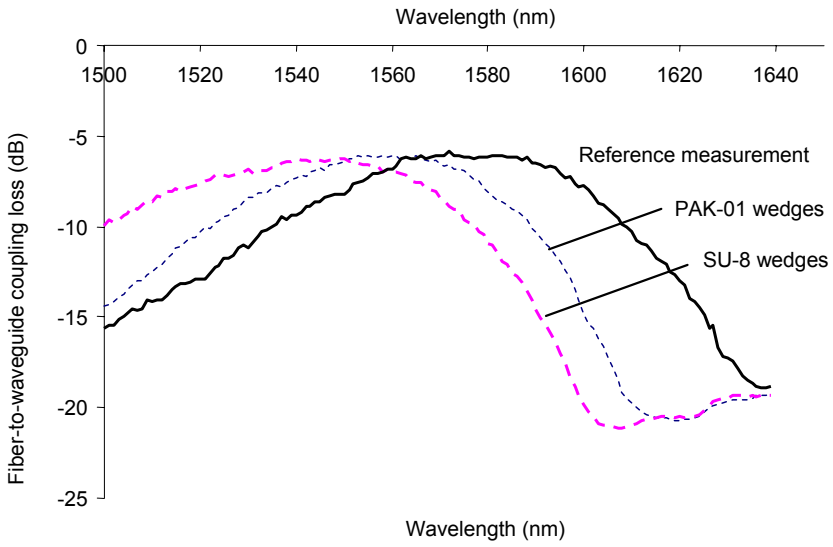

Figure 5.7: Experimentally determined fiber-to-waveguide coupling spectrum extracted from a fiber-to-fiber measurement with two vertically positioned fibers with angled facets on the grating couplers fabricated by 3D nanoimprint using PAK-01 and SU-8. A 10^o to 10^o reference measurement on standard grating couplers is included for comparison.

system for 5 minutes. The fiber is then lifted from the silicon sample to finalize the process. Due to the anti-adhesion treatment of the sample, the fiber is lifted easily and now contains a polymeric facet termination that makes an angle of 18^o with respect to the original fiber facet. Fig. 5.10 depicts a picture of the device taken with scanning electron microscopy.

We used the same sample as in the previous measurements. Two fibers with a facet angle of 18^o with respect to the fiber axis were fabricated and were mounted vertically. A picture is shown in Fig. 5.11 (a). The schematic in Fig. 5.11 (b) shows the light flow from input to output fiber by refraction at the polymer/air interface and diffraction by the grating coupler. Using the camera image of the setup, both fibers were first aligned passively. Then an active alignment of the fiber positions was carried out by optimizing the power output. The SLED with a central wavelength of 1545 nm and a spectrum analyzer were used.

From the measurements, a fiber-to-waveguide coupling efficiency of 32 % and a 1 dB bandwidth of 32 nm were extracted. The spectral dependence is plotted in Fig. 5.12. For comparison, the experiment was repeated with two straight-cleaved fibers. The fiber-to-waveguide coupling efficiency was extracted in the same way and was included in the graph. The coupling efficiency is very low illustrating the necessity of the angled facet when coupling between vertical optical fibers and waveguides containing these grating couplers.

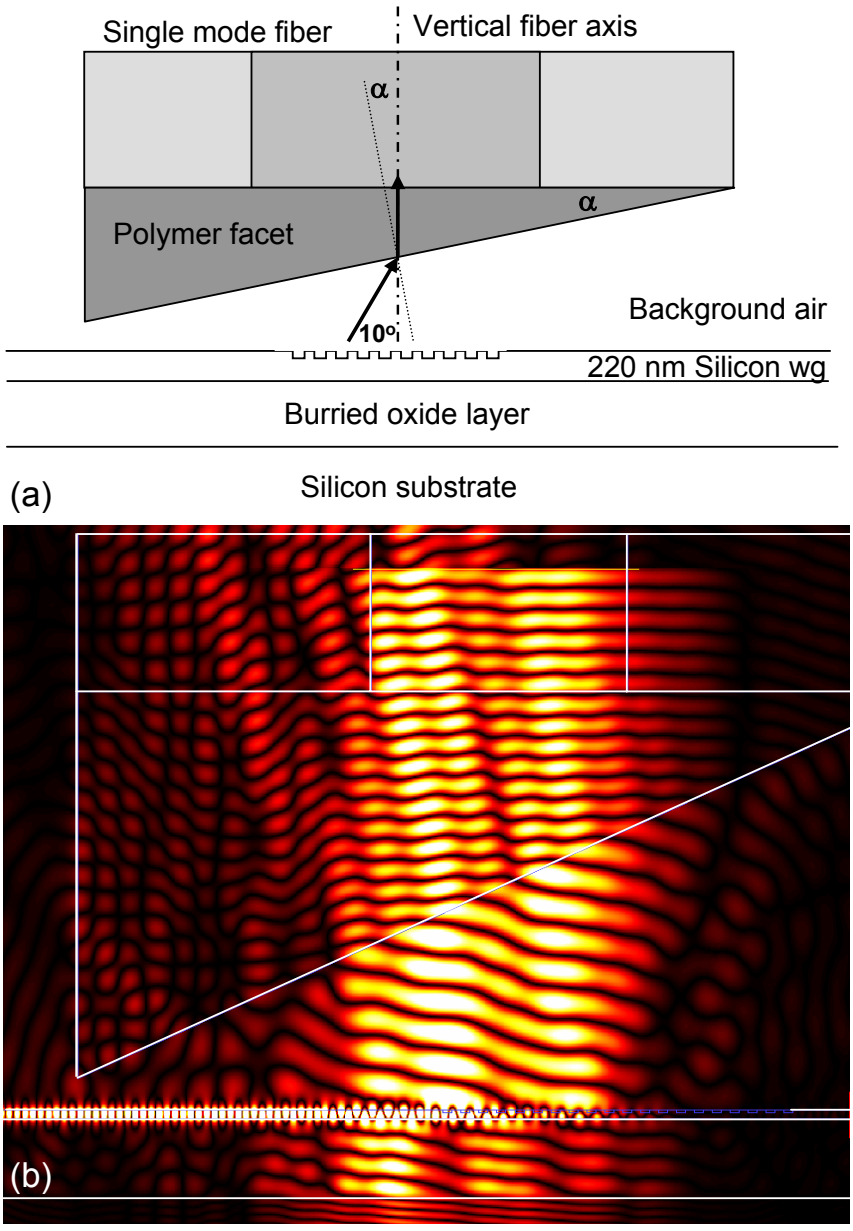

Figure 5.8: (a) Coupling scheme between an SOI waveguide and a perfectly vertical optical fiber using a conventional grating coupler and an adapted single mode fiber with an angled facet. The grating coupler is designed for near-to-vertical diffraction by 10° off the vertical axis to avoid secondary order reflections back into the waveguide. The angled polymer facet causes refraction into the vertically positioned single-mode fiber. (b) The FDTD simulation of the coupling scheme illustrates the refraction of the outcoupled light into the fiber.

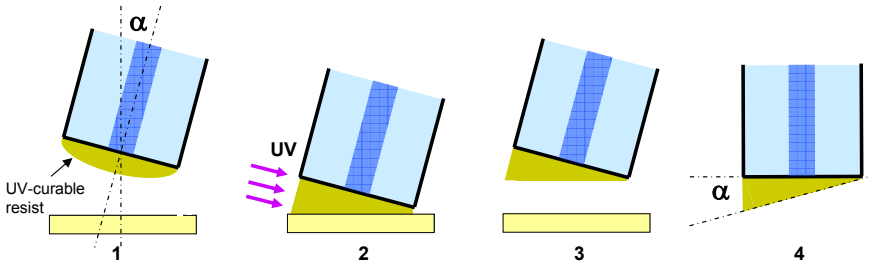

Figure 5.9: Single-step fabrication of an optical fiber with an angled polymer facet. (1) The straight-cleaved fiber is tilted and the silicon sample is treated with an anti-adhesion layer, (2) UV-curable resist is squeezed between the fiber facet and the silicon sample, (3) demolding of the sample. (4) The facet angle equals the initial fiber axis tilt.

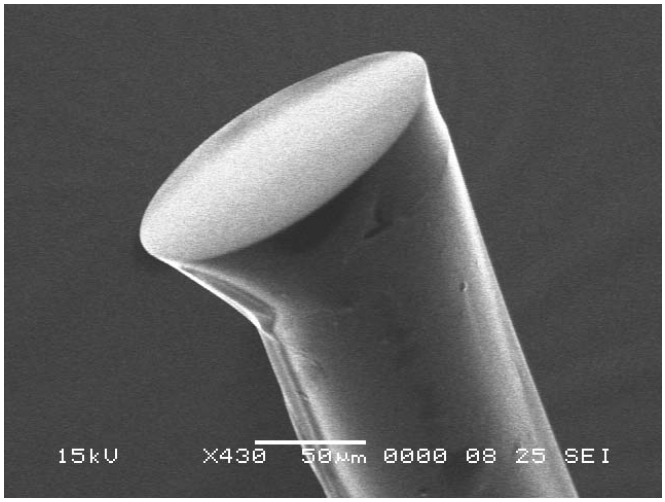

Figure 5.10: SEM picture of the fabricated fiber with a polymeric angled facet fabricated by a molding technique.

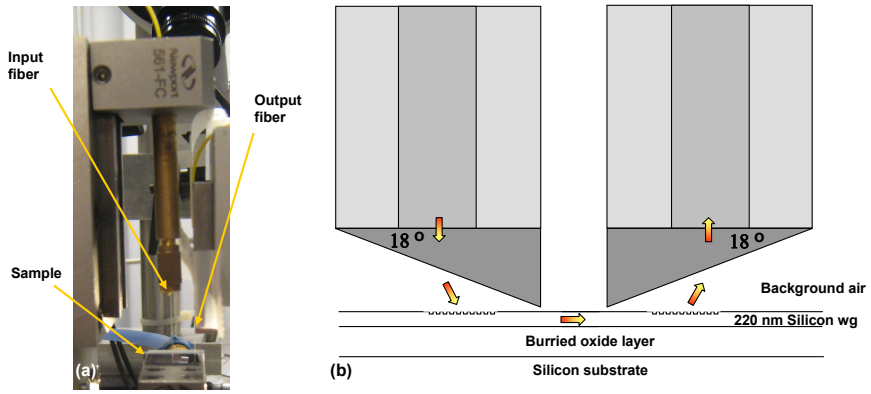

Figure 5.11: (a) Picture of the perfectly vertical mounted fibers in the setup.(b) Schematic of the light flow from input to output fiber.

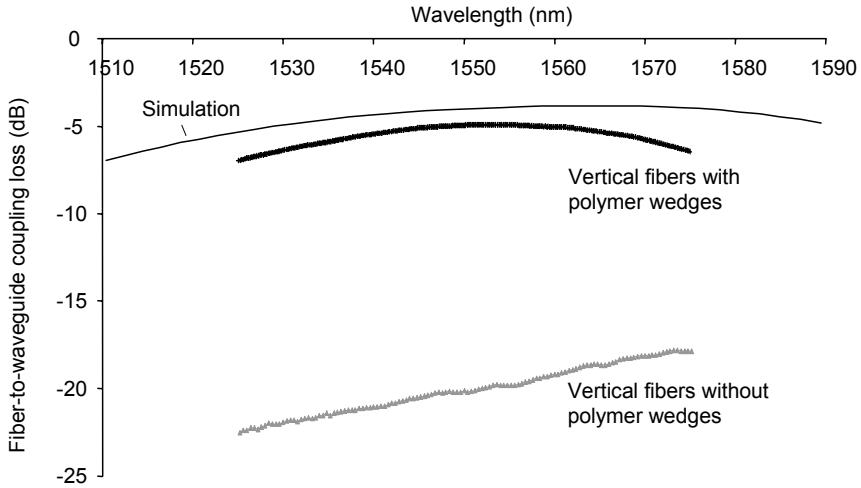

Figure 5.12: Experimentally determined fiber-to-waveguide coupling spectrum extracted from a fiber-to-fiber measurement with two vertically positioned fibers with and without angled facets. The theoretical curve for the angled facet fibers is also plotted.

There is a slight discrepancy between the simulated and measured coupling spectrum: the difference in coupling efficiency is about 1 dB and there is a slight shift in wavelength. This can be explained as follows. First of all, previous work has shown that the measured coupling efficiency of SOI grating couplers is always lower by about 0.7 dB than theoretically expected and that slight wavelength shifts in the order of 10 nm can be attributed to fabrication errors. Furthermore, the distance between the grating and the actual fiber facet is limited in the simulation to 6 μm, whereas it is about 40 μm in the measurement which accounts for an additional loss of 0.4 dB. We conclude that there is good agreement between simulation and experiment for the proposed coupling scheme.

5.5 Applications

Wedges to redirect the light coming from or sent into photonic chips via grating couplers are interesting add-ons in the packaging toolbox of photonic chips. Here we describe a number of possible applications.

Light generation in silicon is a big challenge and a major issue in the development of photonic and optoelectronic components in SOI. So far, the most successful approach to obtain light generation on a silicon chip is by heterogeneous integration of III-V semiconductor materials on the silicon-based platform, either by direct bonding [2] or by polymer (BCB) bonding [3], [4]. An alternative approach is sketched in Fig. 5.13 which was recently proposed by J. Schrauwen et al [5]. The idea is to make use of vertical cavity surface

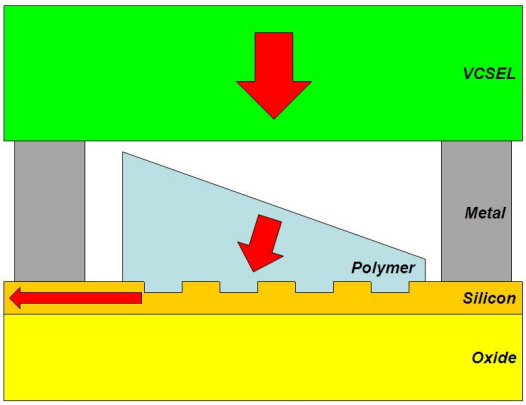

Figure 5.13: Flip-chip bonded VCSEL on top of a grating coupler by use of a polymer refractive wedge. Low reflections are guaranteed by the nearly vertical coupling of the grating coupler. Figure reproduced from [5].

emitting lasers (VCSEL's) and integrate them onto the SOI circuit by flip-chip bonding. Prior to the bonding process, a polymer wedge is defined on top of standard grating couplers to obtain perfectly vertical coupling between the VCSEL and the photonic circuit. Flip-chip bonding uses solder bumps and is a widely used and well-established technique for interconnecting semiconductor devices with electronic chips. Moreover, it can be done with micrometer alignment precision. The same technique can be used for integrating other components such as detectors.

SOI photonic chips are potential candidates for ultra-miniaturized biosensing. Such a biosensor consists of a photonic circuit layer combined with a microfluidic channel layer to flow around the analyte samples to and from the individual nanophotonic sensors. Compact grating couplers allow for simultaneous and remote read-out of thousands of detection sites using free-space coupling to and from the grating couplers. However, the off-vertical coupling direction of current state-of-the art grating couplers is a complication for obtaining compact packaging of these sensor arrays. A possibility is to integrate polymer wedges in the PDMS microfluidic channel layer to serve as an interface between the photonic chip and the external light sources and/or (camera) detector chips. The idea is sketched in Fig. 5.14.

5.6 Conclusion

In this chapter, we described polymer wedges as a novel approach for vertical coupling between optical fibers and photonic chips. We proved that molding is a suitable technique to define these wedges on chips as well as on fiber facets. We demonstrated that the coupling efficiency decreases only slightly because

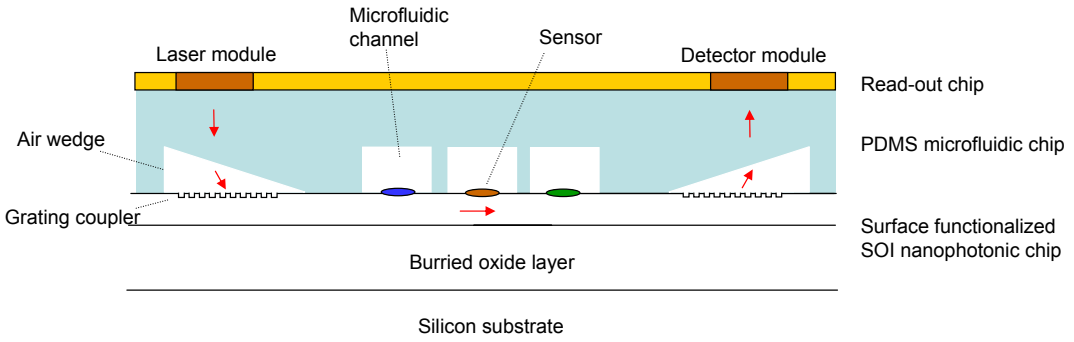

Figure 5.14: Integraded air-polymer wedges into the PDMS microfluidic channel layer as an interface between a nanophotonic sensor chip and a read-out chip.

of the wedge. In the next chapter, we will go a step further and combine the fabrication of angled facets with the fabrication of a metal grating coupler to define a probe for photonic integrated circuits.

Bibliography

[1] G. Roelkens "Heterogeneous III-V/Silicon Photonics: Bonding Technologies and Integrated Devices" *PhD thesis*, Ghent University, 2007.

[2] A.W. Fang, H. Park, O. Cohen, R. Jones, M.J. Paniccia, J.E. Bowers "Electrically pumped hybrid AlGaInAs-silicon evanescent laser" *Opt. Express* 14(20), pp. 9203-9210, 2006.

[3] G. Roelkens, D. Van Thourhout, R. Baets, R. Notzel, M. Smit "Laser emission and photodetection in an InP/InGaAsP layer integrated on and coupled to a Silicon-on-Insulator waveguide circuit" *Opt. Express* 14(18), pp.8154-8159, 2006.

[4] J. Van Campenhout, P. Rojo Romeo, P. Regreny, C. Seassal, D. Van Thourhout, S. Verstuyft, L. Di Cioccio, J. -M. Fedeli, C. Lagahe, R. Baets "Electrically pumped InP-based microdisk lasers integrated with a nanophotonic silicon-on-insulator waveguide circuit" *Opt. Express* 15, pp. 6744-6749, 2007.

[5] J. Schrauwen, S. Scheerlinck, G. Roelkens, D. Van Thourhout, R. Baets "Integrated Photonic Devices Including Refractive Elements and Methods of Coupling Light Between an Integrated Photonic Waveguide and an Optical Element" *US Provisional Patent Application* 61054401, 2008.

[6] H.-P. Loock, S. Brown, J.A. Barnes, N.R. Trefiak, K.L. Laugesen, G. Nemova "Long period grating sensor methods and apparatus" *United States Patent* 7391942, 2008.

6

Metal grating based fiber probe

AN important step towards widescale applications of photonic integrated circuits is the ability to test the operation and performance of circuit parts and components on a wafer-scale. For microelectronic circuits, numerous systems and methods exist for testing. Such systems are based on probes used to apply and read out voltages or currents at specific points in the circuit. But an optical equivalent of such a probe does not yet exist. In this chapter, we introduce such a probe for nanophotonic circuits. We demonstrate its fabrication and usage.

6.1 Introduction

In microelectronics manufacturing, testing of electronic chips at different stages in the fabrication process greatly increases fabrication yield through statistical process control. Testing of electronic circuitry is so successful because it is non-destructive, parametric (it gives quantitative information) and is carried out at a wafer-scale. As an example, the most simple form of circuit testing is carried out with metal tip probes: an input probe is used to apply currents or voltages to a first point in the circuit and an output probe is used to read out the response at a second point. In this way, individual components, groups of components or entire circuits can be tested in a rather straightforward manner, giving not only qualitative but also quantitative information on the performance of the device(s) under test.

For photonic chip manufacturing, testing is equally important. Testing of photonic chips can be done by sending light signals into the chip and check the output signal. Such a testing scheme requires the coupling of light into or out of integrated waveguides, which is not straightforward, especially not for high-index contrast material platforms such as the silicon-on-insulator platform.

The most widely used method for light coupling is butt-coupling whereby light is launched into a waveguide through a cleaved facet. Although inherently simple, this method is only interesting for waveguides that support modes that are comparable in size to the size of the modes supported by the optical fiber. For waveguides with a smaller mode size, butt-coupling remains possible but becomes much less efficient. To cope with efficiency, mode conversion is often used, either within the fiber by using a lensed fiber, either on the waveguide chip by using waveguide tapers, or either by a combination of both. Butt-coupling is not at all interesting for circuit testing. The requirement to dice the chips or wafers to produce optical facets is a big disadvantage. Dicing is time-consuming and difficult for producing high quality facets. Moreover, it is permanent and the effort is useless if after testing it turns out that the photonic circuit is not working. Another disadvantage of butt-coupling is that only the whole circuit between the facets can be tested. Testing of individual components within the circuit is impossible.

Despite its disadvantages, butt-coupling remains widely used for photonic device testing at a die-scale. To date, the best candidate to perform photonic device testing at a wafer-scale is by integrating grating couplers into the circuits. Grating couplers can be defined anywhere in the circuit and play the role of access points where light from a light source such as a tunable laser can be coupled in or out. Vertical (or near-to vertical) input and output fibers are brought in close proximity to the grating couplers for testing. Alternatively, one can work in free space, illuminating the grating couplers from a distance and read out the circuits using the light which is coupled back out via the grat-

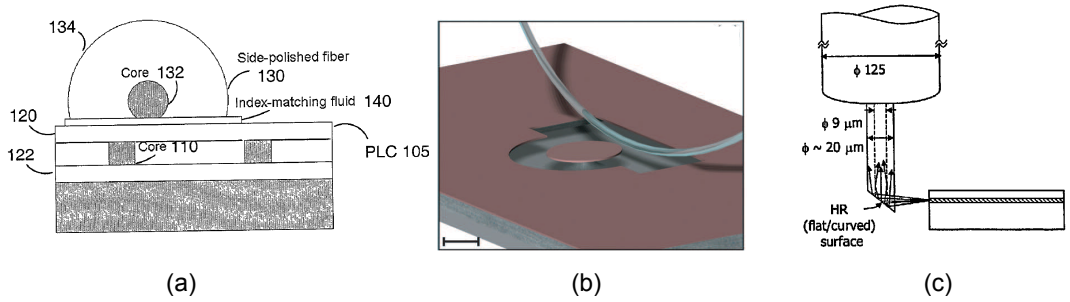

Figure 6.1: Fiber probes proposed in the literature: (a) side-polished fiber probe, (b) fiber taper probe, (c) angled facet fiber probe.

ing couplers using a camera. Both approaches allow to test components and circuits by checking the spectral output.

The main drawback of these approaches are the grating couplers themselves: they need to be integrated in the circuit when the circuit is fabricated. Once they are defined, the access points to couple light in and out are fixed and cannot be changed. As a consequence, only the whole circuit (which may be extremely complex in terms of number and type of components) between the grating couplers can be tested. This makes any testing method based on the integration of grating couplers rather inflexible, though not impossible. For the fabrication of complex devices, a suitable testing method requires a process flow where a number of generic and device-specific components are simultaneously defined close to the final device and directly coupled to grating couplers.

The insight that a viable testing method should be implemented on a wafer-scale rather than on a die-scale has triggered the idea to work with optical probes, i.e. an optical equivalent of the electric metal tip based probes. Fig. 6.1 shows a number of probes based on optical fibers that have been proposed in recent years to assess the problem of wafer-scale testing. However, as we will see in the following section, non of the proposed solutions meets with the requirements for implementing a non-destructive parametric testing method at a wafer scale for high-index contrast material platforms.

In this chapter we introduce a solution that does meet with these requirements. Our probe is an optical element which can be connected to a waveguide at any point in the circuit and with the ability to couple light in or out so that access points can be chosen freely. This enables to establish an optical path between any two (or more) points in a circuit and allows for the testing of the circuit part between those points, ranging from an individual circuit component over a group of components to complete circuits. The probe is especially useful because it is compatible with fiber-optic hardware. A wafer-scale test-

ing method based on such a probe has been described previously (in particular in reference [14]) but it has not yet been demonstrated, not even for low-index contrast waveguide systems.

6.2 Optical fiber probes: literature overview

In the literature, various optical fiber probes have been proposed and demonstrated to assess individual components within a photonic circuit. They are shown in Fig. 6.1: the side-polished fiber probe, the fiber taper probe and the angled/curved facet fiber probe. We describe each of them in the following and discuss their potential for wafer-scale testing of photonic circuits.

The development of fiber probes is strongly related to the development in the past decades of photonic resonators, being fundamental building blocks in photonic circuits and systems. The use of optical fibers to excite and detect high Q whispering gallery modes in near-spherical dielectric microparticles (Q as great as $\approx 10^{10}$ has been demonstrated [1]) - so called microspheres - was first demonstrated in 1995 for 60 μm to 450 μm microparticles. This was done with monomode optical fibers of which the cladding was locally removed by polishing. When such a microsphere is placed in the evanescent field of the propagating mode in the core of the fiber, light can be resonantly coupled between the fiber and the microparticle [2], [3]. The principle of this coupling scheme is based on phase matching between the propagation constant of the whispering gallery mode in the microparticle and the propagation constant of the mode propagating in the fiber.

Figure 6.1 (a) shows a schematic of a side-polished optical fiber probe used for coupling to a waveguide. This coupling scheme is based on phase-matching and was proposed as a method for wafer-scale probing and testing of low index contrast waveguide systems [14]. Despite the high material compatibility with optical fibers and the large dimensions of individual components, there are only few reports on the probing of low index contrast waveguide circuits. In fact, we found only one experimental result of coupling light between a flexible SU-8 on PDMS waveguide, which is attached to a fiber and acts as a multimode probe [12]. A coupling efficiency of only 4 % was reported whereas over 80 % was theoretically predicted. The discrepancy was due to the non-zero gap between the waveguide and the probe over the 2 mm contact path due to roughness.

The search for photonic resonators that combine a high quality factor with a small mode volume has stimulated the research activity on resonant cavities much smaller than microspheres. Optical fibers were seen as a method to study those cavities, but a number of problems had to be overcome. Main problem was the low coupling efficiency between microspheres and eroded fibers ($\approx$ 20 % for very large spheres (radius of $\approx$ 1 mm) and much less for

smaller spheres). Another problem was the lack of mode filtering leading to coupling to higher order modes, both in the fiber as well as in the resonator, which complicates the mode matching.

Fiber tapers offered a solution to overcome these problems. Fiber tapers are adiabatically tapered fibers. They are formed by simultaneously heating and stretching a section of the optical fiber to form a narrow thread joined to the untreated ends of the fiber by a gradual taper transition. The taper waist is several millimeters in length and about a micrometer in diameter (see for example [4] in which a fiber taper with waist diameter of 800 nm is reported). A fiber taper filters all waveguide modes very efficiently except the fundamental mode at both the input and the output. At the waist, the fundamental mode has an evanescent tail extending significantly out into the free space. As a result the propagation constant of the mode will be a function of the waist radius allowing for mode matching to any whispering gallery mode of interest in spheres of a large size range (coupling efficiencies up to 90 % have been demonstrated for microspheres of sizes ranging from 50 μm to 250 μm radius [5]). Because of the micron-scale extent of the taper waist, the probing with a fiber taper also provides the advantage of simple alignment.

With the development of high index contrast micro- and nanophotonic components on a chip defined in semiconductor based material platforms, much smaller cavities with a much larger field confinement were fabricated and studied. Semiconductor cavities are smaller due to the high refractive index contrast provided by such platforms. However, the small mode volumes in high index contrast cavities (such as photonic crystal cavities, microdisk resonators or microring resonators) make coupling with fiber tapers by phase matching even more difficult due to the disparate material indices between the fiber taper core and the semiconductor resulting into highly different propagation constants. Moreover, given that these components have micron to submicron scale dimensions and are integrated on a chip in a circuit or in an alternative assembly, it is imperative that the dimensions of the probe are small enough and only couple to the component of interest.

The original fiber taper design was slightly changed by introducing local dimples in the straight fiber taper so that it is small enough for probing individual high-index contrast resonant cavities on a chip without parasitic coupling to the surrounding substrate (Fig. 6.1 (b)). In particular, coupling to silicon-on-insulator microdisk and microring components has been achieved [7]. However, the coupling efficiency is so low due to the index mismatch that this type of probing can only be used for resonators with a sufficiently high Q-factor.

A solution to compensate for the disparate material indices is exploiting the dispersive properties of photonic crystals. The idea is to use photonic crystal waveguides defined in the semiconductor chip as a connection between the cavity and the fiber taper. A schematic is shown in Fig. 6.2. In other words,

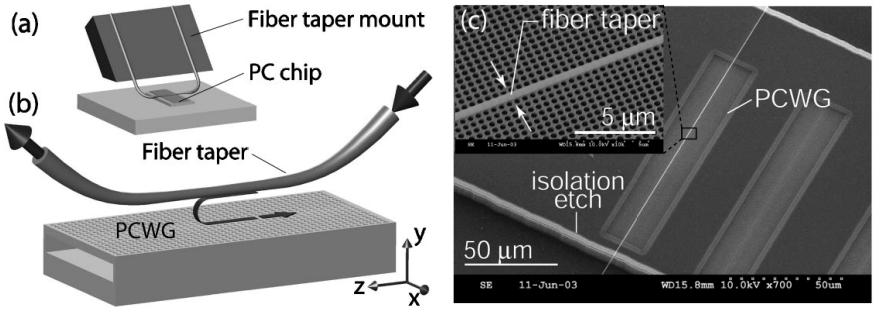

Figure 6.2: (a) Schematic of the taper probe mount and (b) the coupling scheme. (c) SEM-images showing a fabricated photonic crystal waveguide with a fiber taper positioned at its center (reproduced from [10]).

these photonic crystal waveguide structures serve as circuit access points and are in a sense the equivalent of grating couplers for vertical coupling, only now for horizontal fiber taper coupling. Using photonic crystals, the principle of phase matching between a fiber taper mode and a photonic crystal waveguide mode has been demonstrated for silicon-on-insulator [10], chalcogenide glass [8] and InP-based circuits [9]. Coupling efficiencies of higher than 95 % were reported but with a rather limited 3dB coupler bandwidth of 10 nm to 20 nm depending on the fiber taper diameter. Efficiencies are so high because the spatial overlap between the interacting modes can be made large enough over tens of microns so that near-complete power transfer can be achieved. For silicon-on-insulator devices, experiments using a fiber taper with a straight section of ≈ 1 cm have yielded a fiber-to-cavity coupling efficiency of 44 % [11].

Fiber tapers are not a good candidate for wafer-scale circuit testing. For high-index contrast photonic chips, photonic crystal based phase-matching structures are required for coupling, which does not allow for flexible access points. Because of the macroscopic extent of the fiber taper mode, sufficient isolation of the components under test from the other components on the chip is also required. This can be seen on Fig. 6.2 (c) where the photonic crystal waveguide structure is isolated from the rest of the chip by etching. From a practical point of view, the parallel orientation of fiber taper probes with respect to the chip plane is a disadvantage as it makes the coupling very susceptible to any noise sources that produce physical displacements of the fiber probe such as stray air currents, requiring N_2-purged enclosure of the measurement setup [7].

Working with probes in a normal orientation with respect to the circuit plane is a much more practical solution and should allow straightforward implementation of the testing method at a wafer-scale. A vertically oriented fiber probe that allows for high coupling efficiencies was proposed in [13] and sketched in Fig. 6.1 (c). The optical fiber probe contains an angled or curved

facet to turn the light and change the propagation direction incident on the fiber end. The probe is used in combination with deep trenches formed at the edge of the devices under test by etching. Although etching and testing can be done at a wafer-scale, this method is thus destructive and not suitable for non-destructive wafer-scale testing.

A special type of probes are optical fibers tapered down to extremely small tip sizes and placed normal to the circuit plane above the waveguides. Such probes are used for Scanning Near-field Optical Microscopy (SNOM) [15], which can be applied for probing photonic components, mapping of the optical field and study of light propagation of guided modes. However, the coupling efficiency between SNOM fiber tips and waveguides is extremely low. For this reason, SNOM fiber tips can be used for detecting [16] or scattering of light [17] from waveguides, but are not suitable for coupling purposes or wafer-scale testing.

In conclusion, non of the optical fiber probes described in the literature meets with the requirements for implementing a non-destructive parametric testing method at a wafer scale for high-index contrast material platforms.

6.3 Novel concept for wafer-scale circuit testing

We propose a flexible and efficient optical fiber probe used in a normal orientation with respect to the chip plane and with a probing area as small as the fiber core diameter that does not need integrated phase-matching coupling structures or any other integrated structures. Our probe consists of a single-mode fiber with a metal diffraction grating on the core facet which serves as a grating coupler for waveguides in the circuit. In this way broadband light is efficiently delivered to or captured from the waveguides. The main advantage of this probe is that it offers a high degree of flexibility. In particular, these probes do provide a straightforward mechanism to verify whether light can flow between any two points in a circuit while at the same time the spectral properties of the optical path established between those two points can be addressed. As a result, testing a single component or sets of components is possible. A schematic of the concept is depicted in Fig. 6.3 (a). Each probe contains a sub-wavelength period metal diffraction grating and is brought within evanescent field distance to the waveguide (Fig. 6.3 (b)). Light guided in the top waveguide layer will be captured by the fiber as is illustrated by the field plot in Fig. 6.3 (c).

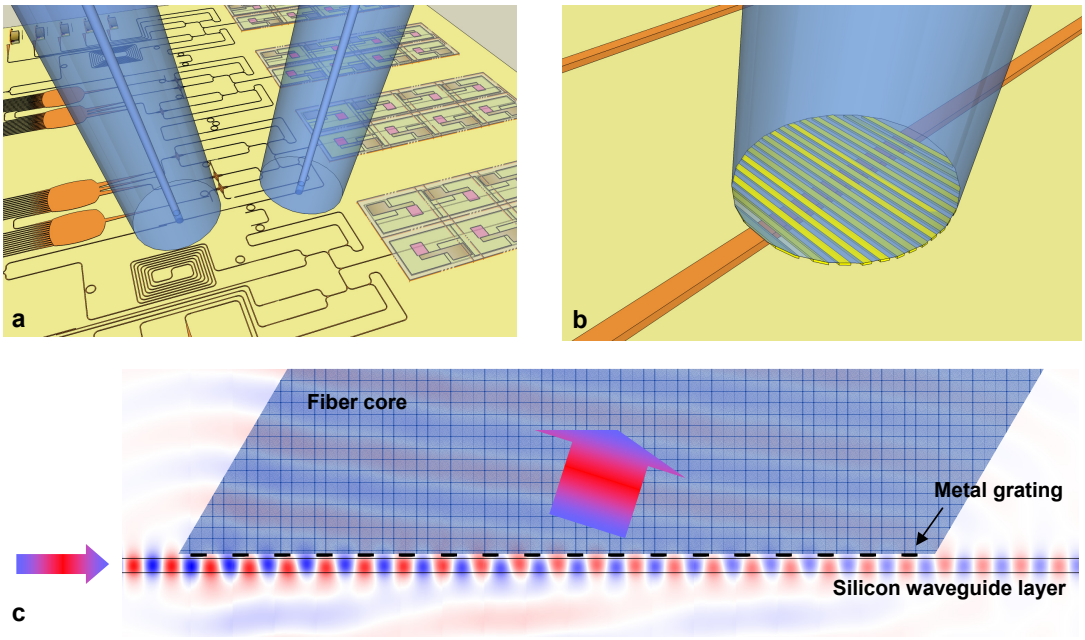

Figure 6.3: (a) Testing an integrated nanophotonic circuit using metal grating fiber probes. The orange arrows represent the flow of light. (b) Light is coupled between the fiber and the waveguide via the metal grating attached to the fiber facet. (c) 2-Dimensional field plot of metal grating induced light coupling between the waveguide and the fiber probe.

6.4 Design

We designed and fabricated a fiber probe for silicon-on-insulator waveguides for TE-polarization. The design of the fiber probe is based on our study of metal grating couplers presented in the previous chapter. We learned that a metal grating on top of an SOI waveguide works as an efficient and broadband grating coupler. From a comparison of the diffraction efficiency of various gratings made of different materials (silicon, silver, gold, aluminum, etc. ...) we learned that - unlike silicon - metals are advantageous because only very thin layers are needed to obtain a high enough directionality and thus high coupling efficiency. Of the different metal grating couplers, silver was shown to be most efficient but less interesting from a fabricational point of view because it is very susceptible to corrosion when exposed to ambient air. For that reason, gold was chosen as the grating material.

Our starting point for the design of a gold grating based fiber probe is the gold grating coupler with a period of 630 nm on top of 10 μm x 220 nm SOI waveguides demonstrating 34 % coupling efficiency and a 1dB bandwidth of 40 nm for a single-mode fiber tilted by 10^o with respect to the vertical. So we fixed the angle between the grating plane and the fiber axis to 80 degrees. We opted for the near-to-vertical configuration to avoid any second order Bragg reflections that might cause cavity formation in the circuit. This design requires the grating to be fabricated on an angle-cleaved fiber.

A crucial aspect of the optical fiber probe is the position of the gold grating with respect to the core. The schematic of Fig. 6.4 shows the problem. Suppose that the gold grating fiber probe consists of a gold grating that covers the whole facet of the angle-cleaved fiber, as depicted in Fig. 6.4 (a). When such a probe is used as an output probe and brought in close proximity to a waveguide, all the light will be coupled out before it reaches the fiber core. As a result, all the light is coupled into the cladding rather than into the core and the coupling efficiency will be zero. On the other hand, if the gold grating fiber probe consists of a compact gold grating that covers only the facet of the core, all the light will be coupled into the core and the coupling efficiency will be maximal.

This was investigated in detail by 2-dimensional FDTD-calculations (Omnisim 4.0, PhotonDesign). For the simulation, the probe grating is assumed in contact with the waveguide. The coupling efficiency at a wavelength of 1540 nm as a function of relative grating position with respect to the fiber core is plotted in Fig. 6.5. It follows that alignment to the fiber core within a tolerancy frame of a few microns is necessary for sufficient coupling, illustrating the importance of alignment for the performance of the fiber probe. It also follows that a grating which is too large compared to the core diameter has limited or no coupling efficiency as light will be coupled out without being captured by the fiber core. Probing with the gold grating fiber probe requires that

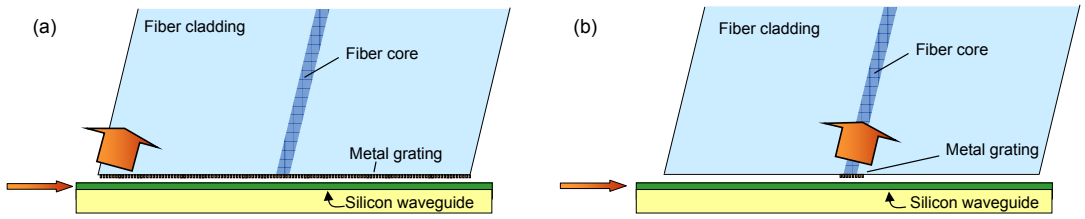

Figure 6.4: (a) The angle-cleaved fiber facet is fully covered with a metal grating. As a result, light is coupled out before it reaches the fiber core. (b) The metal grating is as small as the fiber core facet area and is aligned to it. As a result, light is coupled out into the fiber core.

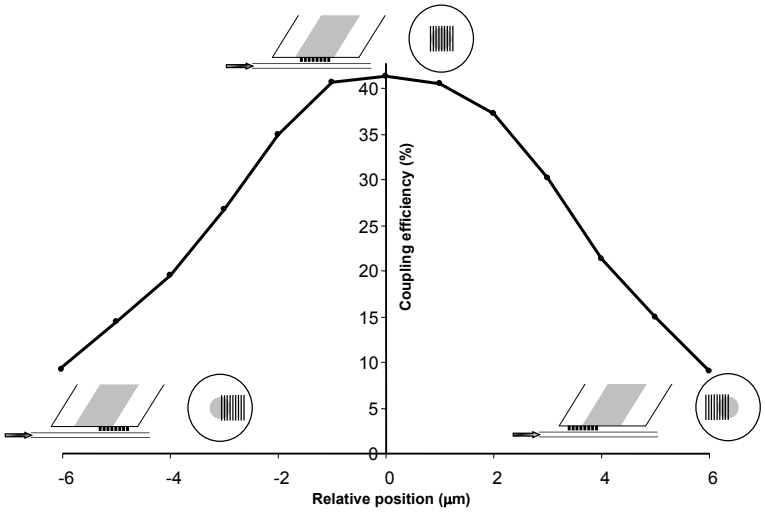

Figure 6.5: Alignment tolerancy analysis by 2-dimensional FDTD-calculations. The coupling efficiency is calculated as a function of relative position of the gold grating with respect to the fiber core. The insets illustrate the relative grating position.

the distance between the top of the waveguide and the gold grating is within the evanescent field decay length of the waveguide mode. FDTD-calculations show a drop in coupling efficiency from 40 % to less than 4 % when the distance to the waveguide exceeds 200 nm.

6.5 Fabrication issues

The proposed optical fiber probe consists of a sub-micron period metal grating on an area as small as the core facet of a single-mode optical fiber and at a predetermined angle with respect to the fiber axis. This seems rather challenging to fabricate, but the techniques developed in chapter 2 allow for a single step fabrication scheme using UV-NITL. We developed two techniques, one based

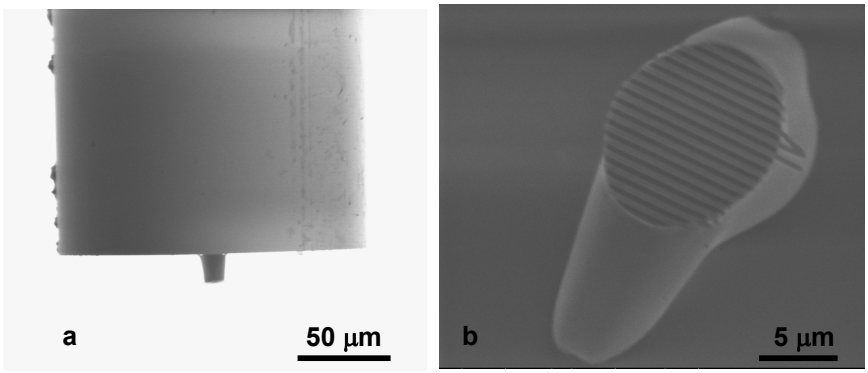

Figure 6.6: A gold grating based fiber probe made by UV-NITL and self-alignment.(a) Side-view. (b) Detail of the gold grating on the facet.

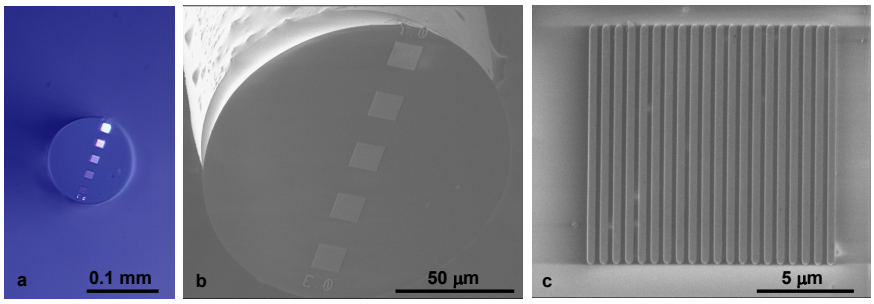

Figure 6.7: A gold grating fiber probe made by UV-NITL and active alignment. (a) Microscope image of a gold grating based fiber probe facet containing 10 x 10 µm gold gratings. (b) Fiber facet with the central grating aligned to the fiber core. (c) Detail of the gold grating.

on self-alignment, the other based on active alignment. Fiber probes made with self-alignment are more critical to damage during handling than fiber probes made with active alignment, which are more robust. The question as to which of both is optimal depends on the available set-up and measurement conditions. In particular, the self-aligned probes require a more mechanically stable set-up and more accurate x,y,z-positioning control than actively aligned probes. Fig. 6.6 shows the result of a self-aligned probe containing a 630 nm period gold grating on the cured polymer cylinder extending from the fiber core with the plane of the grating making an angle of 10^o with respect to the fiber core. Fig. 6.7 shows the result of an actively aligned probe containing a number of 630 nm period gold gratings with varying filling factor, also making an angle of 10^o with respect to the fiber core.

The active alignment procedure is depicted in Fig. 6.8. The technique relies on designing the mold in such a way that it contains a waveguiding layer. The silicon-on-insulator (SOI) material system is very well suited for this purpose with the top silicon layer serving as a lossless waveguide for infrared light.

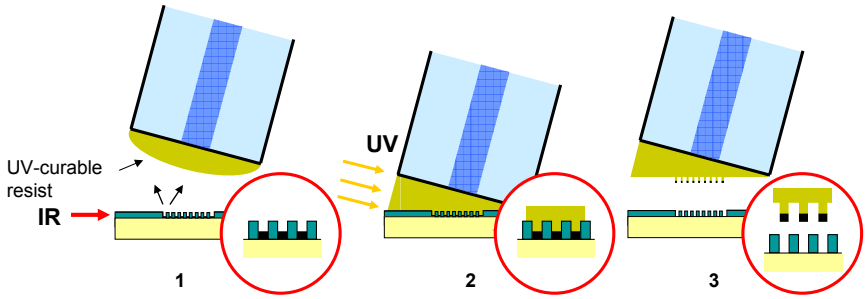

Figure 6.8: UV-NITL using active alignment: (1) power-monitored positioning of the fiber with low-viscous UV-curable resist using infrared light scattered out of the mold waveguide, (2) imprinting and curing by external UV-irradiation, (3) pattern transfer and mold release.

The alignment works as follows. The fiber onto which the gold grating is to be fabricated is connected to a power meter and infrared light is coupled into the silicon waveguide layer of the mold. When the light enters the grating zone it is scattered out of the waveguide. The amount of scattered light captured by the fiber is monitored by the power meter and allows optimization of the fiber's position by in-plane translation.

At this point, we note that the active alignment scheme is based on the scattering of light by pieces of gold at the bottom of trenches in the silicon waveguide layer rather than by pieces of gold on top of the silicon waveguide layer. As a result, the field profile of the light that is coupled out of the waveguide is quite different. This has to be taken into account when using active alignment for probe fabrication. Fig. 6.9 shows the field plots and calculated coupling efficiency with a single-mode fiber tilted at 10 ^{o}. The optimal position of the fiber is at the curve's maximum, which is different in the two cases. For active alignment we use an SOI mold with with gold in the grating trenches. In that case the position of optimal coupling is at about 1 μm from the start of the grating. However, for the gold grating on top of the silicon, it is at 3.8 μm. Thus, for accurate positioning active alignment as described above should be combined with controlled translation. Fig. 6.10 shows the result of active alignment and UV-curing applied through the fiber core for a 10 μm x 10 μm grating. Fig. 6.11 shows the result of active alignment including an additional translation in the direction of the grating by 4 μm and UV-curing. In the first case, only the first few grating lines are transferred: there is a mis-alignment between the core and the grating. However, thanks to the additional translation, the complete grating can be transferred and the alignment is well done.

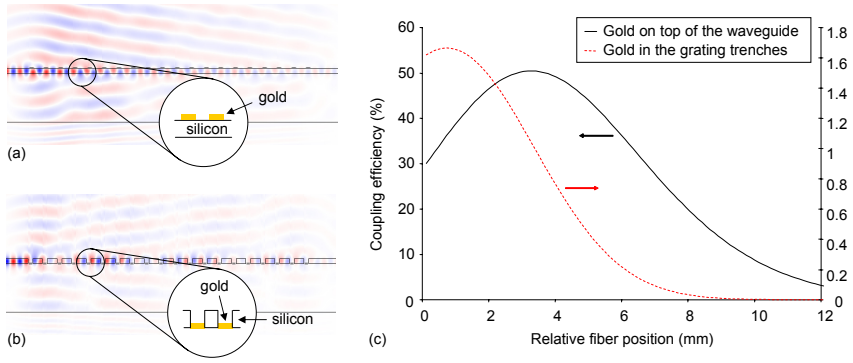

Figure 6.9: Issues with active alignment using a UV-NITL mold. (a) Field plot of waveguide-to-fiber coupling with a gold grating on top of a silicon waveguide. (b) Field plot of waveguide-to-fiber coupling with a gold grating in the trenches of a silicon waveguide. (c) Calculated waveguide-to-fiber coupling efficiency as a function of relative fiber position.

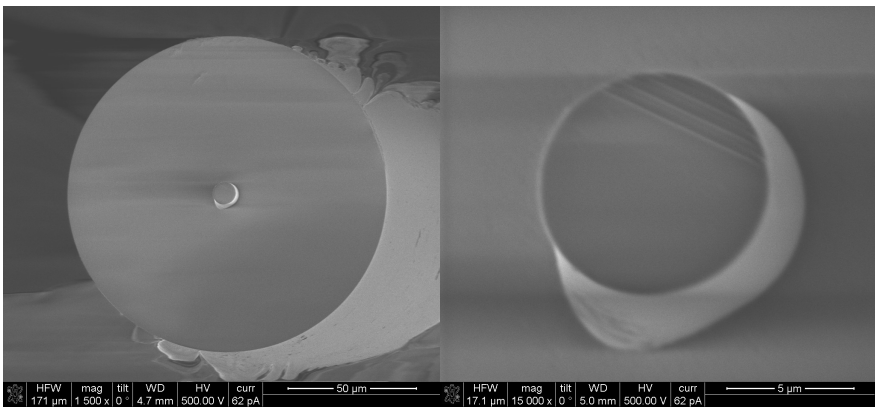

Figure 6.10: UV-NITL of a gold grating on a fiber facet using active alignment. UV-curing is applied through the core of the single-mode fiber when the fiber is at the position of optimal coupling between waveguide and fiber. (a) Fiber facet picture. (b) Detail of the fiber facet: bad alignment between core and grating.

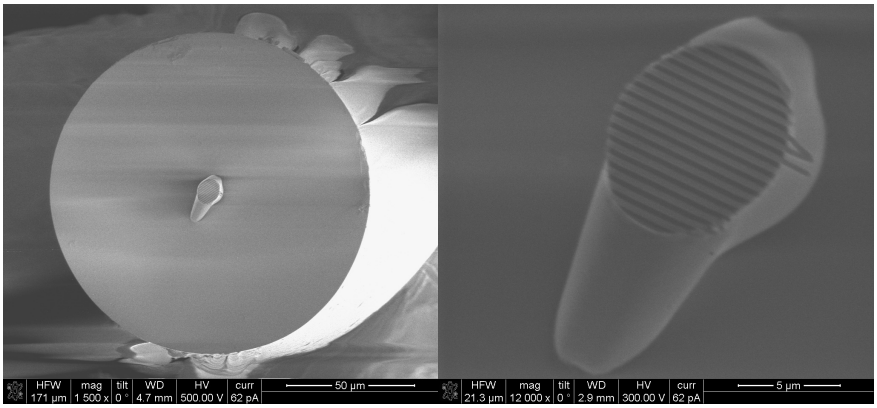

Figure 6.11: UV-NITL of a gold grating on a fiber facet using active alignment followed by an additional translation. UV-curing is applied through the core of the single-mode fiber when the fiber is at the position 4 μm off the optimal coupling between waveguide and fiber. (a) Fiber facet picture. (b) Detail of the fiber facet: good alignment between core and grating.

6.6 Measurement results

6.6.1 Distance dependent coupling

When a fiber probe is brought within evanescent field distance of a waveguide, light will be coupled between the waveguide and the fiber probe. We assessed the distance-dependent coupling and compared with theoretical results from FDTD calculations. For the following experiments probes were fabricated on the measurement setup using active alignment and external UV-curing.

The following experiment was set up. An SOI chip containing waveguides was loaded in the set-up. Each waveguide consisted of a first standard grating coupler, a first taper to taper down from a waveguide width of 12 μm to a waveguide width of 3 μm, a second taper to taper up again and a second standard grating coupler. A first measurement was done with two standard fibers to extract the coupling efficiency of each grating coupler. It was found to be 6 dB at the central wavelength. Next, a probe was fabricated according to the earlier described procedure and mounted in a special fiber mount including a rigid support for the fiber probe end. This probe was brought into contact with the waveguide part of width 3 μm. In this manner, an optical path was established from the source via the fiber to the grating coupler through the SOI waveguide and back via the fiber probe into the spectrum analyzer. Next, the vertical position z of the probe was changed in steps Δz of about 100 nm using a piezo-controlled x,y,z-stage unit. Figure 6.12 (a) shows the raw measurement data for increasing values of the parameter z indicated by the piezo-controller.

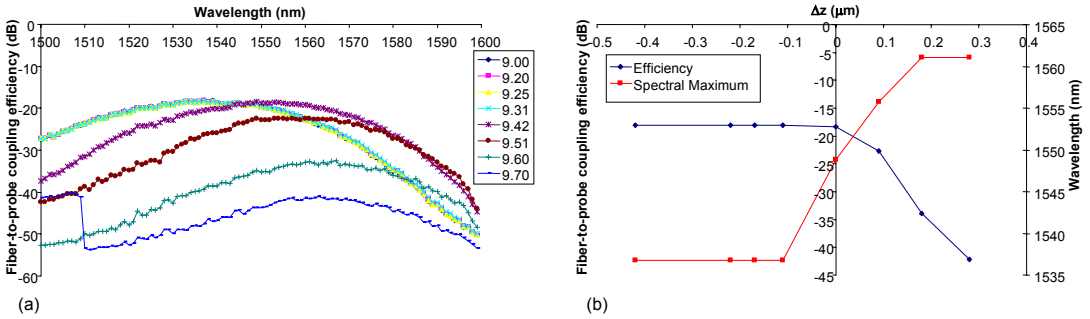

Figure 6.12: (a) Fiber-to-probe coupling efficiency as a function of wavelength for increasing values of z. (b) Fiber-to-probe coupling efficiency and position of the spectrum as a function of Δz.

Figure 6.12 (b) shows the result of the data analysis: the maximal fiber-to-probe coupling efficiency and the position of the spectral maximum are plotted as a function of Δz. Δz is defined as z-zo where z is the value indicated by the piezo-controller and zo is the value indicated by the piezo-controller for which a significant change in coupling efficiency is detected. We interpret the graph in Fig. 6.12 (b) as follows: for Δz between -0.4 and 0.1, the probe is in contact with the waveguide. In this range of Δz, the fiber is slightly under stress. The fiber-to-probe coupling efficiency is at its maximum and does not change until the contact is broken. For higher z-values (Δz between -0.1 and 0.1), the probe loses contact with the waveguide and the distance between the probe's metal grating and the waveguide increases. As a result, the coupling efficiency decreases and the wavelength of the spectral maximum increases. For even higher z-values the coupling efficiency decreases further while the spectral maximum increases until saturation is reached as soon as the distance to the waveguide goes beyond evanescent field distance. These findings are in qualitative agreement with our simulation results.

To assess the quantitative agreement, we repeated the experiment a number of times. The probe-to-waveguide coupling efficiency is now derived by subtracting the grating coupler loss from the fiber-to-probe coupling loss. The results are plotted in Fig. 6.13 (a) and (b), in which the probe-to-waveguide coupling efficiency and the spectral maximum of the efficiency are plotted as a function of Δz. The calculated FDTD result is also plotted for comparison.

It is clear that the relative decrease in efficiency is in good quantitative agreement with theory. The absolute probe-to-waveguide coupling efficiency however is much lower than expected. From earlier work, we expect a discrepancy of 1 to 2 dB between simulation and experiment for a gold grating in contact with a waveguide due to roughness, grating defects, angular misalignment, etc. We attribute the larger discrepancy found here to dust or con-

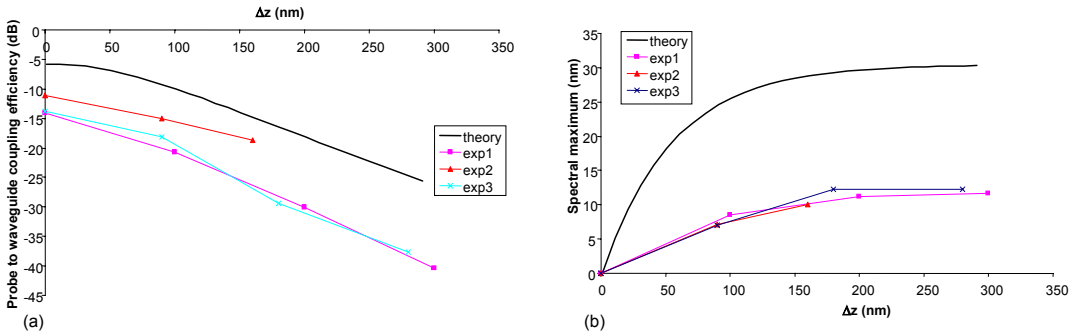

Figure 6.13: Probe-to-waveguide (a) coupling efficiency and (b) spectral maximum as a function of Δz: simulation and experimental results.

taminating defects on the probe's surface. Due to these defects, the minimal distance between the probe's metal grating and the waveguide surface is limited and the optimal coupling efficiency is lower by a few dB. Moreover, these defects hinder proper alignment of the probe's metal grating with respect to the waveguide, which accounts for an additional loss of a few dB. In conclusion, the distance between the waveguide and the metal grating is larger than indicated by Δz and the measured coupling efficiency is thus lower than theoretically expected.

FDTD simulations indicate that the coupling efficiency spectrum shifts the most when the metal grating is closest to the waveguide. The shift gets smaller when the distance between metal grating and waveguide increases. The same conclusions are drawn from our experimental results plotted in Fig. 6.13 (b). However, the experimental data show a much more moderate spectral shift than expected from the simulations. This might indicate that the distance between the metal grating and the waveguide is larger than is indicated by the value of Δz. This is in agreement to our earlier statements explaining the discrepancy between theory and experiment with regard to the coupling efficiency.

6.6.2 Coupling efficiency

Two fiber probes with gold gratings of thickness 20 nm and a grating period of 630 nm were fabricated using active alignment and external UV-curing. The coupling efficiency of these probes was determined as follows. We made use of a 12 mm long waveguide containing standard grating couplers on the 12 μm wide end sections, tapering down to a 220 nm x 3 μm waveguide and with a mode filter in the middle (DUV reticle PICSOI 13, design: DIEHARD1). The alignment procedure is as follows. The input probe was connected to a tunable laser and the output probe was connected to a power monitor. First, the two

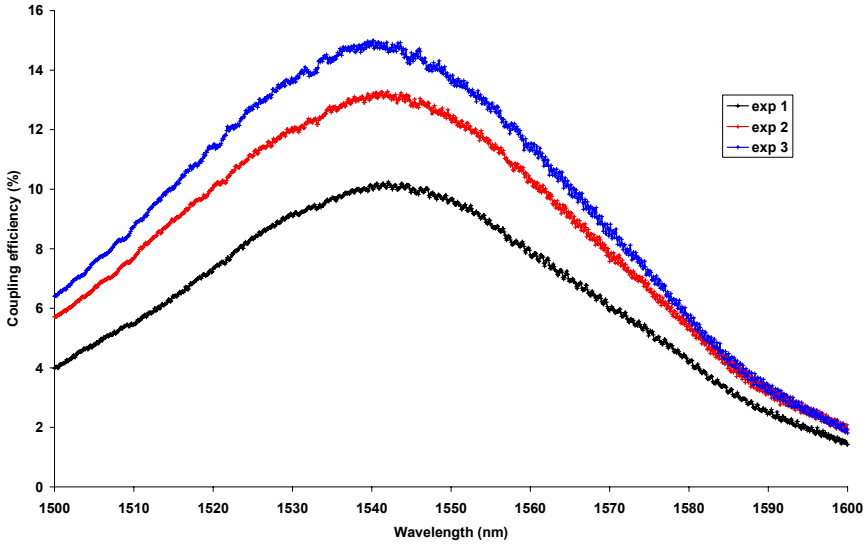

Figure 6.14: Experimentally determined wavelength-dependent coupling efficiency of a gold fiber probe in contact with a 220 nm x 3 μm waveguide after thourough optimization of the position of two probes, measured over time.

probes were aligned over the SOI grating couplers (first passively using camera images, then actively by monitoring the power through the fiber probes and the waveguide) in order to rougly align the probes with respect to the waveguide. The input probe was then moved away from the grating coupler and brought closer to the straight 220 nm x 3 μm SOI waveguide section by decreasing the gap distance between probe and waveguide until a signal was obtained. Then the output probe was moved away from the grating coupler and brought closer to the straight 220 nm x 3 μm SOI waveguide section in the same manner until a signal was obtained. Next, the two probes were carefully moved in the x,y,z-directions in order to optimize the transmission until both probes made contact with the waveguide. The setup was left in this state for a while to allow for mechanical relaxation.

During relaxation, our measurements indicate that the output power increases while the spectral maximum shifts towards shorter wavelengths as depicted in Fig. 6.6.2. This means that the mechanical relaxation is accompanied by a decrease of the gap between the probe facet and the waveguide. The coupling efficiency between waveguide and probe was calculated for the smallest gap obtained. Assuming a losless waveguide and two identical probes, 15 % coupling efficiency was demonstrated at a wavelength of 1545 nm with a 1 dB bandwidth of 38 nm. This is in very good agreement to the coupling efficiency of 16 % expected from 2D simulation result of 42 % multiplied by the 3D correction factor of 0.38 calculated for 3 μm wide waveguides, indicating that the probe facet and the waveguide are indeed in very close proximity.

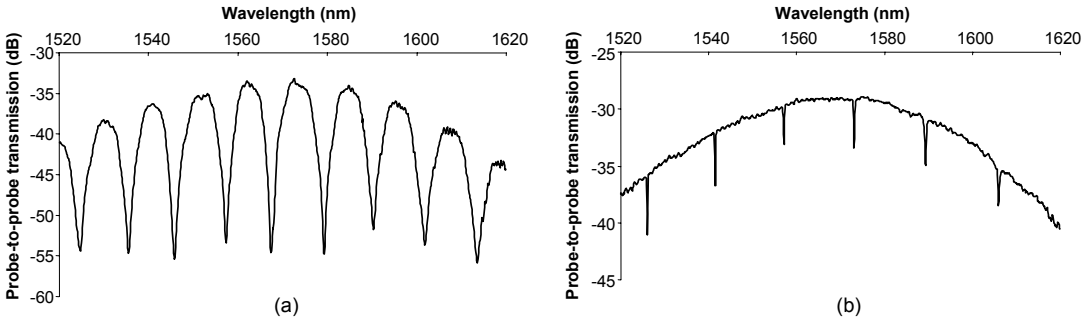

Figure 6.15: Testing of SOI components using two gold grating fiber probes

The procedure outlined above consists of numerous manual alignment steps performed simultaneously for both probes and is rather time-consuming. However, the procedure can in principle be automized. We expect the alignment procedure to be even faster when a self-aligned probe is used as such a probe is less hindered by mechanical obstructions during the alignment. The reason why we worked with actively aligned probes in these and the following experiments is because of their robustness.

6.6.3 Circuit probing

Here, we demonstrate the feasibility of circuit probing for testing individual components, including resonating structures and other structures. Two probes were fabricated using active alignment and external UV-curing. A first probe was used to deliver light to the input port of a Mach-Zehnder interferometer and an SOI microring resonator made of photonic wires with dimensions of 220 nm x 500 nm and a second probe was used to capture light from the output port (DUV reticle PICSOI 8, design: EPIX3). The on-chip footprint of both components is 10 μm x 15 μm and 15 μm x 50 μm respectively. For testing, the probes were used in a contact mode. This means that simple contact was made between the probes and the waveguide without thourough optimization of the position and coupling efficiency. In Fig. 6.15 the measurement data are plotted. The observed spectra indicate that the components are well fabricated and perform as expected. These spectra can be used for further analysis of the performance of integrated components. In this case, for the microring resonator we measured Q-factors of up to 2.6×10^4. The measurements presented here were perforemd on a set-up fixed to a pneumatically stabilized optical table in a standard laboratory environment. The measurements show very little noise when compared to measurements using standard waveguide-to-fiber coupling using grating couplers.

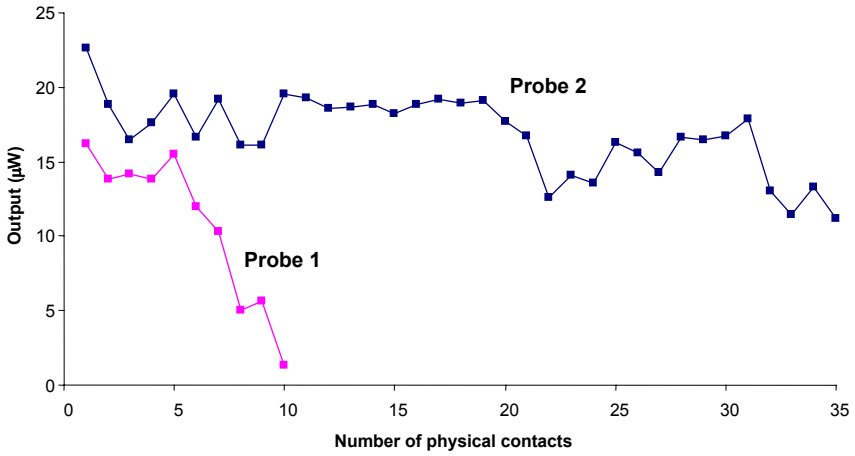

Figure 6.16: Measured output power at a wavelength of 1.55 µm as a function of the number of contacts between probe and waveguide. Probe 1 is made by internal UV-curing. Probe 2 is made by external UV-curing.

6.6.4 Multiple usage

The metal grating based fiber probe can be used in a non-contact as well as in a contact mode. Contact mode provides optimal coupling efficiency, but also damages the probe. When the probe is used in a setup without means to avoid contact, it can still be used, but damage of the facet will occur. There is a big difference in robustness between a probe made by UV-curing through the core consisting of a small fiber core-sized probe end and a probe made by external UV-curing consisting of a large fiber facet-sized probe. This is clear from Fig. 6.16, where the output power is plotted with an input probe of the first type and with an input probe of the second type. For the experiment, the probe was moved up and down and the output power was measured after each contact. It is clear that the first probe degrades rapidly whereas the second probe can be used several times without severe degradation in performance. After the experiment the probes were examined using SEM (see Fig. 6.17 and Fig. 6.18). It follows that the first probe is damaged the most with the original grating structure hardly recognizable. Imprints of the waveguide structures can be discerned. We assume that the infrared light from the light source is heating the polymer such that the probe end is softened leading to imprints during contact. The second probe is more robust and the damage is at the level of the gold material that does not adhere sufficiently well to the polymer in order to withstand the local pressures that arise from the contacting.

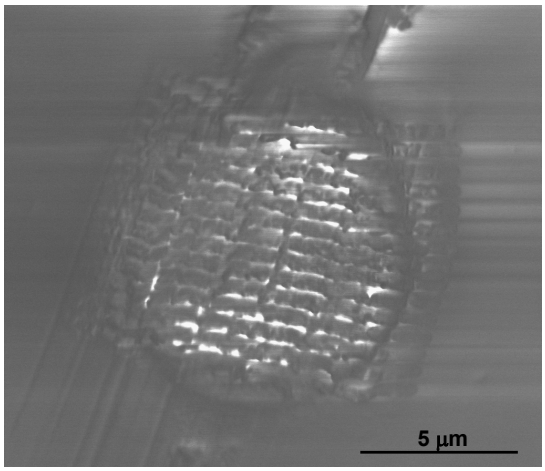

Figure 6.17: SEM-image of probe 1 after usage.

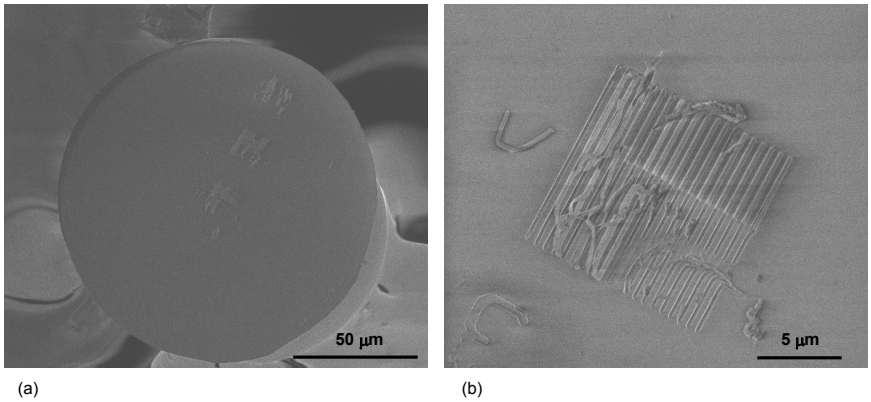

Figure 6.18: (a) SEM-image of probe 2 after usage. (b) Detail of the central grating.

6.7 Conclusion

In conclusion a metal grating fiber probe for probing and testing integrated photonic circuits was proposed. The device consists of a metal diffraction grating at an angled facet aligned to the fiber core. A UV-based nano imprint and transfer process was developed to fabricate gold grating fiber probes in a single step relying on a specially prepared mold. For making the probe an active alignment procedure was proposed as an alternative to self-alignment. Gold grating fiber probes were fabricated and demonstrated 15 % coupling efficiency to SOI waveguides and a 1 dB bandwidth of 38 nm. The demonstrated metal grating fiber probe is a potential candidate for low-cost and wafer-scale testing of highly integrated nanophotonic circuits.

Bibliography

[1] V. B. Braginsky, M.L. Gorodetsky, V.S. Ilchenko "Quality-Factor and Nonlinear Properties of Optical Whispering-Gallery Modes" *Phys. Lett. A* 137 (7-8), pp. 393-397, 1989.

[2] N. Dubreuil, J.C. Knight, D.K. Leventhal, V. Sandoghdar, J. Hare, V. Lefevre "Eroded Monomode Optical-Fiber for Whispering-Gallery Made Excitation in Fused-Silica Microspheres" *Opt. Lett.* 20 (8), pp. 813-815, 1995.

[3] A. Serpenguzel, S. Arnold, G. Griffel "Excitation of resonances of microspheres on an optical-fiber" *Opt. Lett.* 20, pp. 654, 1995.

[4] C. Grillet, C. Monat, C. L. Smith, B. J. Eggleton, D. J. Moss, S. Frdrick, D. Dalacu, P. J. Poole, J. Lapointe, G. Aers, R. L. Williams "Nanowire coupling to photonic crystal nanocavities for single photon sources" *Opt. Express* 15 (3), pp. 1267-1276, 2007.

[5] J.C. Knight, G. Cheung, F. Jacques, T.A. Birks "Phase-matched excitation of whispering-gallery-mode resonances by a fiber taper" *Opt. Lett.* 22 (15), pp. 1129-1131, 1997.

[6] V.S. Ilchenko, X.S. Yao, L. Maleki "Pigtailing the high-Q microsphere cavity: a simple fiber coupler for optical whispering-gallery modes" *Opt. Lett.* 24 (11), pp. 723-725, 1999.

[7] C.P. Michael, M. Borselli, T.J. Johnson, C. Chrystal, O. Painter "An optical fiber-taper probe for wafer-scale microphotonic device characterization" *Opt. Express* 15 (8), pp. 4745-4752, 2007.

[8] C. Grillet, C. Smith, D. Freeman, S. Madden, B. Luther-Davies, E. Magi, D. Moss, B. Eggleton "Efficient coupling to chalcogenide glass photonic crystal waveguides via silica optical fiber nanowires" *Opt. Express* 14 (3), pp. 1070-1078, 2006.

[9] I.-K. Hwang, M.-K. Kim, Y.-H. Lee "All-optical switching in InGaASP-InP photonic crystal resonator coupled with microfiber " *IEEE Phot. Technol. Lett.* 19 (19), pp. 1535 -1537, 2007.

[10] P.E. Barclay, K. Srinivasan, M. Borselli, O. Painter "Probing the dispersive and spatial properties of photonic crystal waveguides via highly efficient coupling from fiber tapers" *Appl. Phys. Lett.* 85 (1), pp. 4-6, 2004.

[11] K. Srinivasan "Semiconductor Optical Microcavities for Chip-Based Cavity QED" *PhD thesis*, Californian Institute of Technology, 2006.

[12] A.J. Zakariya, T. Liu, R.R. Panepucci "Experimental demonstration of a wafer-level flexible probe for optical waveguide testing" *Opt. Express* 15 (24), pp. 16210-16215, 2007.

[13] Y.L. Lam, Y.C. Chan, L.C. Choo, S.L. NG "Wafer Scale L-I-V Probing" *International Patent Publication* PCT WO 03/044504

[14] D.E. Nikonov, M.T. McCormack "Method and apparatus for wafer level testing of integrated optical waveguide circuits" *US Patent Application Publication* US 2003/0123804, 2003.

[15] E. Betzig, J.K. Trautman, T.D Harris, J.S. Weiner, R.L. Kostelak "Breaking the diffraction barrier - optical microscopy on a nanometric scale" *Science* 251 (5000), pp. 1468-1470, 1991.

[16] S. Bourzeix, J. M. Moison, F. Mignard, F. Barthe, A. C. Boccara, C. Licoppe, B. Mersali, M. Allovon, A. Bruno "Near-field optical imaging of light propagation in semiconductor waveguide structures" *Appl. Phys. Lett.* 73, pp. 1035, 1998.

[17] J. T. Robinson, S. F. Preble, M. Lipson "Imaging highly confined modes in sub-micron scale silicon waveguides using Transmission-based Near-field Scanning Optical Microscopy" *Opt. Express* 14, 10588, 2006.

[18] N. Chevalier, Y. Sonnefraud, J. F. Motte, S. Huant, K. Karrai "Aperture-size-controlled optical fiber tips for high-resolution optical microscopy" *Rev. Sci. Instr.* 77, 063704, 2006.

7
Conclusion and perspectives

IN this chapter, we review our work, draw a number of conclusions and give a perspective for future work.

7.1 Conclusions

Photonic integration is a promising route towards the miniaturizating of optical components for sensing and communication applications. High index contrast platforms such as silicon-on-insulator allow for miniaturization of components to the micron-scale and are thus very promising for high-level photonic integration. Silicon is especially interesting because of its compatibility with CMOS electronics and highly mature wafer-scale and thus low-cost fabrication processes. Although standard processes can be used for the fabrication of photonic integrated circuits, novel components and methods are needed for the testing, packaging and assembly of these circuits into final products. In this work, we designed, fabricated and demonstrated novel components that are expected to facilitate testing and packaging of photonic integrated circuits in the future.

We developed a novel type of grating coupler for out-of-plane coupling, based on a metal grating defined on top of the waveguide rather than etched into the waveguide. The influence of the absorption losses in the metal were discussed and it was proven that they do not dominate the diffraction efficiency for a good combination of metal grating parameters, even for metals with a high absorption loss. We designed those parameters for a number of commonly used metals and uniform gratings by simulations based on eigenmode-expansion and finite-difference time domain methods. We calculated their efficiency and found that they are equal to or slightly less than the coupling efficiency of standard SOI grating couplers. We validated our simulation results by fabricating gold grating couplers on top of SOI waveguides for near-to-vertical coupling. We found good agreement between simulation and experimental results. Different approaches to define gold grating couplers were investigated including nanoimprint lithography, e-beam lithography and FIB milling. The best grating couplers were made by e-beam lithography and demonstrated 34 % fiber-to-waveguide coupling efficiency.

We implemented refractive elements on top of grating couplers for redirecting light by refraction. We introduced the concept of polymer wedges and air wedges that contain an angled facet with respect to the circuit plane. These wedges offer are an elegant solution to the problem of perfectly vertical coupling without causing high reflections in the waveguide while keeping broadband operation. We integrated polymer wedges on SOI chips as well as on single-mode optical fiber facets and demonstrated perfectly vertical coupling in both cases. We found that the coupling efficiency penalty is negligeable.

The third component developed in this work is a metal-grating based optical fiber probe. This probe consists of a single-mode optical fiber that contains a tiny gold grating on the facet. When approaching a waveguide with the probe from above, light can be coupled between the fiber and the waveguide by exploiting the diffraction properties of the metal grating. We designed and

fabricated gold grating fiber probes for SOI circuits and demonstrated 15 % coupling efficiency between the probe and a 3 μm wide SOI waveguide, which is in good agreement to simulation results. We proved that the testing of individual components is feasible using two probes and discussed the potential of this probe for wafer-scale testing.

Throughout this work, we made use of various high-resolution patterning techniques including DUV lithography, e-beam lithography and FIB milling. However, for the fabrication of polymer wedges and the structuring of optical fiber facets, none of them were suitable. For this purpose, we developed a number of new techniques based on nanoimprint lithography. We relied on DUV lithography and FIB for the mold fabrication and used conventional alignment and bonding tools for the imprint process. With imprint tools in partnering laboratories, the fabrication of SOI nanophotonic circuits was demonstrated. With in-house developed techniques we demonstrated the fabrication of on-chip sub-micron metal grating patterns, polymer wedges aligned to grating couplers and polymer wedges on fiber facets. Moreover, a technique was developed to prepare hybrid silicon/gold molds for subsequent nanoimprint and transfer of gold gratings on fiber facets and two techniques - self-alignment and active alignment - were developed to align the gold gratings with respect to the fiber core.

7.2 Future work

Throughout this work, we designed and verified the operation of prototype components and proved novel concepts for out-of-plane coupling. However, multiple problems still remain unanswered and various paths could be worth looking at. More specifically, the following selection of problems and issues could be interesting in a possible follow-up of this research work:

For the development of metal grating couplers, we fabricated metal gratings - gold gratings in particular - on top of SOI waveguides in a post-processing scheme by using direct-write techniques on SOI dies. The next step is to use standard DUV-lithography based CMOS processes that allow to define metal grating couplers on a wafer-scale in the CMOS fab. Gold is not a CMOS-compatible metal, so alternatives should be chosen such as aluminum or copper. Lift-off is not a CMOS-compatible process, so etching and/or CMP-processes will be needed. Further work is necessary to develop these processes.

We expect that the integration of active functionality will benefit from the fact that efficient couplers such as aluminum couplers are in fact electrodes and can be used as such. We expect that this insight will lead to novel concepts for photonic and optoelectronic components. Existing approaches for increasing the coupling efficiency of grating couplers such as making use of a varying filling factor over the length of the grating to establish a better over-

lap with the gaussian mode of the optical fiber or making use of bottom and top mirrors can be exploited as extra degrees of freedom in the design of these novel components.

The success of wedge-features in polymer overlayers for packaging depends largely on the scale of fabrication. An approach to bring the fabrication from a chip-scale level to a wafer-scale level would be worth investigating. We mentioned earlier that a possible economically relevant approach is offered by a step-and-repeat imprint process using a small FIB-fabricated mold on the large SOI wafers that come from the CMOS fab.

Polymer wedges on chips are just one example of a non-planar refractive element. More elaborate designs can be lenses, gratings for polarization filtering or for anti-reflection, mirrors, splitters and many more. We expect that all of them can be defined by an appropriate imprint lithography process and by choosing an appropriate polymer material in terms of its optical and mechanical properties.

We solved the problem of high-resolution patterning at an angle with the optical axis of the fiber by developing a nanoimprint-and-transfer technique, whereby a polymer layer connects the grating pattern with the optical fiber. In a broader context, we expect that the principle of transferring a functional material to a fiber facet is of interest to a wide range of applications, especially because it can be performed with multiple fibers simultaneously.

In this context, we think it is worth investigating the potential of nanophotonic components integrated onto fiber facets. Given that fiber facets are in fact big enough to host multiple components, this approach would open up varous new opportunities for packaging, assembly, use for in-vivo applications, etc. A possible approach for integrating photonic integrated circuits on fiber facets is by first fabricating SOI circuits on a wafer and subsequently transfer them onto the fiber using a combination of the UV-nanoimprint-and-transfer process outlined in chapter 2 with underetching of the buried oxide layer of the SOI wafer. A preliminary results is presented in Fig. 7.1. The pictures show a mini-circuit containing a curved grating coupler, a splitter and a ring resonator. The shallowly etched grating coupler is invisible because it is at the opposite side of the silicon membrane. The successful transfer of the silicon to the fiber was proven by EDX (Energy dispersive X-ray spectroscopy) (Fig. 7.1 (c) and (d)).

For testing purposes, we expect that the optical fiber probe as demonstrated in this work provides sufficient coupling efficiency. However, for some applications it may be necessary to improve it. This can be done by working with overlayers and integrate them on the fiber facet. To make this possible, the nanoimprint-and-transfer technique will need to be modified. Another issue is the robustness. We showed that making contact deteriorates the fiber probe. Further development is needed to either avoid contact by working with

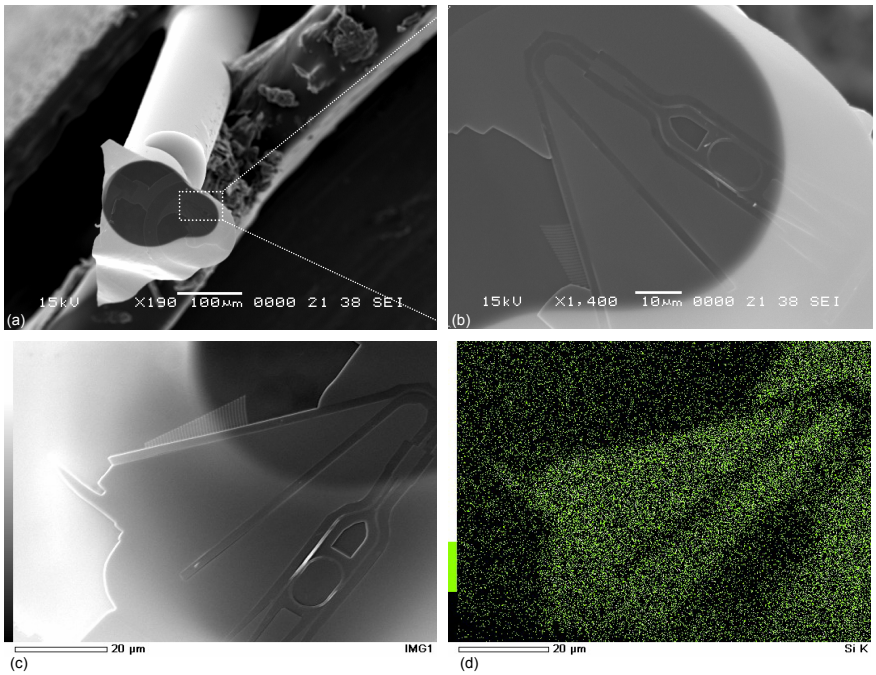

Figure 7.1: (a) SEM picture of a silicon circuit transferred to a fiber facet using UV-NITL, (b) detail of the fiber facet, (c) image and (d) silicon content of the sample.

a more appropriate setup, or encapsulate the probe surface with appropriate layers that act as a protection.

A wafer-scale automated implementation of testing with optical fiber probes needs a mechanism for controlling the distance between the probe facet and the waveguide. Such a mechanism could rely on feedback mechanisms as used in atomic force microscopy or near-field scanning microscopy. However, since testing does not require distances down to a few nanometers but rather a few tens of nanometers, a less demanding feedback approach based on for instance capacitance sensing [1] could also be used.

Wafer-scale testing of individual circuit components is especially interesting when it is combined with a method to fix the component when it does not perform well. For ring resonators, such a method has already been demonstrated using electron beams [2]. The combination of probing and trimming could be an important step in the further development of wafer-scale processes for future photonic integrated circuit fabrication.

Bibliography

[1] L. C. Gunn, R. Malendevich, T.J. Pinguet, M. J. Rattier, M. Sussman, J. Witzens "Wafer-level testing of optical and optoelectronic chips" *US Patent* 7262852 B1, 2007.

[2] J. Schrauwen, D. Van Thourhout, and R. Baets "Trimming of silicon ring resonator by electron beam induced compaction and strain" *Opt. Express* 16 (6), pp. 3738-3743, 2008.